Magneto-transport properties of antiferromagnetic topological insulators MnBi2Te4 and MnBi4Te7

Aoyu Tan

THESIS

submitted to obtain the degree of Doctor of Science of the

UNIVERSITÉ GRENOBLE ALPES

and of the

TECHNISCHE UNIVERSITÄT DRESDEN

Specialty : **Physics**

Arrêté ministériel : le 6 janvier 2005 – 25 mai 2016

Presented by

Aoyu TAN

Thesis directed by **Olivier FRUCHART** and **Bernd BÜCHNER**, co-directed by **Romain GIRAUD**

prepared at the **Laboratory for Spintronics and Devices Technology (SPINTEC)** and **Leibniz Institute for Solid State and Materials Research (IFW)**

as a co-tutelle thesis between the ComUE UGA and the TU Dresden

Magneto-transport Properties of Antiferromagnetic Topological Insulators $MnBi_2Te_4$ and $MnBi_4Te_7$

Thesis defended on **21.09.2021**,
in the presence of the dissertation committee:

Prof. Bernd BÜCHNER, Examiner
Leibniz Institute IFW, Dresden, Germany
Prof. David FERRAND, Chair
Néel Institute, Grenoble, France
Prof. Thorsten HESJEDAL, Reviewer
Department of Physics, Clarendon Laboratory, Oxford, United Kingdom
Prof. Anna ISAEVA, Examiner
Institute of Physics, University of Amsterdam, The Netherlands
Dr. Laura THEVENARD, Examiner
Institut of NanoSciences, Paris, France
Prof. Sergio VALENZUELA, Reviewer
Catalan Institute of Nanoscience and Nanotechnology, Barcelona, Spain
Prof. Matthias VOJTA, Examiner
Institute of Theoretical Physics, Technical University, Dresden, Germany

Abstract

The coupling between topological bands and magnetism gives new routes to investigate novel topological quantum states, such as the quantum anomalous Hall effect (QAHE), axion insulators or magnetic Weyl semimetals, and to control them with magnetic textures. In diluted magnetic topological insulators, such as Cr- or V-doped (Bi, Sb)$_2$Te$_3$ systems, the QAHE is however only observed below 1K. Intrinsic magnetic topological insulators (IMTIs) hold further promises to both higher operating temperatures and the control of additional topological states by changing the magnetic order.

In this work, we investigate the magneto-transport properties of van-der-Waals-layered antiferromagnetic topological insulators from the $[MnBi_2Te_4][Bi_2Te_3]_n$ family, where homogenous 2D ferromagnetic layers with a perpendicular magnetic anisotropy are coupled to each other by exchange interactions, either directly ($n = 0$) or via non-magnetic spacers ($n > 0$). A comparative study of $MnBi_2Te_4$ ($n = 0$) and $MnBi_4Te_7$ ($n = 1$) reveals an evolution from the strong to the weak-coupling regime. Whereas $MnBi_2Te_4$ is an A-type 3D antiferromagnet, with typical spin-flop transitions at intermediate magnetic fields, $MnBi_4Te_7$ behaves as a metamagnet (ensemble of 2D ferromagnets) at low temperature, with ferromagnetic-like properties only driven by the dominant anisotropy and typical spin-flip transitions at low fields. These differences are well captured by a bi-layer Stoner-Wohlfarth model, revealing the importance of the K/J ratio, the relative strength of the magnetic anisotropy K to the interlayer exchange coupling J, in order to describe the different magnetization behaviors. The anisotropy is identified as a key parameter to stabilize the magnetization of intrinsic IMTIs, and the fully-magnetized remanent state of metamagnets below their blocking temperature (T_B ~5K for $MnBi_4Te_7$) suggests a new route to observe the QAHE at higher operating temperatures.

Résumé

Le couplage entre les structures de bandes topologiques et le magnétisme offre de nouvelles voies pour générerde nouveaux états quantiques topologiques, tels que l'effet Hall quantique anormal QAHE, les isolants axioniques ou les semi-métaux de Weyl magnétiques, et pour contrôler les quasi-particules avec la modification des textures magnétiques. Dans les isolants topologiques magnétiques dilués, tels que les systèmes (Bi, Sb)$_2$Te$_3$ dopés au Cr- ou au V, le QAHE n'est cependant observé qu'en dessous de 1K. Au contraire, les isolants topologiques magnétiques intrinsèques (IMTI), aux propriétés magnétiques plus homogènes, offrent de nouvelles perspectives, à la fois pour augmenter les températures de fonctionnement, mais aussi pour ajouter une symétrie spécifique à l'ordre magnétique pouvant ainsi modifier la topologie des structures de bandes, en plus de la brisure de symétrie introduite par le champ d'echange.

Dans ce travail, nous étudions les propriétés de magnéto-transport d'isolants topologiques antiferromagnétiques de la famille [MnBi$_2$Te$_4$][Bi$_2$Te$_3$]$_n$, des empilements à liaisons van der Waals où des couches ferromagnétiques 2D homogènes avec une anisotropie magnétique perpendiculaire sont couplées par un einteraction d'échange antiferromagnétique, soit directement ($n = 0$), soit via des espaceurs non-magnétiques ($n > 0$). Une étude comparative de MnBi$_2$Te$_4$ ($n = 0$) et MnBi$_4$Te$_7$ ($n = 1$) révèle une évolution vers le régime de couplage faible dès qu'un plan Bi2Te3 est ajouté à la structure. Alors que MnBi$_2$Te$_4$ est un antiferromagnétique de type A, avec des transitions de spin-flop typiques, MnBi$_4$Te$_7$ présente un comportement métamagnétique à basse température (ensemble de ferromagnétiques 2D), uniquement induit par l'anisotropie dominante et associé à des transitions de spin-flip à champs faibles, avec des propriétés similaires à celles d'une phase ferromagnétique douce. Ces différences sont bien reproduites par un modèle de Stoner-Wohlfarth à deux couches ferromagnétiques à anisotropie perpendiculaure couplées par un champ d'échange, révélant en particulier l'importance du rapport K/J, soit l'amplitude relative de l'anisotropie magnétique K au couplage d'échange inter-couche J, afin de décrire les différents comportements magnétiques. L'anisotropie est un paramètre essentiel pour stabiliser l'aimantation des isolants topologiques magnétiques, avec la possibilité d'obtenir un état rémanent entièrement aimanté en dessous de leur température de blocage (T_B ∼5K pour MnBi$_4$Te$_7$), suggèrant ainsi une nouvelle voie pour réaliser le QAHE à des températures de fonctionnement plus élevées.

Zusammenfassung

Die Kopplung zwischen topologische Bänder und Magnetismus eröffnet neue Wege, um neuartige topologische Quantenzustände wie den QAHE, Axion-Isolatoren oder magnetische Weyl-Semimetalle zu untersuchen und mit magnetischen Texturen zu kontrollieren. In dotierten magnetischen topologischen Isolatoren, wie Cr- oder V-dotierten (Bi, Sb)$_2$Te$_3$-Systemen, wird der QAHE jedoch nur unterhalb von 1K beobachtet. Intrinsische magnetische topologische Isolatoren (IMTIs) versprechen darüber hinaus sowohl höhere Betriebstemperaturen als auch die Kontrolle zusätzlicher topologischer Zustände durch Änderung der magnetischen Ordnung.

In dieser Arbeit untersuchen wir die Magnetotransporteigenschaften von vdW-geschichteten antiferromagnetischen topologischen Isolatoren aus der [MnBi$_2$Te$_4$][Bi$_2$Te$_3$]$_n$-Familie, bei denen homogene 2D-ferromagnetische Schichten mit einer senkrechten magnetischen Anisotropie durch Austauschwechselwirkungen gekoppelt sind, entweder direkt ($n = 0$) oder über nicht-magnetische Spacer ($n > 0$). Eine vergleichende Untersuchung von MnBi$_2$Te$_4$ ($n = 0$) und MnBi$_4$Te$_7$ ($n = 1$) zeigt einen Übergang in den Bereich der schwachen Kopplung. Während MnBi$_2$Te$_4$ ein Antiferromagnet vom A-Typ ist, mit typischen Spin-Flop-Übergängen bei mittleren Magnetfeldern, verhält sich MnBi$_4$Te$_7$ bei niedriger Temperatur wie ein Metamagnet (Ensemble von 2D-Ferromagneten), mit ferromagnetähnlichen Eigenschaften, hervorgerufen nur durch die dominante Anisotropie, und typischen Spin-Flip-Übergängen bei niedrigen Feldern. Diese Unterschiede werden durch ein modifiziertes Stoner-Wohlfarth-Modell gut erfasst, wobei die Bedeutung des K/J-Verhältnisses, der relativen Stärke der magnetischen Anisotropie K zur Zwischenschicht-Austauschkopplung J, zur Beschreibung des unterschiedlichen Magnetisierungsverhaltens deutlich wird. Die Anisotropie wird als Schlüsselparameter zur Stabilisierung der Magnetisierung von intrinsischen IMTIs identifiziert, und der vollständig magnetisierte Restzustand von Metamagneten unterhalb ihrer Blockierungstemperatur (T_B ∼5K für MnBi$_4$Te$_7$) legt einen neuen Weg zur Beobachtung des QAHE bei höheren Betriebstemperaturen nahe.

Extended abstract

Three-dimensional topological insulators (3DTIs) are non-trivial insulators with band inversions and stable degeneracies at certain high-symmetry points in momentum space. The materials have drawn much attention not only due to the Dirac nature of topological surface states, but also due to their specific helical spin texture. The spin-momentum locking gives unique properties to these quasi-particles, different from those in graphene, which may be beneficial for 2D spintronic applications. Coupling topological surface states with magnetism can induce a non-trivial gap at the Dirac point, which allows for further novel physics such as the quantum anomalous Hall (QAHE) effect, where 1D edge-state dissipationless charge transport can be achieved without applying any external magnetic field (contrary to the quantum Hall effect, quantum Hall effect (QHE)). The conductive channels in the QAHE regime, as they are fully spin polarized, can serve as pure spin sources and spin filters, and most importantly as ballistic conductors for information transfer. Furthermore, these topological channels can also generate other exotic states, such as Majorana states in an anomalous Hall insulator/superconductor heterostructure[1] or in the quantum wire geometry[2], which may be further applied to quantum computation.

The search for experimental methods to efficiently couple the surface states in a 3D topological insulator with magnetism has been a long run. The task was veiled at the beginning since doping topological insulators with magnetic elements can also increase the bulk carrier density, making the novel topological properties of gapped surface states difficult to evidence. It was found out in 2010 that Cr- or V- doped (Bi, Sb)$_2$(Se, Te)$_3$ systems can benefit from the large Van Vleck susceptibility and therefore can have long-range magnetic order without much bulk conductivity introduced[3]. The QAHE was later realized in these systems[4, 5]. However, the observation was only possible at very low temperature ($\sim$0.1K), which made this physics difficult to investigate. Other proposals based on Mn-doped Bi$_2$(Se, Te)$_3$[6] or on proximity effects in topological insulator/ferromagnet insulator heterostructures[7] failed to become alternative routes.

A new type of magnetic topological insulators was proposed by R. S. K. Mong et al. in 2010[8], when considering antiferromagnetic order. The material has layer-dependent magnetic properties, depending on magnetic surface terminations. The nearest neighboring layers are antiferromagnetically coupled and the next neighbors are ferromagnetically coupled. This layer-wise property can be relatively handy to achieve in van der Waals materials. When the magnetism couples with the topological surface states, depending on the parity of the layers, different topological states can exist: the quantum anomalous Hall state exists in the odd-numbered layers, and the axion insulator state exists in the even-numbered layers. This extended the studies of magnetic topological insulators from ferromagnetic materials to antiferromagnetic materials.

The members of the [MnBi$_2$Te$_4$][Bi$_2$Te$_3$]$_n$ (MBT) family including MnBi$_2$Te$_4$ and MnBi$_4$Te$_7$ were identified as antiferromagnetic topological insulators[9, 10]. These are van der Waals materials with the layers stacking in the A-B-C manner. Each MnBi$_2$Te$_4$ layer (one septuple layer) consists of seven atoms with covalent bonds. The layer-dependent magnetic properties mentioned above are expected in such systems[11]. The bulk MnBi$_2$Te$_4$ is therefore an antiferromagnet. By inserting non-magnetic spacers Bi$_2$Te$_3$ layers between the septuple layers, other derivatives in the [MnBi$_2$Te$_4$][Bi$_2$Te$_3$]$_n$ family can be obtained, such as MnBi$_4$Te$_7$, MnBi$_6$Te$_{10}$ and others. Ab initio calculations predicted the gapped surface states of these materials[9, 10]. As the magnetic

properties in these materials are not introduced by extrinsic doping, and since the materials ideally grown homogenous have a larger magnetization compared to diluted magnetic topological insulators, a relatively large band gap can exist in these materials. Together with their relatively high Néel temperatures, this paves the road to achieve the QAHE at higher temperatures. Experimentally, these materials can be obtained by bulk-crystal growth methods of eutectic compounds formed from the melt of MnTe and Bi_2Te_3 mixtures[12]. Thin films can be grown with the molecular beam epitaxy (MBE) method[13]. The angle resolved photoemission spectroscopy (ARPES) measurements on the crystals confirmed the opening of non-trivial band gaps on the surface states. The superconducting quantum interference device (SQUID) measurements also showed the antiferromagnetic properties of the samples[9].

Due to the different spacing between the magnetic layers in the two materials $MnBi_2Te_4$ and $MnBi_4Te_7$ (13.6Åand 23.8Årespectively[14]), the interlayer exchange coupling can be varied. However, the actual mechanism that drives the different magnetic properties among different members of $[MnBi_2Te_4][Bi_2Te_3]_n$ was not well understood. Spin-flop transitions at relatively large field were observed for $MnBi_2Te_4$[9]. Similar spin-flop transitions were also observed for $MnBi_4Te_7$ near the Néel temperature, but at lower temperature, ferromagnetic behaviors were reported[10]. The objective of this work is to investigate the magnetic properties of $MnBi_2Te_4$ and $MnBi_4Te_7$ by means of transport measurements. In fact, the perpendicular magnetic anisotropy can make these antiferromagnets different from each other. In this work, a general discussion about the relative role of the uniaxial magnetic anisotropy and the interlayer exchange coupling in co-linear A-type antiferromagnets is carried out.

For the sample preparation, bulk crystals grown by Anna Isaeva's group at the TU Dresden. were mechanically exfoliated and transferred to SiO_2/Si++ substrates. Nanostructures with thicknesses between 20nm to 100nm were obtained. Electron beam lithography was used to obtain ohmic contacts, and then to design the Hall geometry of the samples. Magnetotransport measurements were carried out in a temperature range of 0.1∼300K, using 2D/3D vector magnetic fields (2/2/6T and 1/12T setups).

The temperature dependence of the longitudinal resistivity of both $MnBi_2Te_4$ and $MnBi_4Te_7$ shows a metallic behavior. This is typical for materials with some structural disorder, similar to the case of non-magnetic 3D topological insulators[15], but here possibly due to the intermixing of Bi and Mn, in addition to anions disorder. Resistivity peaks have been observed at Néel temperatures, where large spin fluctuations exist. The Néel temperature is 23K for $MnBi_2Te_4$ and 12K for $MnBi_4Te_7$. Comparing the Néel temperature to the Curie-Weiss temperature of both materials gives us a clue about the relative strength of their interlayer exchange coupling. According to the molecular field theory, the relative strength of the interlayer exchange coupling is related to the ratio between the Curie-Weiss temperature and the Néel temperature. A simple calculation suggests a much weaker interlayer exchange coupling in $MnBi_4Te_7$, which is consistent with the large spacing between the magnetic layers[16].

When sweeping the field along the easy axis, magnetic transitions can be identified with distinct changes in both the longitudinal resistivity and the transverse resistivity. Generally speaking, $MnBi_2Te_4$ has a rather large spin-flop transition field (∼3.2T at 2K) compared to $MnBi_4Te_7$ (∼0.1T at 10K). The spin-flop transition field can be roughly estimated with the anisotropy and exchange coupling strength $B_{\mathrm{sf}} \sim \sqrt{JK}$. Assuming the anisotropy is similar in both materials, one can see that the exchange coupling will be much weaker in $MnBi_4Te_7$. In addition, the difference between the saturation field and the spin-flop transition in $MnBi_2Te_4$ is large (B_{sat} ∼6.9T at 2K), whereas the two transitions are nearly at the same field for $MnBi_4Te_7$. This is an evidence of the large spin canting in $MnBi_2Te_4$, with an exchange coupling larger than the anisotropy, whereas this canting is rather small in $MnBi_4Te_7$, for which the anisotropy dominates. This confirms the different strength of the interlayer exchange coupling between $MnBi_2Te_4$ and $MnBi_4Te_7$.

When the field is applied at different angles, we evidenced a strong angular dependence

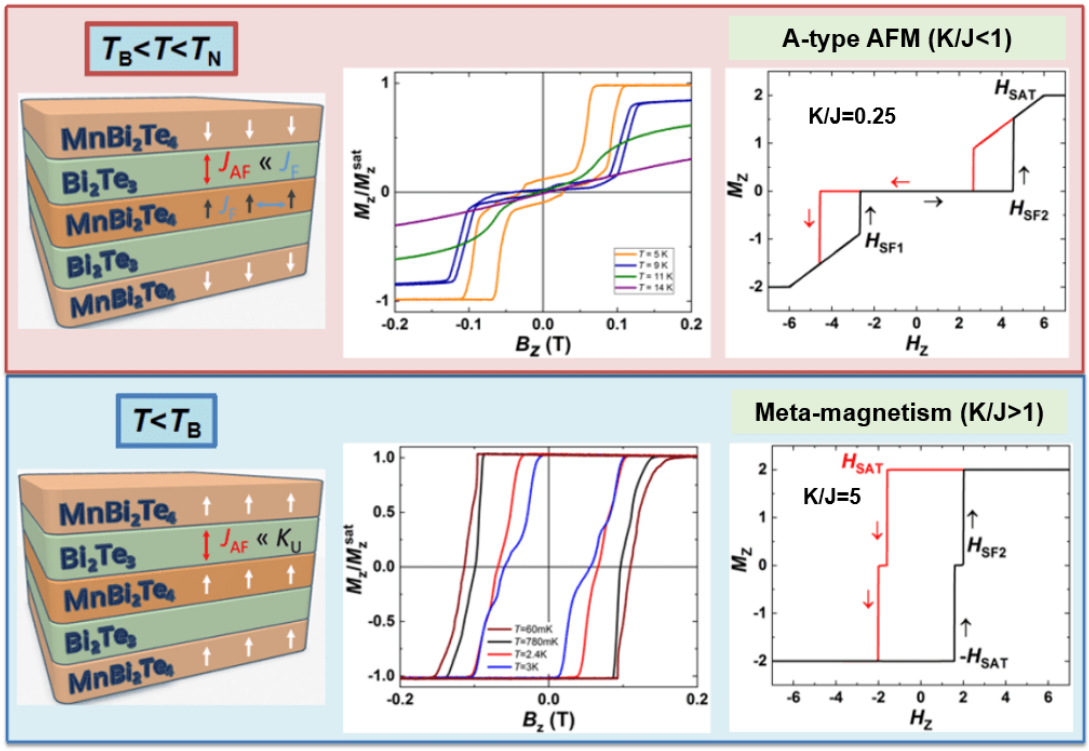

Figure 1: Magnetic hysteresis of $MnBi_2Te_4$ above and below the blocking temperature T_B. Above T_B, the interlayer exchange coupling dominates the magnetic properties. Spin-flops transitions can be observed. As the temperature decreases, the hysteresis becomes prominent. Below T_B, the effective uniaxial anisotropy is larger than the interlayer exchange. Ferromagnetic hysteresis can be observed. The figures in the rightmost column are the calculation results for the $K/J < 1$ and $K/J > 1$ cases.

for $MnBi_2Te_4$. The spin-flop transition disappeared rapidly as the field angle was increased. This is typical for antiferromagnets with dominating exchange coupling[17]. On the other hand, $MnBi_4Te_7$ has spin-flop transitions that can be observed up to large angles. This suggests the spin-flop transitions in $MnBi_4Te_7$ are no longer limited by a dominant exchange coupling.

The effective uniaxial anisotropy $K_{\text{eff}} \sim \langle M_s^2 \rangle$ increases with decreasing temperature. This leads to the significant difference of the magnetic properties between $MnBi_2Te_4$ and other weakly-coupled antiferromagnets in the $[MnBi_2Te_4][Bi_2Te_3]_n$ family. Due to the relatively weak interlayer exchange coupling in $MnBi_4Te_7$, the effective anisotropy becomes larger than the exchange coupling at lower temperature. As a consequence, $MnBi_4Te_7$ starts to develop some magnetic hysteresis already slightly below the Néel temperature. The hysteresis further expands as the temperature decreases and one switching field changes its sign (Fig. 1). At very low temperature ($\sim$0.1K), a sharp magnetization switching behavior can be observed under reversed magnetic fields, typical for a metamagnetic state, and the remnant magnetization becomes fully saturated up to a blocking temperature as high as 5K. The angular dependence of the switching field was also studied, by applying a magnetic field tilted away from the easy-anisotropy axis. In this case, the switching behavior can be observed for almost all angles, which is the signature of an anisotropy barrier. As the field angle increases, the switching field first decreases, goes to a minimum and then increases to its maximum value for the hard-axis direction. This is roughly expected from the Stoner-Wohlfarth, but with a deviation from the exact astroid when the magnetization reversal proceeds via a domain-wall nucleation propagation mechanism instead of a single-domain coherent rotation.

A bi-layer Stoner-Wohlfarth model was developed, so as to capture the basic magnetic properties of these A-type antiferromagnets. The model reveals that the magnetic state has a strong dependence on the K/J ratio. For small K/J values, the system has an AFM ground state and typical spin-flop transitions at intermediate magnetic fields. These transitions occur for small field angles only, close to the easy anisotropy direction, and they disappear for a large misalignment. As the K/J ratio increases, the magnetic hysteresis becomes more prominent. The critical spin-flop angle, at which the spin-flop transition vanishes, also becomes larger. As the magnetic anisotropy becomes larger than the exchange coupling, one spin-flop transition reverses its sign. Therefore, the magnetization at remanence remains fully saturated. Moreover, the spin canting is reduced, so that the spin-flop evolves to a spin-flip transition, and the magnetization hysteresis loop thus looks like that of a soft ferromagnet (Fig. 1). The different angular dependence in both regimes (spin-flop vs. spin-flip) is also reproduced by the model. A semi-quantitative analysis also provides an estimation of K/J for these materials. While $MnBi_2Te_4$ has a rather small K/J ratio ($\sim$0.132) at 2K, the K/J value of $MnBi_4Te_7$ has relatively strong temperature dependence and the ratio is as large as $\sim$1.2 around 4K.

It can be further concluded, according to the results obtained in this work, that other members of $[MnBi_2Te_4][Bi_2Te_3]_n$ are weakly coupled antiferromagnets and hence have a magnetization process similar to that of $MnBi_4Te_7$. Specifically, they can have Néel transitions close to 12K and ferromagnetic-like hysteresis at lower temperature which is the signature of metamagnetism. This work unveils the mechanism that drives the different magnetic states and shows that van der Waals antiferromagnets can have various magnetic properties, depending on the spacing between 2D ferromagnetic layers. For antiferromagnetic topological insulators, topological effects such as the QAHE and the quantized magnetoelectric effect can be further manipulated by their controlling their magnetic properties. The model proposed in this work can be generalized to other colinear antiferromagnets with a perpendicular-to-plane uniaxial anisotropy. Novel intrinsic MTIs with enhanced anisotropic properties and critical temperatures could therefore push the operating temperatures of QAHE devices to even higher values than those achieved with the MBT family.

Résumé étendu

Les isolants topologiques tridimensionnels (3DTI) sont des isolants non triviaux présentant des inversions de bande à certains points de haute symétrie dans l'espace réciproque. Ces matériaux ont attiré beaucoup d'attention, non seulement en raison de la nature de Dirac de leurs états topologiques de surface, mais aussi par leur texture de spin hélicoïdale spécifique. Le verrouillage spin-impulsion donne des propriétés uniques à ces quasi-particules, différentes de celles des fermions de Dirac du graphène, qui pourraient être avantageuses pour les applications en spintronique 2D (diffusion anisotrope, conversion spin-charge,...). Par ailleurs, en présence de couplages magnétiques, il est possible d'induire une bande interdite pour ces états topologiques de surface, dont la nature non triviale est associée à d'autres états quantiques topologiques, notamment l'effet Hall quantique anormal (QAHE), où la conduction est liée à des états de bords non dissipatifs sans besoin d'appliquer un champ magnétique externe (contrairement à l'effet Hall quantique QHE). Les modes de conduction 1D dans le régime QAHE sont entièrement polarisés en spin. Ils peuvent servir de sources ou de filtres de spin, et surtout comme conducteurs balistiques pour le transfert d'information. Ces modes topologiques peuvent également générer d'autres états exotiques, tels que les états de Majorana dans une hétérostructure isolant/superconducteur à effet Hall anormal[1] ou en géométrie de fil quantique[2], qui pourraientt être utiles en technologie de l'information quantique.

Coupler les états électroniques topologiques au magnétisme n'est pas une tâche évidente. Les premières tentatives de dopage par des impuretés magnétiques ont surtout conduit à un dopage électrique en volume, rendant impossible les études des états proches du point de Dirac par des mesures de magneto-transport. En 2010, il a été montré que les systèmes $(Bi, Sb)_2(Se, Te)_3$ dopés au Cr- ou au V- peuvent associer ferromagnétisme (forte susceptibilité de Van Vleck) et faibles dopages électriques, ce qui a ensuite permis de mettre en evidence la phase de QAHE [4, 5]. Cependant, l'observation ne reste possible qu'à très basse température (∼1K), ce qui complique les études, mais aussi les applications en métrologie quantiques[18, 19]. D'autres propositions basées sur le $Bi_2(Se, Te)_3$ dopé Mn[6] ou sur les effets de proximité dans les hétérostructures isolant topologique/isolant ferromagnétique[7] n'ont pas réussi à devenir des voies alternatives.

Dès 2010, un nouveau type d'isolant topologique magnétique a été proposé par Mong, Essin et Moore , en considérant l'ordre antiferromagnétique. Le matériau possède des propriétés tolologiques dépendantes de l'épaisseur de couche, selon les terminaisons magnétiques de la surface, à cause de la symétrie supplémentaire induite par le réseau magnétique. Les plans voisins les plus proches sont couplés antiferromagnétiquement et alors que les suivants sont couplés ferromagnétiquement. Cette propriété peut être relativement facile à obtenir dans les matériaux quasi-2D à liaisons van der Waals. Une propriété remarquable est un effet de parité : l'effet Hall quantique anormal existe pour un nombre impaire de couches, alors que l'état est isolant pour un nombre paire de couches avec une quantification de la conductance transverse (axion). Ces travaux ont ainsi permis d'étendre les possibilités d'études de nouvelles phases quantiques dans les isolants topologiques magnétiques avec un ordre à longue porté.

Les membres de la famille $[MnBi_2Te_4][Bi_2Te_3]_n$ (MBT) incluant $MnBi_2Te_4$ et $MnBi_4Te_7$ ont en effet été identifiés comme des isolants topologiques antiferromagnétiques[9, 10]. Il s'agit de matériaux à liaisons van der Waals (empilement de type A-B-C). Chaque couche $MnBi_2Te_4$

(un septuplet) est constituée de sept atomes avec des liaisons covalentes. A cause du couplage d'echange inter-plans antiferromagnétique, $MnBi_2Te_4$ est un matériau antiferromagnétique en volume [11]. En insérant des espaceurs non magnétiques Bi_2Te_3 (un ou plusieurs quintuplets) entre septuplets, d'autres dérivés de la famille $[MnBi_2Te_4][Bi_2Te_3]_n$ peuvent être obtenus, tels que $MnBi_4Te_7$, $MnBi_6Te_{10}$, obtenus en phase pure par croissance de monocristaux. Les calculs ab initio ont prédit l'ouverture d'une bande interdite dans la structure de bande des états de surface de ces matériaux[9, 10]. Comme les propriétés magnétiques sont intrinsèques, l'aimantation est homogène et plus importante que celle des isolants topologiques magnétiques dilués, conduisant à une bande interdite relativement plus large. Associé à leures températures de Néel relativement élevées, cela ouvre la voie à la réalisation du QAHE à des températures plus élevées. Expérimentalement, ces matériaux peuvent être obtenus par des méthodes de croissance en phase liquide à partir de mélanges de MnTe et Bi_2Te_3, pour la formation de composes eutectiques. Les mesures d'ARPES sur monocristaux ont confirmé l'ouverture de bandes interdites non triviales pour les états de surface. Les mesures SQUID ont également démontré les propriétés antiferromagnétiques [9].

En raison de l'espacement différent entre les couches magnétiques dans les deux matériaux $MnBi_2Te_4$ et $MnBi_4Te_7$ (13,6Ået 23,8Årespectivement[14]), le couplage d'échange entre couches peut être modifié. Cependant, le mécanisme qui conduit aux différentes propriétés magnétiques observées reste mal compris. Des transitions spin-flop à un champ relativement important ont été observées pour le $MnBi_2Te_4$[9]. Des transitions spin-flop similaires ont également été observées pour $MnBi_4Te_7$ près de la température de Néel, mais à une température plus basse, et une phase ferromagnétique a été rapportée[10]. L'objectif de ce travail est d'étudier les propriétés magnétiques de $MnBi_2Te_4$ et $MnBi_4Te_7$ par des mesures de magneto-transport. En effet, l'anisotropie magnétique perpendiculaire peut rendre ces antiferromagnétiques différents les uns des autres. Dans ce travail, une étude générale sur le rôle relatif de l'anisotropie magnétique uniaxiale et du couplage d'échange entre couches dans les antiferromagnétiques colinéaires de type A est conduite.

Pour la préparation des échantillons, des monocristaux ont été élaborés par le groupe d'Anna Isaeva à la TU Dresden, puis nous les avons exfolié mécaniquement et transféré sur des substrats SiO_2/Si++. Des nanostructures d'une épaisseur comprise entre 20nm et 100nm ont été obtenues. La lithographie par faisceau d'électrons a été utilisée pour obtenir des contacts ohmiques, puis pour réaliser la géométrie de Hall des échantillons. Des mesures de magnétotransport ont été effectuées dans une plage de température de 0,1∼300K, en utilisant des champs magnétiques vectoriels 2D (1T-12T) ou 3D (2T-2T-6T).

La dépendance en température de la résistivité des composés $MnBi_2Te_4$ et $MnBi_4Te_7$ montre un comportement métallique. Ceci est typique des matériaux présentant un certain désordre atomique, similaire au cas des isolants topologiques 3D non magnétiques, avec ici des substitutions cationiques entre Bi et Mn proches voisins, en plus du désordre des anions (lacunes, interstitiels, anti-sites). Un maximum de résistivité est observé à la transition de phase (divergence des fluctuations à la température de Néel, conduisant à une plus faible mobilité des porteurs libres) . La température de Néel est de 23.5K pour $MnBi_2Te_4$ et de 12.5K pour $MnBi_4Te_7$, alors que leur température de Curie-Weiss, obtenue par des mesures d'aimantation, est respectivement de 1K et 12K. En modèle de champ moyen, le rapport de ces températures donne une indication sur la force relative descouplages d'échange intra-plans et inter-plans. Un calcul simple suggère que le couplage antiferromagnétique inter-plan est environ vingt fois plus faible dans $MnBi_4Te_7$ que dans $MnBi_2Te_4$, ce qui est cohérent avec la presence d'un espaceur non magnétique et un mécanisme d'échange à courte portée[16].

En appliquant un champ magnétique le long de l'axe d'anisotropie facile, la transition de reorientation de spin (spin-flop) peut être identifiée par des sauts de résistivité longitudinale et transverse. D'une manière générale, $MnBi_2Te_4$ présente un champ de transition spin-flop plutôt important (∼3,2T à 2K) comparé à celui de $MnBi_4Te_7$ (∼0,1T à 10K). Un bon ordre de grandeur

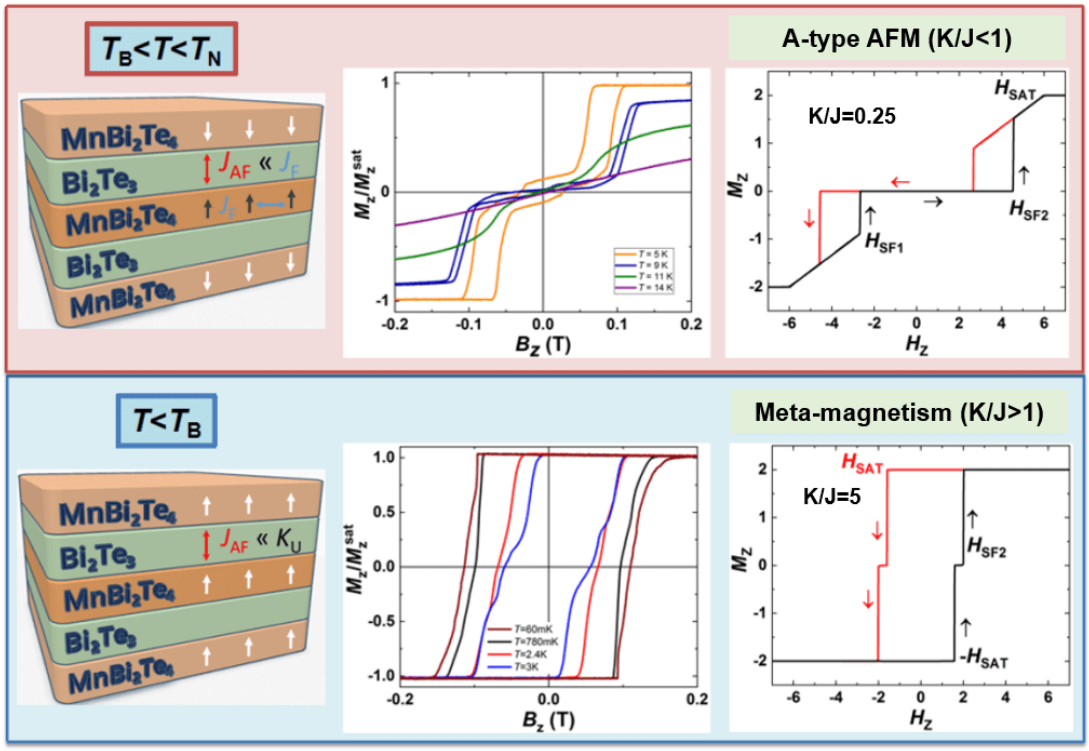

Figure 2: Hystérésis magnétique du $MnBi_2Te_4$ au-dessus et en dessous de la température de blocage T_B. Au-dessus de T_B, le couplage d'échange entre couches domine les propriétés magnétiques. Des transitions spin-flops peuvent être observées. Lorsque la température diminue, l'hystérésis devient proéminente. En dessous de T_B, l'anisotropie uniaxiale effective est plus grande que l'échange entre couches. Une hystérésis ferromagnétique peut être observée. Les chiffres de la colonne la plus à droite sont les résultats des calculs pour les cas $K/J < 1$ et $K/J > 1$.

de ce champ de transition peut être estimé à partir du produit de l'anisotropie uniaxiale K et du couplage d'échange inter-plans J, avec $B_{\rm sf} \sim \sqrt{JK}$. En supposant que l'anisotropie est similaire dans les deux matériaux (même environnement de champ cristallin), ce résultat confirme que le couplage d'échange est beaucoup plus faible dans $MnBi_4Te_7$. De plus, la différence entre le champ de saturation et celui de la transition de spin-flop est grande dans $MnBi_2Te_4$ ($B_{\rm sat}$ ~6.9T à 2K), alors que ces deux champs sont presque identiques dans $MnBi_4Te_7$. Cette différence est la signature d'un couplage d'échange plus grand que l'anisotropie ($J > K$) dans $MnBi_2Te_4$, avec un important écart à la colinéarité, alors que l'aimantation des sous-réseaux reste proche de l'axe facile dans $MnBi_4Te_7$, pour lequel l'anisotropie domine ($K > J$).

Une autre signature des différents régimes ($J < K$ ou $J > K$) est mise en évidence dans la dépendance angulaire des champs de transition, en appliquant un champ incliné par rapport à l'axe d'anisotropie uniaxiale. Pour $MnBi_2Te_4$, la transition spin-flop disparaît rapidement lorsque l'angle augmente, un comportement typique des matériaux antiferromagnétiques avec un couplage d'échange dominant[17]. Au contraire, $MnBi_4Te_7$ présente des transitions qui peuvent être observées jusqu'à de grands angles, comme attend pour un couplage d'anisotropie dominant.

L'anisotropie uniaxiale effective $K_{\rm eff} \sim \langle M_s^2 \rangle$ augmente avec la diminution de la température. Ceci conduit à une différence significative des propriétés magnétiques entre $MnBi_2Te_4$ et les autres antiferromagnétiques, plus faiblement couples, de la famille $[MnBi_2Te_4][Bi_2Te_3]_n$. En raison du couplage d'échange intercouche relativement faible dans le $MnBi_4Te_7$, l'anisotropie effective domine à basse temperature, et les cycles d'aimantation deviennent rapidement non réversiblesen dessous de la température de Néel. L'hystérésis se développe à plus basse temper-

ature, et l'aimantation rémanente devient non nulle lorsqu'un champ de renversement change de signe (Fig. 2), définissant alors une temperature de blocage (de l'ordre de 5K dans $MnBi_4Te_7$).Les cycles d'hystérésis ressemblent alors à ceux d'un matériau ferromagnétique, mais c'est bien un état métamagnétique qui s'est formé dans le régime $K > J$. A très basse temperature, la dépendance angulaire du champ coercitif correspond bien à la signature d'une barrière d'anisotropie uniaxiale. En function de l'angle du champ appliqué, le champ coercitif diminue d'abord, passe à un minimum puis augmente jusqu'à sa valeur maximale pour la direction correspondant à l'axe difficile. Le lieu des champs de retournement de l'aimantation correspond à peu près à une astroïde de Stoner-Wohlfarth, sauf aux petits angles, lorsque la rotation coherent est faible et que le renversement de l'aimantation est induit par un mécanisme de nucléation/propagation de parois de domaines, ce qui donne une astroïde tronquée.

Un modèle de Stoner-Wohlfarth à deux couches a été développé, afin de reproduire les propriétés magnétiques de base de ces composes antiferromagnétiques colinéaires (type A). Ce modèle simple révèle que l'état magnétique dépend fortement du rapport K/J. Pour $K/J \ll 1$, l'état fondamental est AFM et les cycles d'aimantation évoluent vers un état d'aimantation incline au delà du champ de transition spin-flop à des champs magnétiques intermédiaires (de l'ordre de quelques Tesla). Ces transitions se produisent uniquement pour des champs proches de la direction d'anisotropie facile, et elles disparaissent en champ incliné. Lorsque le rapport K/J augmente, l'hystérésis magnétique devient plus importante, et deux champs de transition spin-flop sont identifiés. L'angle critique au delà duquel la transition spin-flop disparaît augmente également. Lorsque l'anisotropie magnétique devient plus grande que le couplage d'échange, l'une des transitions spin-flop, celle qui correspond à l'évolution d'un état aligné vers un état anti-aligné des sous-reseaux magnétique, change de signe. Par conséquent, l'aimantation rémanente reste entièrement saturée. De plus, l'orientation relative des aimantations de sous-réseaux est si réduite à la transition spin-flop que celle-ci évolue plutôt vers une transition de type spin-flip, et le cycle d'hystérésis de l'aimantation ressemble donc à celle d'un ferromagnétique doux (Fig. 2). La dépendance angulaire différente dans les deux régimes (spin-flop vs. spin-flip) est également bien reproduite par le modèle. Une analyse semi-quantitative fournit aussi une estimation des valeurs K/J, pour chaque matériau. Alors que $MnBi_2Te_4$ présente un rapport K/J plutôt faible ($\sim$0,132) à 2K, la valeur K/J de $MnBi_4Te_7$ présente une dépendance relativement forte avec la température et le rapport évolue vers un maximum à $\sim$1,2 à basse temperature, au dessous de 4K environ..

On peut également conclure, d'après les résultats obtenus dans ce travail, que les autres membres de $[MnBi_2Te_4][Bi_2Te_3]_n$ sont aussi des antiferromagnétiques faiblement couplés et ont donc un processus d'aimantation similaire à celui de $MnBi_4Te_7$. Plus précisément, ils ont des transitions de Néel proches de 12K et une hystérésis de type ferromagnétique à plus basse température qui est la signature du métamagnétisme. Ce travail dévoile le mécanisme qui régit les différents états magnétiques et montre que les matériaux magnétiques 2D à liaisons de Van der Waals peuvent avoir diverses propriétés magnétiques, en fonction du signe du couplage d'échange inter-plans et aussi de l'espacement entre les couches ferromagnétiques 2D. Pour les isolants topologiques antiferromagnétiques, les effets topologiques tels que le QAHE et l'effet magnétoélectrique quantifié devraient pouvoir être facilement manipulés à faibles champs, notamment dans les situations où l'anisotropie domine. Le modèle proposé dans ce travail peut être généralisé à d'autres antiferromagnétiques colinéaires avec une anisotropie uniaxiale perpendiculaire au plan, et a été facilement étendu au delà du simple cas à deux couches. De nouveaux MTI intrinsèques avec des propriétés anisotropes et des températures critiques améliorées pourraient donc pousser les températures de fonctionnement des dispositifs QAHE à des valeurs encore plus élevées que celles atteintes avec la famille MBT. Par ailleurs, l'étude du transport quantique dans des nanostructures ultra-fines (à quelques plans empilés) devrait révéler une richesse de comportements liés au détail microscopique des textures magnétiques.

Erweiterter Zusammenfassung

Dreidimensionale topologische Isolatoren (3DTIs) sind nicht-triviale Isolatoren mit Bandinversionen an bestimmten hochsymmetrischen Punkten im k-Raum. Die Materialien haben nicht nur wegen der Dirac-Natur der topologischen Oberflächenzustände, sondern auch wegen ihrer spezifischen helikalen Spintextur viel Aufmerksamkeit auf sich gezogen. Das Spindrehimpuls-Locking verleiht diesen Quasiteilchen einzigartige Eigenschaften, die sich von denen in Graphen unterscheiden und die für 2D-Spintronik-Anwendungen von Nutzen sein können. Die Kopplung von topologischen Oberflächenzuständen mit Magnetismus kann eine nicht-triviale Lücke am Dirac-Punkt induzieren, die weitere neuartige Physik wie den Quanten-Anomal-Hall-Effekt (QAHE) ermöglicht, bei dem ein verlustfreier Ladungstransport in 1D-Kantenzuständen ohne Anlegen eines externen Magnetfeldes erreicht werden kann (im Gegensatz zum bekannten Quanten-Hall-Effekt, QHE). Die leitfähigen Kanäle im QAHE-Regime können, da sie vollständig spinpolarisiert sind, als reine Spinquellen und Spinfilter und vor allem als ballistische Leiter für die Informationsübertragung dienen. Diese topologischen Kanäle können auch andere exotische Zustände erzeugen, wie Majorana-Zustände in einer anomalen Hall-Isolator/Supraleiter-Heterostruktur[1] oder in der Quantendraht-Geometrie[2], die weiter zur Quantenberechnung eingesetzt werden können.

Die Suche nach experimentellen Methoden, um die Oberflächenzustände in einem topologischen 3D-Isolator effizient mit Magnetismus zu koppeln, war ein langer Lauf. Die Aufgabe war anfangs erschwert, da die Dotierung topologischer Isolatoren mit magnetischen Elementen auch die Bulk-Ladungsträgerdichte erhöhen kann, was den Nachweis der neuartigen topologischen Eigenschaften von Oberflächenzuständen mit Bandlücke erschwert. Im Jahr 2010 wurde herausgefunden, dass Cr- oder V-dotierte $(Bi, Sb)_2(Se, Te)_3$-Systeme von der großen Van-Vleck-Suszeptibilität profitieren und daher eine langreichweitige magnetische Ordnung aufweisen können, ohne dass eine große Bulk-Leitfähigkeit eingeführt wird[3]. Der QAHE wurde später in diesen Systemen realisiert[4, 5]. Allerdings war die Beobachtung nur bei sehr niedrigen Temperaturen (∼0,1K) möglich, was die Untersuchung dieser Physik erschwerte. Andere Vorschläge, die auf Mn-dotiertem $Bi_2(Se, Te)_3$[6] oder auf Proximity-Effekten in topologischen Isolator/Ferromagnet-Isolator-Heterostrukturen[7] basieren, scheiterten als alternative Wege.

Ein neuer Typ von magnetischen topologischen Isolatoren wurde 2010 von R. S. K. Mong et al. vorgeschlagen[8], unter Berücksichtigung von antiferromagnetischer Ordnung. Das Material hat schichtabhängige magnetische Eigenschaften, abhängig von magnetischen Oberflächenabschlüssen. Die nächstbenachbarten Schichten sind antiferromagnetisch gekoppelt und die nächsten Nachbarn sind ferromagnetisch gekoppelt. Diese schichtweise Eigenschaft ist in van-der-Waals-Materialien relativ leicht zu erreichen. Wenn der Magnetismus mit den topologischen Oberflächenzuständen koppelt, können je nach Parität der Schichten verschiedene topologische Zustände existieren: der quantenanomale Hall-Zustand existiert in den ungeradzahligen Schichten und der Axion-Isolator-Zustand in den geradzahligen Schichten. Damit wurden die Untersuchungen der magnetischen topologischen Isolatoren von ferromagnetischen Materialien auf antiferromagnetische Materialien erweitert.

Die Mitglieder der $[MnBi_2Te_4][Bi_2Te_3]_n$ (MBT) einschließlich $MnBi_2Te_4$ und $MnBi_4Te_7$ wurden als antiferromagnetische topologische Isolatoren identifiziertOtrokovDresden2019, Vidal2019.

Es handelt sich um van-der-Waals-Materialien, bei denen sich die Schichten in A-B-C-Manier stapeln. Jede $MnBi_2Te_4$-Schicht (eine Septupelschicht) besteht aus sieben Atomen mit kovalenten Bindungen. Die oben erwähnten schichtabhängigen magnetischen Eigenschaften werden in solchen Systemen erwartet[11]. Das Bulk-$MnBi_2Te_4$ ist also ein Antiferromagnet. Durch Einfügen von nichtmagnetischenBi_2Te_3-Spacerschichten zwischen den Septupelschichten können andere Derivate der $[MnBi_2Te_4][Bi_2Te_3]_n$-Familie erhalten werden, wie $MnBi_4Te_7$, $MnBi_6Te_{10}$ und andere. Durch Ab-Initio-Rechnungen wurden die gegappten Oberflächenzustände dieser Materialien vorhergesagtOtrokovDresden2019, Vidal2019. Da die magnetischen Eigenschaften in diesen Materialien nicht durch extrinsische Dotierung eingebracht werden und die Materialien im Idealfall homogen gewachsen eine größere Magnetisierung im Vergleich zu dotiert magnetischen topologischen Isolatoren aufweisen, kann in diesen Materialien eine relativ große Bandlücke existieren. Zusammen mit ihren relativ hohen Néel-Temperaturen ebnet dies den Weg, den QAHE bei höheren Temperaturen zu erreichen. Experimentell können diese Materialien durch Bulk-Kristallwachstumsmethoden von eutektischen Verbindungen erhalten werden, die aus der Schmelze von MnTe- und Bi_2Te_3-Gemischen gebildet werden. ARPES-Messungen an den Kristallen bestätigten die Öffnung von nicht-trivialen Bandlücken an den Oberflächenzuständen. SQUID-Messungen zeigten auch die antiferromagnetischen Eigenschaften der Proben[9].

Aufgrund der unterschiedlichen Abstände zwischen den magnetischen Schichten in den beiden Materialien $MnBi_2Te_4$ und $MnBi_4Te_7$ (13,6Åbzw. 23,8Å), kann die Zwischenschicht-Austauschkopplung variiert werden. Der eigentliche Mechanismus, der die unterschiedlichen magnetischen Eigenschaften zwischen den verschiedenen Mitgliedern von $[MnBi_2Te_4][Bi_2Te_3]_n$ antreibt, wurde jedoch nicht gut verstanden. Für $MnBi_2Te_4$ wurden Spin-Flop-Übergänge bei relativ großen Feldern beobachtetOtrokovDresden2019. Ähnliche Spin-Flop-Übergänge wurden auch für $MnBi_4Te_7$ in der Nähe der Néel-Temperatur beobachtet, aber bei niedrigeren Temperaturen wurde ferromagnetisches Verhalten berichtet[10]. Ziel der vorliegenden Arbeit ist es, die magnetischen Eigenschaften von $MnBi_2Te_4$ und $MnBi_4Te_7$ mit Hilfe von Transportmessungen zu untersuchen. Durch die senkrechte magnetische Anisotropie können sich diese Antiferromagneten voneinander unterscheiden. In dieser Arbeit wird eine allgemeine Diskussion über die relative Rolle der uniaxialen magnetischen Anisotropie und der Zwischenschicht-Austauschkopplung in kolinearen A-Typ-Antiferromagneten geführt.

Für die Probenpräparation wurden Bulk-Kristalle, die in der Gruppe von Anna Isaeva an der TU Dresden gewachsen sind, mechanisch exfoliert und auf SiO_2/Si++-Substrate übertragen. Es wurden Nanostrukturen mit Dicken zwischen 20nm und 100nm hergestellt. Mittels Elektronenstrahllithographie wurden ohmsche Kontakte hergestellt und anschließend die Hall-Geometrie der Proben strukturiert. Magnetotransportmessungen wurden in einem Temperaturbereich von 0,1∼300K unter Verwendung von 2D/3D-Vektormagnetfeldern durchgeführt.

Die Temperaturabhängigkeit des Längswiderstandes von sowohl $MnBi_2Te_4$ als auch $MnBi_4Te_7$ zeigt ein metallisches Verhalten. Dies ist typisch für Materialien mit einer gewissen strukturellen Unordnung, ähnlich wie im Fall der nicht-magnetischen topologischen 3D-IsolatorenLVeyrat2015, hier aber möglicherweise aufgrund der Vermischung von Bi und Mn, zusätzlich zur Unordnung der Anionen. Widerstandsspitzen wurden bei Néel-Temperaturen beobachtet, wo große Spin-Fluktuationen existieren. Die Néel-Temperatur beträgt 23K für $MnBi_2Te_4$ und 12K für $MnBi_4Te_7$. Der Vergleich der Néel-Temperatur mit der Curie-Weiss-Temperatur beider Materialien gibt uns einen Anhaltspunkt über die relative Stärke ihrer Zwischenschicht-Austauschkopplung. Nach der Molekularfeldtheorie hängt die relative Stärke der Zwischenschicht-Austauschkopplung mit dem Verhältnis zwischen der Curie-Weiss-Temperatur und der Néel-Temperatur zusammen. Eine einfache Berechnung deutet auf eine viel schwächere Zwischenschicht-Austauschkopplung in $MnBi_4Te_7$ hin, was mit dem großen Abstand zwischen den magnetischen Schichten konsistent ist[16].

Beim Schwenken des Feldes entlang der einfachen Achse können magnetische Übergänge mit deutlichen Änderungen sowohl des Längswiderstandes als auch des Querwiderstandes identifiziert

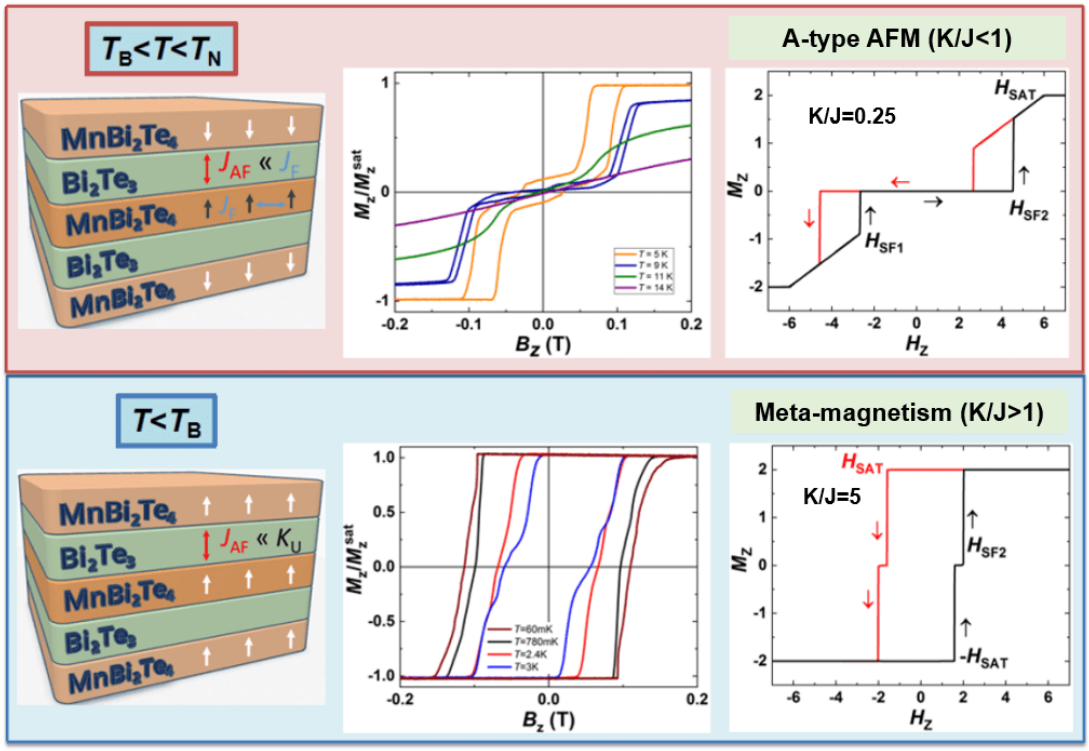

Figure 3: Magnetische Hysterese von $MnBi_2Te_4$ oberhalb und unterhalb der Blockierungstemperatur T_B. Oberhalb T_B dominiert die Zwischenschicht-Austauschkopplung die magnetischen Eigenschaften. Es können Spin-Flop-Übergänge beobachtet werden. Mit abnehmender Temperatur tritt die Hysterese in den Vordergrund. Unterhalb von T_B ist die effektive uniaxiale Anisotropie größer als der Zwischenschichtaustausch. Es ist eine ferromagnetische Hysterese zu beobachten. Die Abbildungen in der Spalte ganz rechts sind die Berechnungsergebnisse für die Fälle $K/J < 1$ und $K/J > 1$.

werden. Im Allgemeinen hat $MnBi_2Te_4$ ein ziemlich großes Spin-Flop-Übergangsfeld (∼3.2T bei 2K) im Vergleich zu $MnBi_4Te_7$ (∼0.1T bei 10K). Das Spin-Flop-Übergangsfeld kann mit der Anisotropie und der Austauschkopplungsstärke $B_{\mathrm{sf}} \sim \sqrt{JK}$ grob abgeschätzt werden. Unter der Annahme, dass die Anisotropie in beiden Materialien ähnlich ist, kann man sehen, dass die Austauschkopplung in $MnBi_4Te_7$ viel schwächer sein wird. Außerdem ist der Unterschied zwischen dem Sättigungsfeld und dem Spin-Flop-Übergang in $MnBi_2Te_4$ groß (B_{sat} ∼6.9T bei 2K), während die beiden Übergänge bei $MnBi_4Te_7$ fast bei demselben Feld liegen. Dies ist ein Beweis für die große Spin-Verkantung in $MnBi_2Te_4$, mit einer Austausch-Kopplung, die größer ist als die Anisotropie, während diese Verkantung in $MnBi_4Te_7$, in welchem die Anisotropie dominiert, eher klein ist. Dies bestätigt die unterschiedliche Stärke der Zwischenschicht-Austauschkopplung zwischen $MnBi_2Te_4$ und $MnBi_4Te_7$.

Durch Variieren des Winkels des angelegten Magnetfelds konnten wir eine starke Winkelabhängigkeit für $MnBi_2Te_4$ nachweisen. Der Spin-Flop-Übergang verschwand schnell, als der Feldwinkel erhöht wurde. Dies ist typisch für Antiferromagneten mit dominierender AustauschkopplungBogdanov2007. Andererseits gibt es bei $MnBi_4Te_7$ Spin-Flop-Übergänge, die bis zu großen Winkeln beobachtet werden können. Dies deutet darauf hin, dass die Spin-Flop-Übergänge in $MnBi_4Te_7$ nicht mehr durch eine dominante Austauschkopplung begrenzt sind.

Die effektive uniaxiale Anisotropie $K_{\mathrm{eff}} \sim \langle M_s^2 \rangle$ nimmt mit abnehmender Temperatur zu. Dies führt zu dem signifikanten Unterschied der magnetischen Eigenschaften zwischen $MnBi_2Te_4$ und anderen schwach gekoppelten Antiferromagneten in der $[MnBi_2Te_4][Bi_2Te_3]_n$-Familie. Auf-

grund der relativ schwachen Zwischenschicht-Austauschkopplung in $MnBi_4Te_7$ wird die effektive Anisotropie bei niedrigeren Temperaturen größer als die Austauschkopplung. Infolgedessen beginnt $MnBi_4Te_7$ bereits knapp unterhalb der Néel-Temperatur eine gewisse magnetische Hysterese zu entwickeln. Die Hysterese vergrößert sich weiter, wenn die Temperatur sinkt und ein Schaltfeld sein Vorzeichen wechselt (Fig. 3). Bei sehr niedriger Temperatur (∼0,1K) kann ein scharfes Magnetisierungsschaltverhalten unter umgekehrten Magnetfeldern beobachtet werden, typisch für einen metamagnetischen Zustand, und die Restmagnetisierung wird bis zu einer Blockierungstemperatur von 5K vollständig gesättigt. Die Winkelabhängigkeit des Schaltfeldes wurde ebenfalls untersucht, indem ein von der Achse der leichten Anisotropie weg geneigtes Magnetfeld angelegt wurde. In diesem Fall kann das Schaltverhalten für fast alle Winkel beobachtet werden, was die Signatur einer Anisotropie-Barriere ist. Mit zunehmendem Feldwinkel nimmt das Schaltfeld zunächst ab, geht auf ein Minimum und steigt dann auf seinen Maximalwert für die Hart-Achsen-Richtung an. Dies wird grob von der Stoner-Wohlfarth erwartet, jedoch mit einer Abweichung vom exakten Astroiden, wenn die Magnetisierungsumkehr über einen Domänenwand-Keimausbreitungsmechanismus anstelle eines Einzeldomänenverhaltens verläuft.

Es wurde ein Zweischicht-Stoner-Wohlfarth-Modell entwickelt, um die grundlegenden magnetischen Eigenschaften dieser A-Typ-Antiferromagneten zu erfassen. Das Modell zeigt, dass der magnetische Zustand eine starke Abhängigkeit vom K/J-Verhältnis hat. Für kleine K/J-Werte hat das System einen AFM-Grundzustand und typische Spin-Flop-Übergänge bei mittleren Magnetfeldern. Diese Übergänge treten nur für kleine Feldwinkel auf, nahe der einfachen Anisotropierichtung, und sie verschwinden für einen großen Versatz. Mit steigendem K/J-Verhältnis wird die magnetische Hysterese deutlicher. Der kritische Spin-Flop-Winkel, bei dem der Spin-Flop-Übergang verschwindet, wird ebenfalls größer. Wenn die magnetische Anisotropie größer wird als die Austauschkopplung, kehrt ein Spin-Flop-Übergang sein Vorzeichen um. Daher bleibt die Magnetisierung bei Remanenz vollständig gesättigt. Außerdem wird die Spin-Verkantung reduziert, so dass der Spin-Flop in einen Spin-Flip-Übergang übergeht und die Magnetisierungshystereseschleife somit wie die eines weichen Ferromagneten aussieht (Fig. 3). Auch die unterschiedliche Winkelabhängigkeit in beiden Regimen (Spin-Flop vs. Spin-Flip) wird durch das Modell reproduziert. Eine semi-quantitative Analyse liefert auch eine Abschätzung von K/J für diese Materialien. Während $MnBi_2Te_4$ ein eher kleines K/J-Verhältnis (∼0,132) bei 2K aufweist, hat der K/J-Wert von $MnBi_4Te_7$ eine relativ starke Temperaturabhängigkeit und das Verhältnis ist ∼1,2 um 4K.

Aus den in dieser Arbeit gewonnenen Ergebnissen lässt sich ferner schließen, dass andere Verbindungen von $[MnBi_2Te_4][Bi_2Te_3]_n$ schwach gekoppelte Antiferromagneten sind und daher einen ähnlichen Magnetisierungsprozess wie $MnBi_4Te_7$ aufweisen. Insbesondere können sie Néel-Übergänge in der Nähe von 12K und eine ferromagnetisch-ähnliche Hysterese bei niedrigeren Temperaturen aufweisen, was typisch für Metamagnetismus ist. Diese Arbeit enthüllt den Mechanismus, der die verschiedenen magnetischen Zustände antreibt und zeigt, dass van-der-Waals-Antiferromagnete verschiedene magnetische Eigenschaften haben können, abhängig vom Abstand zwischen den 2D-ferromagnetischen Schichten. Bei antiferromagnetischen topologischen Isolatoren können topologische Effekte wie der QAHE und der quantisierte magnetoelektrische Effekt durch die Steuerung ihrer magnetischen Eigenschaften weiter manipuliert werden. Das in dieser Arbeit vorgeschlagene Modell kann auf andere kolineare Antiferromagnete mit einer senkrecht zur Ebene verlaufenden uniaxialen Anisotropie verallgemeinert werden. Neuartige intrinsische MTIs mit verbesserten anisotropen Eigenschaften und kritischen Temperaturen könnten daher die Betriebstemperaturen von QAHE-Bauteilen auf noch höhere Werte treiben, als sie mit der MBT-Familie erreicht werden.

Acknowledgements

I thank Prof. Büchner, IFW and SPINTEC for offering the opportunity to join such a wonderful project in my doctoral study. The two institutes provide good facilities and hold many nice and friendly colleagues. These have helped a lot during my work. Both sides also offered great assistance for my travel between Grenoble and Dresden, particularly during the time of pandemic.

I thank my supervisor Dr. Romain Giraud for many, of which I can hardly list all. I have always been missing the time when he explained the concept of things, the basic theories or discussed other details on the pieces of paper or on white broads. I would have learned much less if there were not his words full of patience. I also remember the time when he helped me with my travel between Grenoble and Dresden. He drove me in downtown of Grenoble and helped the one who has little French knowledge to figure out all kinds of administrative stuff. And I think there are much more to mention for his help in my experiments, for example the samples he prepared in Grenoble when I was not there... And as I said, I can hardly list all of them.

I would say the time I have spent with the lovely colleagues of quantum transport group, Valentin Labracherie, Teresa Tschiner, Arthur Veyrat and others was wonderful. There were difficulties, both in work and in life, but the group was full of joy. I am grateful for the atmosphere these super cute colleagues have maintained. Particularly I would like to thank Valentin Labracherie and Arthur Veyrat for their help in my experiments. In fact, some of the results presented in the manuscript would not be available if there were not their help. I also give special thanks to Michael Wißmann for the German grammar checking.

I will also not forget the help offered by many other colleagues in the two institutes. Dr. Joseph Dufouleur and Olivier Fruchart have offered good advice during my work. Laurent Vila and Jean-Luc Thomassin offered great help for the lithography processes. I have to mention sometimes these processes are really bothersome and nevertheless they have helped with great patience. They also gave good advice for other sample preparation processes. I thank Irène Peck for cutting substrates. I thank Aurélien Olivier for helping me to use the metallization chamber and the ion beam etching chamber. I thank Barbara Eichler and Sandra Nestler for their help in the nanofabrication in IFW. I thank Isabelle Joumard for organizing the measurements on PPMS, also for her help to solve the problems of the devices. I thank Robert Morel for organizing the AFM measurements, also for the tools he provided. I thank Catherine Broisin, Rita Taubert and Kerstin Höllerer and other colleagues in the two institutes for their friendly help with administrative issues. I thank Anna Isaeva and her team for preparing the crystals. I thank Vincent Baltz and Philippe Ballet for their feedback on my work. I also give thanks to other colleagues whom I haven't mentioned here.

I give thanks to my closest friends in Dresden, Au Yeung Kwan Ho and Tsai Yun-Yen. I am grateful for their care even I was staying in Grenoble. I also thank the support and prayers from them and other members in the Dresden fellowship in the Grenoble fellowship. Particularly I want to thank the support of Moses Tan, who gave great care for someone like me who had not

many friends in Grenoble.

I owe my parents a lot. I have kept them untended for a long time in China, whereas they tried their best to provide the support I need. I was stubborn and didn't care enough for them. Now I would like to give my sincere gratefulness to them, for their patience as for long they have been waited, for their endurance as the loneliness and the indifference they have suffered, for their kindness as they valued my choice and satisfied my needs in a foreign country.

Thank you!

Contents

List of Acronyms

2DEG two-dimensional electron gas

AHE anomalous Hall effect

ARPES angle resolved photoemission spectroscopy

MBE molecular beam epitaxy

MOSFET metal-oxide-semiconductor field-effect transistor

PXRD powder X-ray diffraction

QAHE quantum anomalous Hall effect

QHE quantum Hall effect

QSHE quantum spin Hall effect

RKKY Ruderman-Kittel-Kasuya-Yosida

RRR residual resistivity ratio

SCXRD single-crystal X-ray diffraction

SEM scanning electron microscope

SHE spin Hall effect

SQUID superconducting quantum interference device

TEM transmission electron microscope

VSM vibrating-sample magnetometer

VTI variable temperature insert

Chapter 1

Introduction

1.1 State-of-art

There have been extensive studies and efforts dedicated to enhancing the performance of transistors since the 1950s. One important factor of the performance of transistors is the "on-off" efficiency. Although the concept of the field-effect transistor can be traced back to 1926, when Julius Edgar Lilienfeld proposed the first field-effect transistor, it was not until the 1960s that the first practical field-effect transistor, the first metal-oxide-semiconductor field-effect transistor (MOSFET), was invented[20]. This achievement has been a key to the development of very-large-scale integration in classical electronic devices, which had been limited for more bulky bipolar junction transistors. Afterwards, the invention rapidly boosted the silicon industry and the massive production of semiconductors. Nowadays, the Moore's law, which states that the density of transistors in an integrated circuit doubles every two years, is still properly fulfilled, as confirmed in the latest so-called 5nm technology node. In a MOSFET, the thickness of the conductive channel (or inversion layer) between the source and the drain can be modulated by the gate voltage. Thus, a quasi-two-dimensional electron gas (2DEG) system can be formed at the interface between the gate oxide and depletion layer.

In fundamental research, 2DEGs can be created in different ways and they were found to be of great interest for the studies of many physical properties, such as quantized resistance, fractional charges *etc.*. In such systems, 2D quasi-particles are confined in a potential well, and due to the quantum confinement in the of the third dimension, their transverse energy is quantized. Under an external magnetic field applied perpendicular to the electronic plane, the orbital energy levels are further split into Landau levels. In this case, the Hall resistance can be quantized, which is known as the quantum Hall effect (QHE). In the quantum Hall state, 1D conductive channels are formed at the edges of the insulating 2D system. This results in dissipationless charge transport in large magnetic fields, and reduced quasi-particle scattering by disorder. Interestingly, the QHE was first discovered also on a MOSFET[21]. Soon afterwards, modulation doping AlGaAs heterostructures, with ultra-high mobilities (exceeding 10^6 $cm^2V^{-1}s^{-1}$) and low carrier densities (as low as 10^{11} cm^{-2}) have lead to tremendous results, for instance with the discovery of the fractional QHE and of non-trivial band topology.[22, 23].

Confined electronic systems can also exist in truly 2D materials. In the past, free standing 2D materials were considered thermodynamically unstable. This has been changed since 2004 when few-layer carbon films, which are now known as graphene, were fabricated. Thanks to the relatively weak van der Waals interaction between 2D layers in graphite, K. S. Novoselov and A. K. Geim *et al.* were able to exfoliate graphene from highly oriented pyrolytic graphite[24]. Graphene has a gapless metallic band structure, with Dirac quasiparticles, and a remarkably large mobility ($\sim$ 1000 $cm^2V^{-1}s^{-1}$) and mean free path at room temperature. Important efforts have been dedicated to improving the carrier mobility at low temperature, since scattering by disorder

remains important, and values in the order of 10^5 $cm^2V^{-1}s^{-1}$ were achieved with suspended graphene[25]. In the vicinity of the Dirac point, linear dispersion of massless quasiparticles leads to novel properties when compared to massive 2DEGs. For instance, due to the reduced scattering by phonons, the QHE was evidenced at room temperature[26].

Early works on the QHE and the discovery of the quantum spin Hall effect (QSHE) later revealed the importance of gauge fields and geometric phases on electronic band structures. It was realized that not all the band gaps are equivalent, and insulators can belong to different classes with trivial or non-trivial topology. Topological invariants including the Chern number and the additional $\mathbb{Z}_2$ topological invariant were assigned to materials in order to describe the nontriviality of the band gaps[27]. In $\mathbb{Z}_2$ insulators, the spin-rotation symmetry is broken but the time-reversal symmetry is preserved. Therefore, topological states exist in zero magnetic field, which is in contrast to the case of the QHE. These novel states can be realized in materials with large spin-orbit coupling, and it was soon identified that it is related to the band-inversion mechanism, which leads to gapless states at boundaries. The topological phase was first observed in 2D materials (such as HgTe quantum well[28]), unveiling the quantum spin Hall state, a state with counter-propagating 1D metallic modes of opposite spin states. Contrary to graphene, due to the preserved time-reversal symmetry, the Chern number and the Hall resistivity in such systems should vanish. However, due to their helical spin texture, the spins are locked perpendicularly to the momentum direction. The direct backscattering by non-magnetic disorder is suppressed and quantum spin Hall edge states are dissipationless. These interesting properties of $\mathbb{Z}_2$ topological insulators further motivated some new research to propose novel concepts for proximity-induced Majorana modes or spintronic devices and spintronics applications in such systems[29].

Because the spins can be manipulated independently with the charge, processing units with faster speed and lower power consumption can be realized using spintronics techniques. In the last decade, researchers have taken advantage of spin-orbit coupling to control spin states and currents in a new generation of spintronic devices. In particular, a lot of efforts were dedicated to identify efficient mechanisms in order to manipulate the spin degree of freedom not only in magnetic but also in non-magnetic electronic devices. Nevertheless, the "on-off" efficiency of spintronic devices nowadays is still limited, which may due to the absence of pure spin sources, low spin-charge interconversion efficiency, and insufficient spin filtering. In this context, topological insulators, thanks to their specific spin texture, provide a promising platform for the development of spintronics. Unlike the Rashba interface, the topological insulator interface does not have spin compensation induced by minority spins. Therefore, a large inverse Edelstein length or a large equivalent spin Hall angle can be achieved with topological insulators. Recent studies showed that the inverse Edelstein length of a topological insulator can be as long as 2nm[30], which corresponds to an equivalent spin Hall angle about one order of magnitude larger than for other materials (also see the summary in Table 1.1). This value is presently limited by the interface quality, and the true intrinsic potential is far from being reached. Indeed, due to spin-momentum locking, the spin transport length of topological insulators is identical to the transport length. For instance, in highly-disordered Bi_2Se_3, a canonical strong 3D topological insulator, the transport length can be as long as 200nm[31]. This suggests a much longer inverse Edelstein length can be achieved, even in a disordered system.

Beyond these studies of spin-helical Dirac fermions in 2D surface states of a 3D topological insulator, there is a specific interest to generate spin-polarized 1D states, which are dissipationless due to the spin-momentum locking. Despite the realization of dissipationless states in the QHE, the required large external magnetic field hinders its further applications. The idea of a QHE without Landau level has been proposed for long[48]. But it was not until the recent years that the quantum anomalous Hall effect (QAHE) was first realized in a diluted magnetic topological insulator (Cr-doped $Bi_xSb_{2-x}Te_3$)[4]. In the QAHE, a surface gap is opened by the intrinsic magnetism of a 3D topological insulator. This band gap remains non-trivial, and thus 1D dissipationless channels can form on the edges. Furthermore, these channels are fully

Layers	Effective spin Hall angle	Inverse Edelstein length	Experimental method	Reference
Py/Bi_2Se_3 (RT)	0.0232	N.A.	FMR spin pumping	[32]
CoFeB/Bi_2Se_3 (RT)	0.35	N.A.	ST-FMR	[33]
CoFeB/Bi_2Te_3 (RT)	1.76	N.A.	ST-FMR	[33]
CoFeB/$(BiSb)_2Te_3$ (RT)	8.33±0.65	N.A.	ST-FMR	[33]
Py/Bi_2Se_3 (RT)	2.0-3.5	N.A.	ST-FMR	[34]
Py/Cu/$(Bi_{1-x}Sb_x)_2Te_3$ (10K)	0.5-5	N.A.	ST-FMR	[35]
Py/Bi_2Se_3 (RT)	0.0093±0.0013	N.A.	FMR spin pumping	[36]
Py/Cu/Sn-doped Bi_2Te_2Se (10K)	N.A.	0.2-0.3 nm	FMR spin pumping	[37]
Fe/SnTe/CdTe/ZnTe	0.013	N.A.	FMR spin pumping	[38]
Py/$(Bi_{0.22}Sb_{0.78})_2Te_3$ (RT)	N.A.	0.075 nm	FMR spin pumping	[39]
Py/NiO/$(Bi_{0.22}Sb_{0.78})_2Te_3$ (RT)	N.A.	0.076 nm	Spin Seebeck effect	[39]
$Co_{40}Fe_{40}B_{20}$/Ag/Bi_2Se_3 (RT)	0.5	3.1 nm	ST-FMR	[40]
$Co_{40}Fe_{40}B_{20}$/Bi_2Se_3 (RT)	<0.15	N.A.	ST-FMR	[40]
$Co_{40}Fe_{40}B_{20}$/Bi_2Se_3 (50K-300K)	0.047-0.42	N.A.	ST-FMR	[41]
$Y_3Fe_5O_{12}$/Bi_2Se_3 (RT)	N.A.	0.0011-0.035 nm	FMR spin pumping	[42]
$Y_3Fe_5O_{12}$/Bi_2Se_3(6QL)/$(BiSb)_2Te_3$(6QL) (RT)	N.A.	0.037±0.004 nm	FMR spin pumping	[42]
$Y_3Fe_5O_{12}$/Bi_2Se_3(6QL)/$Cr_{0.2}(BiSb)_{1.8}Te_3$(6QL) (RT)	N.A.	0.034±0.004 nm	FMR spin pumping	[42]
CoTb/Bi_2Se_3 (RT)	0.16±0.02	N.A.	Planar Hall	[43]
NiFe/$Hd_{0.7}Cd_{0.3}Te$/HgTe (15K)	N.A.	2.0±0.5 nm	FMR spin pumping	[44]
$Co_{40}Fe_{40}B_{20}$/Bi_2Se_3 (RT)	0.3-1.75	0.38-0.82 nm	ST-FMR	[45]
Py/Bi_2Se_3 (RT)	1.71	N.A.	Planar Hall	[45]
Bi_2Se_3 (RT)	0.0085	N.A.	Scanning photovoltage microscope	[46]
$BiSbTeSe_2$ (RT)	0.0616	N.A.	Scanning photovoltage microscope	[46]
MgO/$Co_{20}Fe_{60}B_{20}$/Bi_xSe_{1-x}(4-40nm) (RT)	0.45±0.01 to 18.62±0.13	N.A.	Planar Hall	[47]
MgO/$Co_{20}Fe_{60}B_{20}$/Bi_xSe_{1-x}(4-16nm) (RT)	1.56±0.01 to 8.67±1.08	N.A.	ST-FMR	[47]

Table 1.1: Summary of recent studies that reveal effective spin Hall angle or inverse Edelstein length of topological materials.

spin polarized and protected from backscattering, and therefore are of great interest for spintronic applications. Chiral Majorana modes were found to exist in a quantum anomalous Hall insulator-superconductor structure, which opens new possibilities for using topological materials for quantum computing[1]. It is unfortunate, however, that the QAHE was only observable at very low temperature ($T < 1$K), possibly due to the a lack of strong magnetic anisotropy, a reduced magnetization and inhomogeneous distribution of magnetic dopants.

Recently, an intrinsic antiferromagnetic topological insulator $MnBi_2Te_4$ was proposed[11]. Its chemical stoichiometric composition allows a more homogeneous distribution of the magnetic element Mn, a larger magnetization and additional parity symmetry related to its thickness-dependent properties. It is a van der Waals material with Te-Bi-Te-Mn-Te-Bi-Te septuple units. The layers have intralayer ferromagnetic coupling and interlayer antiferromagnetic coupling. The bulk $MnBi_2Te_4$ is an antiferromagnet with perpendicular magnetic anisotropy. Ab initio calculations and angle resolved photoemission spectroscopy (ARPES) results agree on a relatively large band gap ($\geq$80meV[9, 49]) of the surface state. Furthermore, the Néel temperature is around 25K, which is comparatively larger than the T_c of a diluted magnetic topological insulator[4]. It is very promising that a high-temperature QAHE can be achieved on $MnBi_2Te_4$. Other derivatives in the $[MnBi_2Te_4][Bi_2Te_3]_n$ family, such as $MnBi_4Te_7$ and $MnBi_6Te_{10}$, are also proposed to be magnetic topological insulators[50]. These findings have broadened the study of the QAHE, which was limited to diluted magnetic materials but now can be also investigated in intrinsic magnetic topological insulators, which which give in addition many perspectives to control novel topological states by the magnetic order, also possibly in heterostructures.

Besides the topological properties of $[MnBi_2Te_4][Bi_2Te_3]_n$ materials, their magnetic properties are also intriguing. First of all, non-magnetic spacers (quintuple Bi_2Te_3 layers) can reduce the interlayer exchange coupling, which in certain cases can become smaller than the anisotropy. This is an uncommon situation for antiferromagnets in condensed matter. Secondly, thanks to the van der Waals nature of these materials, they can be thinned down to few layers or even to monolayers, where 2D magnetism can exist. With uniaxial magnetic anisotropy, the long range magnetic order can be stabilized in such 2D systems. In the recent years, a few materials were shown to have long range magnetic order on the 2D scale, including but not limited to CrI_3[51], Fe_3GeTe_2[52] and $Cr_2Ge_2Te_2$[53]. It is worth noting that $[MnBi_2Te_4][Bi_2Te_3]_n$ are one of the first discovered van der Waals antiferromagnets[9, 10, 50]. The layer dependence of magnetism, the dynamics of antiferromagnetic domains in the 2D limit, and the possibilities of skyrmion formation in such systems are still undiscovered areas.

1.2 Objectives

The surface band gap of magnetic topological insulators depends on the long range magnetic order. Understanding the magnetic properties of the magnetic topological insulators is not only crucial for a better control of the QAHE (in the uniform magnetization state) but also to stabilize the axion insulator regime (in the antiferromagnetic state). Early studies considered only exchange interactions, and the observation of narrow hysteresis loops in $MnBi_4Te_7$ was wrongly attributed to a ferromagnetic interlayer exchange interaction[10]. In this work, we show that the magnetic properties of van der Waals antiferromagnets can result from competing interactions (exchange, anisotropy, Zeeman), with similarities to the case of synthetic antiferromagnets. It is worth noting that the energy scale of these interactions are small enough to allow us to investigate the full magnetic phase diagram with laboratory magnetic fields. Remarkably, the interlayer exchange coupling of $[MnBi_2Te_4][Bi_2Te_3]_n$ is strongly reduced already for the $n = 1$ case, namely for $MnBi_4Te_7$. As discussed later in this work, the properties of $MnBi_4Te_7$ are similar to those of other compounds with $n > 1$ and hence the material can be considered typical for weakly coupled antiferromagnets. A detailed study of the magnetic properties of both $MnBi_2Te_4$ and

$MnBi_4Te_7$ by means of magneto-transport measurements allows us to evidence the importance of the perpendicular magnetic anisotropy. In particular, in the weak interlayer coupling regime of $MnBi_4Te_7$, the anisotropy induces a metamagnetic state at low temperature, where ferromagnetic-like magnetization loops can be observed. This result could be important to realize the QAHE at higher operating temperatures. The experimental results are well captured by a modified Stoner-Wohlfarth model, taking both the uniaxial anisotropy K and the interlayer exchange coupling J into account.

This manuscript consists of eight chapters. Chapter 1 gives a general introduction and details the structure of this thesis. Chapter 2 reviews the magneto-transport properties of materials with a non-trivial topological band structure. Chapter 3 reviews the notion of $\mathbb{Z}_2$ 3D topological insulators and the materials identified as magnetic topological insulators. The various methods to couple the surface state electrons with magnetism and the limitations of those methods are discussed in detail. Chapter 4 gives a description of the methods used in this work. The growth of the materials, sample preparation as well as the experimental techniques used are presented. In chapter 5 and chapter 6, comparative studies between $MnBi_2Te_4$ and $MnBi_4Te_7$ are carried out. In chapter 5, it is shown that $MnBi_2Te_4$ has relatively large spin-flop transition field and large spin canting after the transition. Furthermore, the spin-flop transition is limited to small field angles. These results manifest the relatively strong interlayer exchange coupling. On the other hand, in chapter 6, it is shown that $MnBi_4Te_7$ has not only spin-flop transitions that are in contrast with those of $MnBi_2Te_4$ (smaller transition fields and larger critical spin-flop angles), but also ferromagnetic-like hysteresis loops below the blocking temperature, which reveals the different magnetic properties of $[MnBi_2Te_4][Bi_2Te_3]_n$ are caused by the different interlayer coupling strength. This finding is further verified in chapter 7 with a semi-quantitative model, which captures the magnetic properties of both materials by considering the exchange, anisotropy and Zeeman energy.

Chapter 2

Hall effects

In magneto-transport, the transverse conductivity can result from different mechanisms, all of which giving a finite transverse velocity to quasi-particles, limited by disorder in classical mechanics. The most simple one is the normal Hall effect, due to the Lorentz force on charges in an applied magnetic field, only related to the carrier density. Without a magnetic field, the spin-orbit coupling makes the scattering process on impurities spin dependent, which results in the anomalous Hall effect (AHE) in magnetic materials, and the spin Hall effect (SHE) in non-magnetic materials. The contributions to these Hall effects can be either extrinsic, due to impurities or microscopic disorder, or intrinsic to the electronic band structure. The latter contribution has a deeper origin related to a geometric phase, the Berry phase, and is associated to dissipationless transport (although its amplitude usually also depends on disorder due to momentum scattering). In quantum matter, the Hall conductivity can even be quantized, due to the non-trivial topology of the band structure. Such a topological electronic state was first realized in a 2D electron gas under an applied magnetic field (quantum Hall effect (QHE)), and then in zero field with 2D $\mathbb{Z}_2$ topological insulators (quantum spin Hall effect (QSHE)). The latter results from a band inversion, often induced by a large spin-orbit coupling. In magnetic materials, this mechanism results in pure spin-polarized dissipationless edge states (quantum anomalous Hall effect (QAHE)), of particular interest for ballistic spintronics, quantum metrology and interconnects in information technologies.

2.1 Classical Hall effects

2.1.1 Normal Hall effect

In 1879, Edwin H. Hall measured a finite transverse voltage on a current-carrying conductor in an external magnetic field. The transverse voltage was found to be proportional to the field strength. This effect is known as the Hall effect. It origins from the Lorentz force that deviates the free electrons propagating in the longitudinal direction. In equilibrium, the accumulated electrons on the sides of the conductor build up an electric field.

The Hall resistivity can be formulated as follows. In a two-dimensional system, the Ohm's law $\mathbf{E} = \rho\mathbf{J}$ can be written as

$$\begin{pmatrix} E_x \\ E_y \end{pmatrix} = \begin{pmatrix} \rho_{xx} & \rho_{xy} \\ \rho_{yx} & \rho_{yy} \end{pmatrix} \begin{pmatrix} J_x \\ J_y \end{pmatrix}.$$

Assuming the current flow is applied in the x-direction

$$J_x = nev_d, \tag{2.1}$$

where $v_d = -eE\langle\tau\rangle/m$ is the drift velocity of the charge carriers, n is the density of carriers, in equilibrium, the net charge flow in the y-direction is zero $J_y = 0$, and the electric field built up

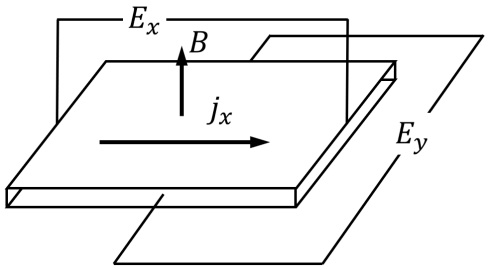

Figure 2.1: A schematic of the Hall effect.

in the y-direction balances the Lorentz force $eE_y = ev_dB$. One can obtain

$$v_dB = \rho_{yx}J_x + \rho_{yy}J_y = nev_d\rho_{yx}, \tag{2.2}$$

$$\rho_{yx} = \frac{B}{ne} = R_0B, \tag{2.3}$$

where $R_0 = 1/ne$. Note that here we also assume there is only one type of carriers. The conductivity tensor is the inverse of the resistivity tensor, where

$$\sigma_{xx} = \frac{\rho_{xx}}{\rho_{xx}^2 + \rho_{xy}^2},\ \sigma_{xy} = -\frac{\rho_{xy}}{\rho_{xx}^2 + \rho_{xy}^2}. \tag{2.4}$$

The longitudinal resistivity can be deduced from the Boltzmann transport theory[54]

$$\sigma_{xx} = \sigma_0 + \beta_0B^2 + \frac{(\gamma_0B)^2}{\sigma_0 + \beta_0B^2}, \tag{2.5}$$

$$\text{where, } \sigma_0 = \frac{ne^2\langle\tau\rangle}{m},\ \beta_0 = -\frac{ne^4\langle\tau^3\rangle}{m^3},\ \gamma_0 = -\frac{ne^3\langle\tau^2\rangle}{m^2}. \tag{2.6}$$

For $\rho_{xx} \gg \rho_{xy}$, $\sigma_{xx} \approx 1/\rho_{xx}$. Using the relation between the mobility and the conductivity

$$J_x = nev_d = ne\mu E = \sigma_{xx}E, \tag{2.7}$$

one can obtain

$$\mu = \frac{\sigma_{xx}}{ne} \approx \frac{1}{ne\rho_{xx}} = R_0/\rho_{xx}. \tag{2.8}$$

2.1.2 Anomalous Hall effect

Later, Edwin H. Hall found that the transverse voltage in a ferromagnetic conductor was much larger and it depended on the magnetization instead of the applied magnetic field. The strong Hall effect in the ferromagnetic conductor is known as the AHE. Despite the fact that the AHE was discovered only shortly after the conventional Hall effect, the mechanism of the AHE has been constantly debated and the two effects have very distinctive mechanism. In crystals, the spin-orbit coupling due to the crystalline arrays gives an intrinsic mechanism of the AHE, which must be described in the reciprocal space by taking the Berry phase into account. The insights of this mechanism were only obtained recently, which took the advantage of progresses made to understand the QHE as well as the concepts of band-structure topology[55]. The AHE can origin also from the spin-dependent scattering on short-range disorder, which is known as the extrinsic contribution. A unified theory which considers the intrinsic and extrinsic contribution to the AHE in metallic ferromagnets with dilute impurities was carried out by S. Onoda, N. Sugimoto and N. Nagaosa[56].

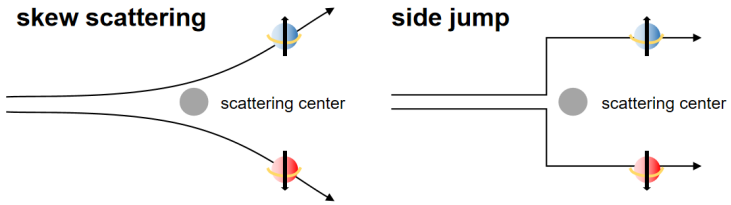

Figure 2.2: A schematic of skew scattering and side jump.

In summary, three mechanisms of the AHE were identified[57]:

1. **Intrinsic AHE** In the energy-momentum space, at the regions where the degeneracy is lifted by the spin-orbit coupling, the Berry curvature averaged over the Brillouin zone can be finite, resulting in a non-zero Berry phase. This gives a contribution to the anomalous Hall conductivity as described by eqn.2.27. This mechanism was first described by Karplus and Luttinger by considering band effects on the anomalous group velocity[58]. The relationship between the anomalous Hall resistivity and the longitudinal resistivity follows roughly the power law $\rho_{xy} \sim {\rho_{xx}}^{\beta}$, where for intrinsic contribution $\beta \sim 2$.
2. **Skew scattering** Smit argued that the main contribution of the AHE comes from extrinsic skew scattering events, for which a local potential due to disorder results in the asymmetric scattering of quasi-particles with opposite spin states[59]. Recently, it has been shown that this contribution dominates the AHE only in the high conductivity regime, or the regime where carriers are only weakly scattered by impurities[56]. For the skew scattering mechanism, the anomalous Hall resistivity follows a power law $\rho_{xy} \sim {\rho_{xx}}^{\beta}$ with $\beta \sim 1$.
3. **Side jump** On the other hand, Berger proposed another picture where the electrons are deflected by opposite electric field when they are close to the impurities[60]. Although in this picture, the power law dependence with ρ_{xx} also gives $\beta \sim 2$. Although this could make the contribution from side jump seemingly indistinguishable with the contribution from the intrinsic mechanism, the former has nevertheless been shown negligible, particularly at low temperatures[56]. And it does not necessarily refer to the picture that Berger has shown, but to all other contributions other than the intrinsic contribution, which gives $\rho_{xy} \sim {\rho_{xx}}^{2}$.

Conventionally, the Hall resistivity in a material can be written as the sum of the normal Hall resistivity and the anomalous Hall resistivity

$$\rho_{\mathrm{H}} = \rho_{\mathrm{OH}} + \rho_{\mathrm{AH}} = R_0 B + R_s \mu_0 M, \tag{2.9}$$

where the normal Hall resistivity is proportional to the applied field, and the anomalous Hall resistivity is proportional to the magnetization. The former term can be explained by the charge accumulation on the boundaries, and the latter term can be further separated into different terms according to the different contributions $R_s M = (\alpha \rho_{xx}^2 + \beta \rho_{xx}) M$, where α and β can be temperature dependent.

In colinear antiferromagnets, the time-reversal symmetry is broken, but since the combination of the time-reversal operation and the spatial translation operation has preserved symmetry, the spontaneous Hall effect was generally thought not to exist in such systems. The time-reversal symmetry can be broken in non-colinear antiferromagnets such as Mn_3Ge[61], where the spin-orbit coupling leads to the spin-dependent scattering similar to the AHE in ferromagnets. Without spin-orbit coupling, the time-reversal symmetry can be broken by chiral spin textures. In this case, the electrons which adiabatically travel through the chiral spin texture can acquire a Berry phase, which further gives rise to the transversal transport of electrons known as the topological Hall effect[62]. This effect has been observed in metallic systems such as MnGe[63] as well as

topological insulator heterostructures or magnetic topological insulators[64, 65, 66]. Specially, the effect was proposed to exist also in weakly canted antiferromagnets[67]. Recently, another mechanism that is able to break the time-reversal symmetry in colinear antiferromagnets was discovered, which origins from the anisotropic antiferromagnetic density[68]. The effect was claimed to be observed in RuO_2[69].

2.1.3 Spin Hall effect

In non-magnetic materials with a large spin-orbit coupling, it was shown that a charge current can induce a transverse pure spin current. This is known as the SHE. The SHE shares some common features with the AHE, thus also having some intrinsic and extrinsic contributions. First, the underlying reason for these Hall effects can be attributed to spin-orbit coupling and second, as a consequence, these Hall effects require no external magnetic field. Third, their Hall conductivity (for intrinsic ones) can be still described by eqn.2.27[70, 55], and the amplitude can depend on the position of the Fermi level and the disorder level[71].

The significant difference between SHE and AHE is whether the time-reversal symmetry is broken or not. A finite Hall conductivity requires breaking the time-reversal symmetry. In other words, if the time-reversal symmetry is respected, the Hall conductivity vanishes. For particles with half-spin, the time-reversal symmetry requires the same energy for particles having the opposite spin as well as the opposite momentum

$$E_{\uparrow}(\mathbf{k}) = E_{\downarrow}(-\mathbf{k}). \tag{2.10}$$

If a finite number of spin-up carriers are moving towards the transverse direction, the same number of the spin-down carriers will move in the opposite direction. The net charge difference on both sides will be zero $n_{\uparrow} + n_{\downarrow} = 0$, hence the vanishing Hall conductance. However, there can be a non-zero spin accumulation on both sides $n_{\uparrow} - n_{\downarrow} \neq 0$. The number of opposite spins with opposite momentum can nevertheless be unbalanced by magnetization. Once the time-reversal symmetry is broken by an external magnetic field or magnetization, there are imbalanced numbers of up spins and down spins that result in a finite Hall conductivity, which is the case of AHE.

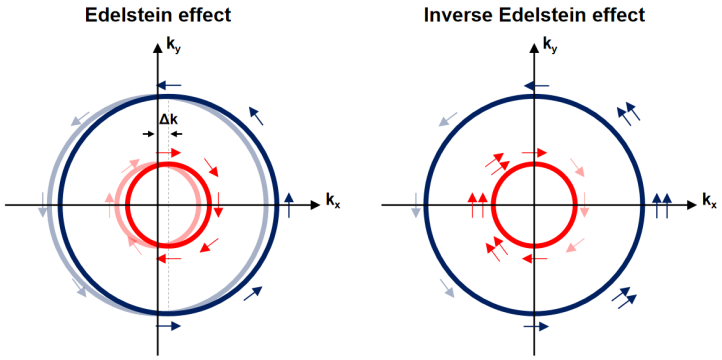

Figure 2.3: A schematic of the Edelstein and the inverse Edelstein effect.

Similar to the AHE, the SHE has different contributions, due to either the band structure (intrinsic) or to impurities (extrinsic). The spin-dependent scattering further allows a reciprocal effect where a transverse charge current can be generated by a pure spin current in the diagonal direction, which is known as the inverse spin Hall effect. A spin Hall angle can be defined to quantify the charge-current interconversion efficiency in the SHE (or the inverse SHE effect), which is the ratio of the spin Hall conductivity to the charge conductivity[71].

In 2D systems, the Edelstein effect (or the inverse spin galvanic effect), where injected unpolarized current becomes spin-polarized via the spin-orbit coupling, can exist. The principle is

shown in Fig. 2.3. For a Rashba-type system, the spin-orbit coupling lifts up the degeneracy of the energy bands. Two separated Fermi contours can be obtained by intersecting the energy surface with the Fermi surface. They have opposite spin textures, but the spin remains perpendicular to the momentum direction as required by the Rashba-type spin-orbit coupling. In the Edelstein effect, by injecting the spin-unpolarized current in the x direction, the Fermi contours are shifted to one side, which consequently induces an unbalanced spin population in the y direction. In the inverse Edelstein effect (spin galvanic effect), the injected spin-polarized current in the y direction can re-distribute the spin population on the Fermi contours, and therefore there will be a charge current in the x direction.

2.2 Hall conductivity of insulators

The concept of Berry phase reveals the topological nature of the intrinsic AHE and SHE in metals. In insulators, the Berry phase further distinguishes insulators with their band gap topology. Those with non-trivial band gaps can results in novel quantum states such as the QHE, QSHE and QAHE.

2.2.1 Berry phase

When a microscopic system evolves adiabatically along a path in the parameter space, it can pick up a geometric phase called Berry phase[72]. It describes how the quantum state evolves on this path, and hence it can be path-dependent. It is an important concept to understand the topological band structure of Bloch states in a crystal. Let's consider a Hamiltonian as a function of a series of parameters $\mathbf{R} = (R_1, R_2, R_3, ...)$, where R_i is time-dependent $R_i = R_i(t)$. These parameters can be a magnetic field, a electric field, or others. The Schrödinger equation reads

$$H(\mathbf{R})|\psi(t)\rangle = i\hbar\frac{d}{dt}|\psi(t)\rangle \tag{2.11}$$

If with varying of time, $\mathbf{R}_i(t)$ is varying slowly in the parameter space, the evolution of $\psi(t)$ with the Hamiltonian can be considered adiabatic. If instantaneous eigenstates $|n(\mathbf{R})\rangle$ of $H(\mathbf{R})$ at point $\mathbf{R}$ are introduced, such that

$$H(\mathbf{R})|n(\mathbf{R})\rangle = E_n(\mathbf{R})|n(\mathbf{R})\rangle, \tag{2.12}$$

then the evolution of $|\psi(t)\rangle$ follows

$$|\psi(t)\rangle = e^{-i\theta(t)}|n(\mathbf{R})\rangle. \tag{2.13}$$

By inserting eqn(2.12) and eqn(2.13) into eqn(2.11), one obtains

$$E_n(\mathbf{R})|n(\mathbf{R})\rangle = \hbar\left(\frac{d}{dt}\theta(t)\right)|n(\mathbf{R})\rangle + i\hbar\frac{d}{dt}|n(\mathbf{R})\rangle. \tag{2.14}$$

When multiplied by $\langle n(\mathbf{R})|$ with the assumption that $|n(\mathbf{R})\rangle$ is normalized, it yields

$$E_n(\mathbf{R}) = \hbar\left(\frac{d}{dt}\theta(t)\right) + i\hbar\langle n(\mathbf{R})|\frac{d}{dt}|n(\mathbf{R})\rangle. \tag{2.15}$$

The phase $\theta(t)$ is hence

$$\theta(t) = \frac{1}{\hbar}\int_0^t E_n(\mathbf{R}(t'))dt' - i\int_0^t \langle n(\mathbf{R}(t'))|\frac{d}{dt}|n(\mathbf{R}(t'))\rangle dt'. \tag{2.16}$$

The first term is called the dynamical phase, which is directly related to the energy of the quantum state. The second term is the geometrical phase, also known as the Berry phase γ_n

$$\gamma_n = i\int_0^t \langle n(\mathbf{R}(t'))|\frac{d}{dt}|n(\mathbf{R}(t'))\rangle dt', \tag{2.17}$$

where the vector function for the integral

$$\mathbf{A}_n(\mathbf{R}) = i\langle n(\mathbf{R})|\nabla_R|n(\mathbf{R})\rangle \tag{2.18}$$

is known as the Berry connection. The dynamical phase and the geometrical phase contribute differently to the total phase. We can rewrite the geometrical phase as implicit in time as followings

$$\begin{aligned}\theta(t) &= \frac{1}{\hbar}\int_0^t E_n(\mathbf{R}(t'))dt' - i\int_0^t \langle n(\mathbf{R}(t'))|\nabla_{\mathbf{R}}|n(\mathbf{R}(t'))\rangle\frac{d\mathbf{R}}{dt}dt' \\ &= \frac{1}{\hbar}\int_0^t E_n(\mathbf{R}(t'))dt' - i\int_{\mathcal{C}}\langle n(\mathbf{R})|\nabla_{\mathbf{R}}|n(\mathbf{R})\rangle d\mathbf{R}.\end{aligned} \tag{2.19}$$

Here the geometrical phase is determined by the position in the parameter Hilbert space, while the dynamical phase depends on the time evolution of the states' energy. So for the movement in the parameter space, we only consider the geometrical phase (Berry phase). We should notice that the Berry connection $\mathbf{A}_n(\mathbf{R})$ is not gauge invariant. Under a gauge transformation

$$|n(\mathbf{R})\rangle \to e^{i\zeta(\mathbf{R})}|n(\mathbf{R})\rangle \tag{2.20}$$

the Berry connection transforms in the following way

$$\mathbf{A}_n(\mathbf{R}) \to \mathbf{A}_n(\mathbf{R}) - \frac{\partial}{\partial\mathbf{R}}\zeta(\mathbf{R}). \tag{2.21}$$

If we consider a cyclic path, assuming that it takes a period of time T to complete the cycle, the change of Berry phase due to the gauge difference is

$$-\oint \frac{\partial}{\partial\mathbf{R}}\zeta(\mathbf{R})d\mathbf{R} = \zeta(\mathbf{R}(T)) - \zeta(\mathbf{R}(0)). \tag{2.22}$$

When the path is completed at time $t = T$, the final states should be identical to the initial states, so we have

$$|n(\mathbf{R}(T))\rangle = |n(\mathbf{R}(0))\rangle. \tag{2.23}$$

Nevertheless, under the gauge transformation this property should not be changed

$$e^{i\zeta(\mathbf{R}(T))}|n(\mathbf{R}(T))\rangle = e^{i\zeta(\mathbf{R}(0))}|n(\mathbf{R}(0))\rangle. \tag{2.24}$$

Combining the two equations above, one can find that if any gauge transformation should maintain the states in a cyclic path, it should satisfy

$$\zeta(\mathbf{R}(T)) - \zeta(\mathbf{R}(0)) = 2\pi n, \tag{2.25}$$

with n being an integer number. This means that the change of Berry phase under cyclic paths must be integer multiples of 2π. In the next section, it is shown that the Chern number itself must be an integer, because of the fact that a gauge-invariant Berry phase must be integer multiples of 2π. This leads to the quantized Hall effect.

A non-zero Berry phase comes from the fact that the final state $|\psi(t)\rangle$ is not identical to the initial state $|\psi(0)\rangle$. One mathematical analog to the Berry phase is the Hannay angle, which is a good example to understand the holonomy or the concept of Berry phase. Consider a vector moved tangential over a sphere. By doing so, the vector does not precess about the normal vector. After a cyclic movement on the sphere, this vector is no longer pointing in the same direction. Instead, there could be a non-zero angle (which is the solid angle corresponding to the surface enclosed by the path) between the final vector and the initial vector (Fig. 2.4).

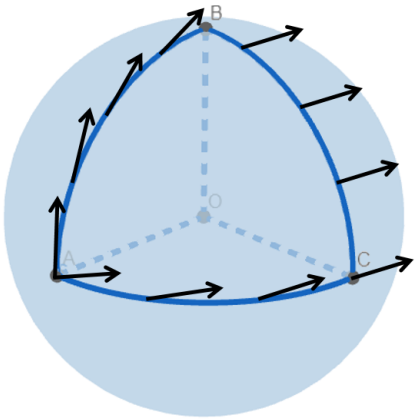

Figure 2.4: A vector doing parallel transport on a sphere through the path $A \to B \to C \to A$.. Notice that the vector does not return to its initial direction when it completes the cyclic path.

2.2.2 Chern number

By applying the Stokes theorem the γ_n can be rewritten as the integral over the surface $\mathbf{S}$ enclosed by the path $\mathcal{C}$

$$\begin{aligned}\gamma_n &=' -i\int_{\mathcal{C}}\langle n(\mathbf{R})|\nabla_{\mathbf{R}}|n(\mathbf{R})\rangle d\mathbf{R} = -i\int \nabla\times\langle n(\mathbf{R})|\nabla_{\mathbf{R}}|n(\mathbf{R})\rangle\cdot d\mathbf{S}\\ &= -i\int\langle\nabla n(\mathbf{R})|\times|\nabla n(\mathbf{R})\rangle\cdot d\mathbf{S} = -i\int \mathbf{F}_n\cdot d\mathbf{S},\end{aligned} \tag{2.26}$$

where $\mathbf{F}_n = \nabla\times\mathbf{A}_n(\mathbf{R})$ is known as the Berry curvature or the Berry field. In 1957, Ryogo Kubo proposed the linear response theory to describe the evolution of a physical variable under a time-dependent Hamiltonian. As an example Kubo used his theory to the calculation of the Hall conductivity[73]. Later it was realized that the Kubo formula, that is the Hall conductivity for a single filled band, corresponds to the integral of the Berry curvature over the Brillouin zone[74], which reads as

$$\sigma_{xy} = \frac{e^2}{h}\frac{1}{2\pi}\int_{BZ} F_{xy}(k)d_{kx}d_{ky}. \tag{2.27}$$

For two-dimensional insulators at $T = 0$, this value is quantized $\sigma_{xy} = Ce^2/h$, where C is the Chern number. For, as mentioned, in a cyclic path the change of the Berry phase should be an integer. The Hall conductivity will therefore be quantized. In fact, the Chern number is a measure of the topological obstruction[74]. Assume that the Berry curvature is well-defined in the Brillouin zone. According to the Stokes theorem, the Hall conductivity is the integral of the Berry connection on the boundary. Because of the periodic lattices, the Brillouin zone has no boundary, so it gives $\sigma_{xy} = 0$. A non-zero Chern number arises when the periodic boundary condition fails or there are singularities of Berry curvature (band crossing) in the Brillouin zone. In this case, the Stokes theorem does not apply. In the next section, it will be shown that the two-dimensional electron gas under external magnetic field, because of the formation of Landau levels and band bending at the edge, becomes a quantum Hall insulator ($C \neq 0$), with gapped bulk states and conductive edge channels, and each filled Landau level gives a quantized Hall conductivity of e^2/h.

2.3 Topological effects

2.3.1 Quantum Hall effect

Let's consider a massive quasiparticle in a two dimensional electron gas (2DEG) under a perpendicular magnetic field $\mathbf{B} = B\vec{e}_z$. The Hamiltonian reads as

$$H = \frac{1}{2m^*}(\mathbf{p} + e\mathbf{A})^2. \tag{2.28}$$

The vector potential $\mathbf{A}$ is nevertheless gauge dependent. We can choose a so-called Landau gauge $\mathbf{A} = (0, xB, 0)$ for the convenience of our calculation. By choosing such gauge, the eigenfunctions in y direction are just plane waves. We can decompose the overall wave function as $\psi_{nk}(x, y) = e^{ik_y y}\varphi_{nk}(x)$, and the Schrödinger equation becomes

$$\frac{1}{2m^*}\left[-\hbar^2\frac{\partial^2}{\partial x^2} + \left(-i\hbar\frac{\partial}{\partial y} + exB\right)^2\right]e^{ik_y y}\varphi_{nk}(x) = Ee^{ik_y y}\varphi_{nk}(x). \tag{2.29}$$

If we let

$$\omega_c = \frac{eB}{m^*},\ x_0 = \frac{\hbar k_y}{eB}, \tag{2.30}$$

then eqn(2.29) becomes the Schrödinger equation for one-dimensional harmonic oscillator

$$\left[-\frac{\hbar}{2m^*}\frac{\partial^2}{\partial x^2} + \frac{1}{2}m^*\omega_c^2(x - x_0)^2\right]\varphi_{nk}(x) = E\varphi_{nk}(x). \tag{2.31}$$

The solution of the eigenvalue problem is

$$E_n = (n + \frac{1}{2})\hbar\omega_c,\ n = 0,\ 1,\ 2,\ ..., \tag{2.32}$$

$$\varphi_{nk} = N_n H_n[a(x - x_0)]\exp\left(-\frac{1}{2}a^2(x - x_0)^2\right), \tag{2.33}$$

where

$$N_n = [a/2^n\sqrt{\pi}n!]^{1/2},\ a = \sqrt{m^*\omega_c/\hbar}, \tag{2.34}$$

and $H_n(x)$ are the n-th order Hermite polynomials.

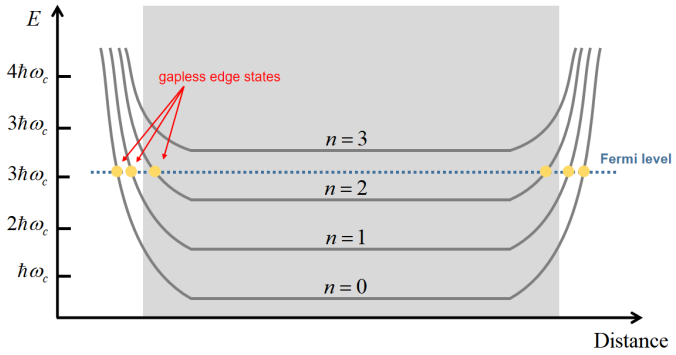

Figure 2.5: Formation of Landau levels when 2DEG is under perpendicular magnetic field.

The consequence is that discrete energy levels are formed, with the spacing between the energy levels increases as increasing magnetic field. However, this is only the case for the bulk. At the edges of the system, the additional edge potential can bend the energy bands. As a result, an energy profile as shown in Fig. 2.5 arises. Although the Landau levels are spaced and give a bulk

band gap, suppressing the conductivity from the bulk, there are however Landau levels crossing the Fermi level due to the band bending at the edges, which give gapless edge states. Each edge channel gives a conductivity of Ce^2/h ($C = 1$ here), and the total conductivity of the edge channels is just the sum of conductivity of all occupied Landau levels

$$\sigma_{xy} = \frac{e^2}{h} n. \tag{2.35}$$

As the external magnetic field increases, the spacing of Landau levels increase and there will be fewer Landau levels occupied. This results in discrete steps of Hall conductivity, with Hall plateaus at the value of ne^2/h, which is known as the QHE. Additionally, since the spacing of energy levels under high magnetic field is relatively large ($\hbar\omega_c \gg k_B T$), there is little chance that the carriers can be scattered into their neighboring states. Therefore, the edge channels are protected against weak disorders and the impedance of the transport along these channels is low.

The QHE was experimentally discovered in low-density Si metal-oxide-semiconductor field-effect transistor (MOSFET) by Klaus von Klitzing at the High Magnetic Field Laboratory in Grenoble, France[21], for which he was awarded the Nobel prize in 1985. Later, the quantized Hall effect was found more prominent in delta-doped AlGaAs heterostructures for the reason that its smaller effective mass m^* leads to a larger splitting of Landau levels, and also the high electron mobility fulfills the onset condition of quantization $\mu B > 1$ already at low magnetic fields[22]. The experimental result is shown in Fig.2.6, which clearly shows the quantized Hall resistance and vanishing longitudinal resistance.

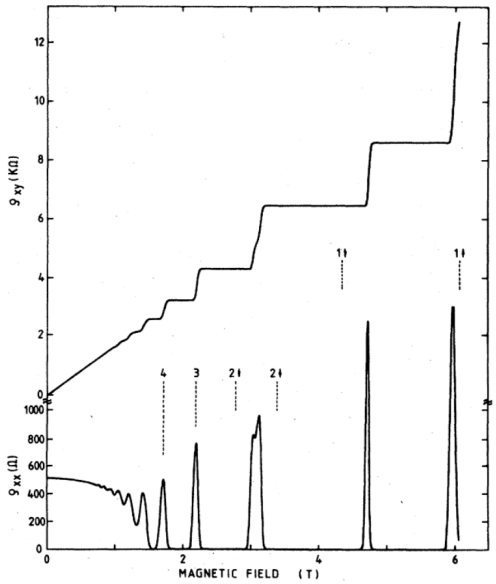

Figure 2.6: Experimental observation of QHE of GaAs-$Al_xGa_{1-x}As$ heterostructures. The Hall resistance increases with discrete steps and the longitudinal resistance vanishes at large magnetic field.[22]

2.3.2 Quantum spin Hall effect, $\mathbb{Z}_2$ topological insulator

As mentioned in the last section, the time-reversal symmetry is preserved in QSHE, the Hall conductivity vanishes and the Chern number $C = 0$. Yet, the Berry phase picked up by each spin is not necessarily zero. One can consider opposite spins picking up the same Berry phase and hence resulting in the same spin-dependent Chern number, however, with opposite signs[75]. Importantly, it was discovered that the QSHE is described by other invariants, and therefore

indeed realizes a novel topological phase in zero field, also with dissipationless edge states but different from the QHE. In real materials, it is not straightforward to evidence the QSHE. A true 2D material like graphene has a small intrinsic spin-orbit coupling, while quasi-2D materials can have coexisting interface and volume quasi-particles. As for realizing the QSHE, the problem now falls on how to eliminate the bulk conductivity without creating Landau levels in a magnetic field.

The solution was found by considering small-gap semiconductors, such as HgCdTe heterostructures[76]. For a conventional (larger gap) semiconductor, GaAs for example, the s-type Γ_6-band is located above the p-type Γ_8-band. In an AlGaAs/GaAs quantum well, the GaAs energy bands join the AlGaAs energy bands of the same symmetry (Fig.2.7(a)). The carriers are confined between the energy barriers resulted from the offset of the Γ_6-band and the Γ_8-band. For a small-gap semiconductor, this can also be the case, as for CdTe (Fig.2.7b). However, the heavier element of Hg in HgTe leads to a strong spin-orbit splitting between the Γ_7-band and Γ_8-band. In the end, the Γ_8-band is higher than the Γ_6-band (Fig.2.7(c)). Depending on the thickness of HgTe, the band orders in the CdTe/HgTe quantum well can be either inverted or normal Γ_6-band (Fig.2.7d-f). In reality, the CdTe/HgTe heterostructure has a finite size, in other words, a boundary. For an inverted well, near the boundary of the heterostructure the reversed band order will smoothly return to a normal one. Hence, there must be closing of the band gap at the edges, which provides gapless edge states for conductance. Furthermore, in contrast to the QHE, the edge states here are protected by time-reversal symmetry. For electrons propagating in one direction, they possess only one spin direction. These edge channels are therefore fully spin-polarized channels. Due to time-reversal symmetry, such edge states come by pairs of counter-propagating modes of opposite spins: a quantum state, realized in zero field, that can be seen as equivalent to the superposition of two QHEs realized for opposite large fields.

The experimental result of realizing the QSHE in the HgTe quantum well is shown in Fig. 2.8[77]. Notice that in contrast to the QHE, the quantized resistance plateaus or conductance plateaus here are not Hall plateaus, since the Hall conductivity vanishes at $B = 0$ due to the time-reversal symmetry. The longitudinal resistance does not vanish and the quantum edge channels give a conductance of $2e^2/h$, the signature of a two-mode ballistic conductor. It is worth noting that, despite the suppression of backscattering by a non-magnetic disorder, resistance plateaus in the QSHE regime always show some deviation from the exact quantization, with variations from sample to sample. This is an important difference with quantum anomalous Hall insulators, and a severe limitation for applications in quantum metrology for instance.

Topological protection of gapless edge states

Now it is clear that the reason for the formation of gapless edge states in QSHE is that the order of energy bands is inverted in the bulk. Besides the Chern number, another number called $\mathbb{Z}_2$ topological index ν has been assigned to describe the topological class of such materials[76]. For a 2D $\mathbb{Z}_2$ topological insulator, this topological index ν can only take a value of 0 or 1, indicating that such gapless states are topologically trivial or topologically protected. For a 3D system, the $\mathbb{Z}_2$ topological insulators phase was also identified, with a more complex invariant (different surfaces).

The time-reversal symmetry requires that the states are two-fold degenerated (c.f. Chap. 2.1.3), which is known as Kramers theorem. This is true for Γ-point and $k = \pm\pi/a$. However, the degeneracy is generally lifted up by spin-orbit coupling for other k values. Two cases will therefore follow. In case that the energy bands cross the Fermi level for even-numbered times, a dislocation of the Fermi level can eliminate all the crossing points (Fig. 2.9(a)). These states are susceptible to disorders and consequently topological trivial ($\nu = 0$). In the other case, where the bands cross the Fermi level for odd-numbered times, the crossing of Fermi level is always ensured (Fig. 2.9(b)), thus leading to gapless electronic states at interfaces. These states are accordingly invulnerable to non-magnetic disorders and topologically protected by symmetries ($\nu = 1$),

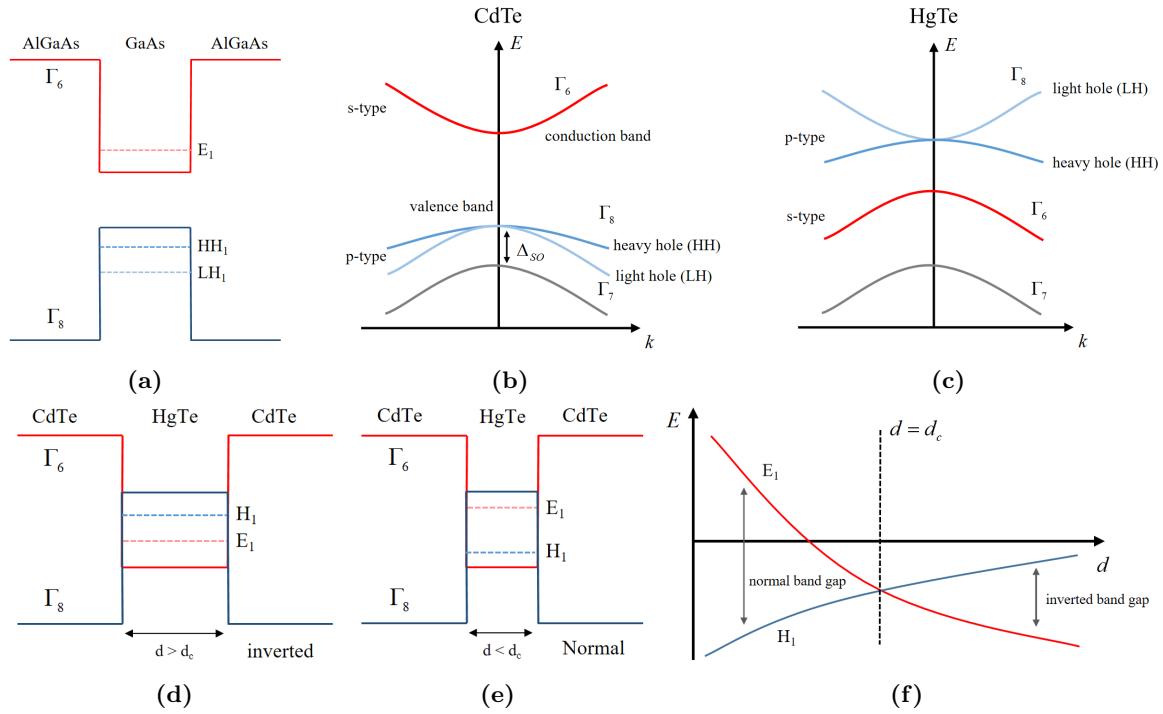

Figure 2.7: Energy profile of the quantum wells.(a) The energy profile of an AlGaAs/GaAs quantum well. (b) For CdTe, the Γ_6-band is located above the p-type Γ_8-band, which is similar to conventional semiconductor, for example, GaAs. (c) The heavy element Hg in HgTe leads to a large spin-orbit splitting between Γ_7-band and Γ_8-band, and the band order for Γ_6-band and Γ_8-band is reversed. (d) and (e) The inverted and normal energy band profile of a CdTe/HgTe quantum well, depending on the thickness of HgTe. (f) The thickness dependence of energy levels E_1 and H_1.

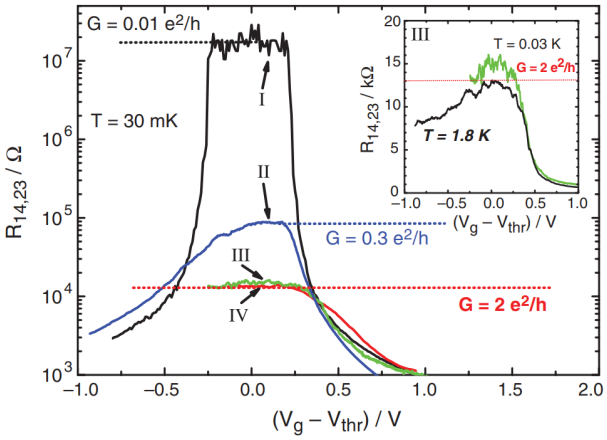

Figure 2.8: Four-probe longitudinal resistance of CdTe/HgTe quantum wells with different sizes. (I) 20.0 µm×13.3 µm×5.5 nm, (II) 20.0 µm×13.3 µm×7.3 nm, (III) 1.0 µm×1.0 µm×7.3 nm and (IV) 1.0 µm×0.5 µm×7.3 nm.[77]

unless the time-reversal symmetry is broken, which is the case in the presence of magnetic field, magnetization or magnetic disorders. In this case, the degeneracy at Γ-point or $k = \pm\pi/a$ points will be lifted up.

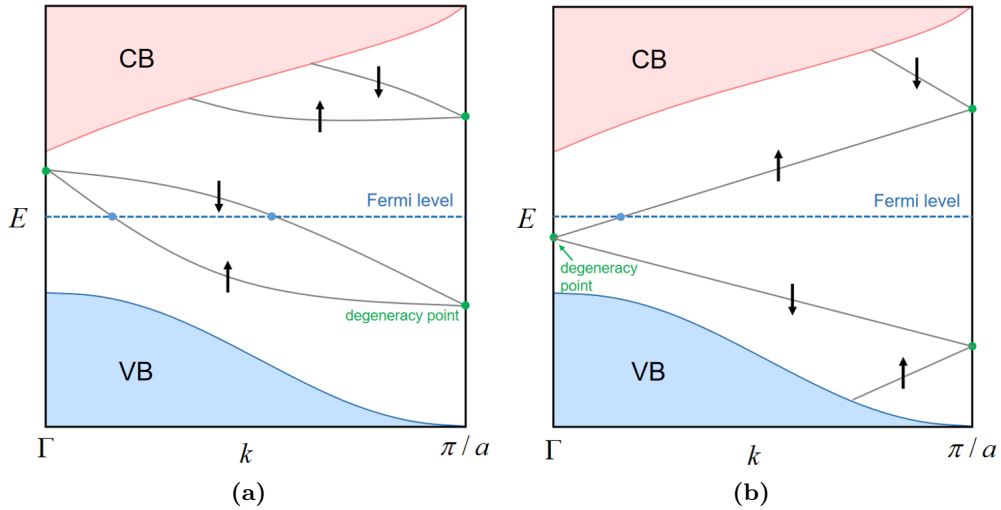

Figure 2.9: Band structures of a $\mathbb{Z}_2$ topological insulator, with a different connectivity of edge states crossing the bulk band gap. a) Topologically trivial ($\nu = 0$), and b) Topologically protected/non trivial ($\nu = 1$). In the latter case, these are gapless states, even in presence of a non-magnetic disorder (time-reversal symmetry is preserved).

2.3.3 Quantum anomalous Hall effect

Three-dimensional topological insulators have 3D bulk band gaps with non trivial topology, and therefore 2D gapless Dirac surface states. These are metallic states, robust against disorder and without any possibility to induce a strong localization of the carriers. To turn this surface states into the insulating regime, it is therefore necessary to open a gap in the surface 2D band spectrum. This can be done with proximity effects of superconductors, which do not break the time-reversal symmetry. Otherwise, it is possible to open a band gap by introducing magnetism into topological insulators. In this case, since the time-reversal symmetry is broken, the Chern number is a non-zero integer. A finite Hall conductivity will therefore be recovered $\sigma_{xy} = Ce^2/h$. This is so-called the QAHE. It is similar to the QHE, however, with fully spin-polarized channels at the edges. The prerequisites for the QAHE are also similar to those of the QHE. First, the Fermi level should lie in the band gaps or, to be more precise, the bulk band gap as well as the surface band gap. This excludes all the conductivity from the bulk and the inner area of the surfaces. Second, the large spin-orbit coupling results in a non-trivial band gap in the bulk. The band gap should be closed at the edges, so that conductive edge channels appear. Third, the time-reversal symmetry is broken, in the sense that different spins have different penalties. One of the spin channels at the edges will therefore be suppressed. In the end, it becomes the reduced version of QSHE. The difference between the QHE and the QAHE is that these edge channels are not caused by the Landau levels and the edge potential, but by the spin-orbit coupling and the magnetization.

One may easily notice that the QAHE can be controlled by the long range magnetic order. A simple intuition can be given by the following Hamiltonian

$$h(\mathbf{k}) = -\mathbf{d}_k \cdot \sigma, \tag{2.36}$$

where $\sigma = (\sigma_x, \sigma_y, \sigma_z)$ are the Pauli matrices, $\mathbf{d}_k = (k_x, k_y, M)$. By solving the stationary Schrödinger equation $h\psi = E\psi$, one can obtain the energy dispersion

$$E_\pm = \pm\sqrt{k_x^2 + k_y^2 + M^2} = \pm\sqrt{k^2 + M^2}. \tag{2.37}$$

The gapped state is only possible when there is sufficient magnetic exchange with the surface states electrons ($M \neq 0$). When $M = 0$ the gapless state with linear energy dispersion recovers.

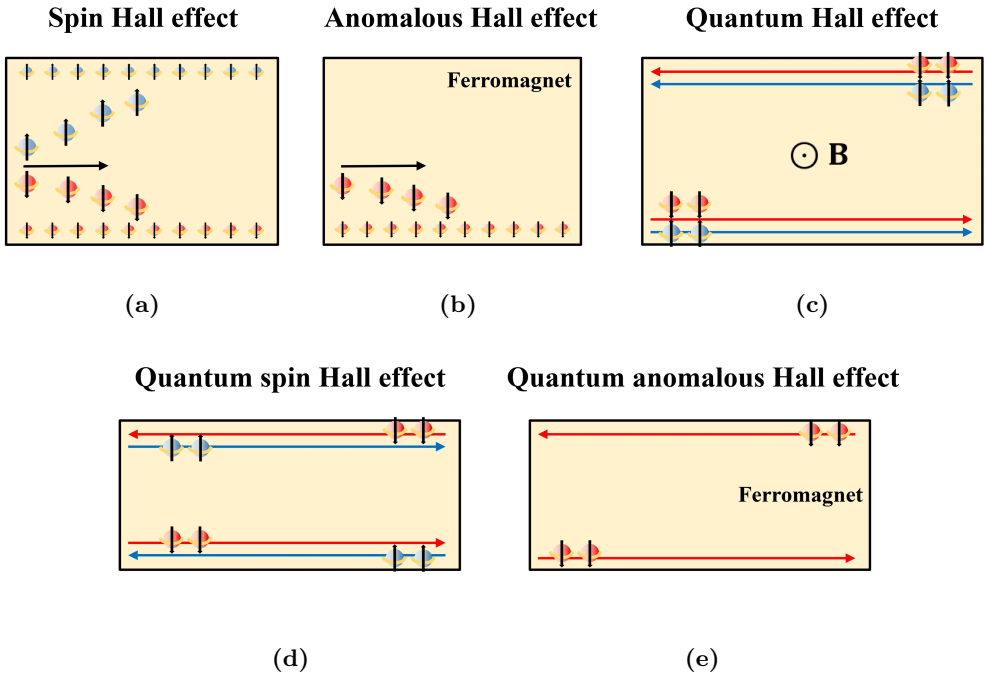

Figure 2.10: A summary of Hall effects. a) The spin Hall effect, where the carriers are scattered anisotropically depending on their spins. b) The anomalous Hall effect, where the spin-dependent scattering creates imbalance charge accumulation. (c) The quantum Hall effect. The external magnetic field generates dissipationless channels in a 2DEG system. (d) The quantum spin Hall effect. With preserved time-reversal symmetry, anti-propagating channels with opposite spins are formed on the edges, which are topologically protected. (e) The quantum anomalous Hall effect. With coupling between the magnetism and the spin-orbit coupling, dissipationless 1D channels form without magnetic field.

For applications of the QAHE, the switching field of the magnetic state of the materials should preferably be small in order to control the effect. It is possible to stack multiple layers of quantum anomalous Hall insulators for different application uses. For example, by stacking antiferromagnetically coupled layers, the quantized magnetoelectric effect can be achieved. In this case, the edge channels are turned on only when there is a finite external magnetic field to saturate the magnetization. Without applied field, due to the compensation of the neighboring layers, the conductivity at the edges vanishes. This effect will be feasible in the intrinsic antiferromagnetic topological insulators as discussed in the next chapter. High Chern number quantum anomalous Hall insulators can be also achieved in multilayer systems[78].

In summary, there are quantized versions of all the classical Hall effects, namely the QHE, the QSHE and the QAHE (Fig. 2.10). In the QHE, the electrons are unlikely to be scattered to the neighboring Landau levels, particularly for spin-polarized states in very large fields. The edge channels are ideally dissipationless. At intermediate magnetic fields, the chiral edges channels can carry both spins but they propagate only in one direction depending on whether the external field is along $+z$ or $-z$ direction. In QSHE, the carriers on the edge channels can propagate in both directions, with opposite spins for opposite momenta (helical states), with no need to apply a magnetic field. The QAHE can be considered as the reduced version of QSHE, with fully spin-polarized chiral edge channels (or as equivalent to the spin-polarized quantum Hall state). Due to the spin-momentum locking, such non-degenerate spin channels have little interaction with their environment, so that backscattering is efficiently suppressed. Therefore, it would be of high interest to implement the QAHE in low-power-consuming devices and for ballistic interconnects

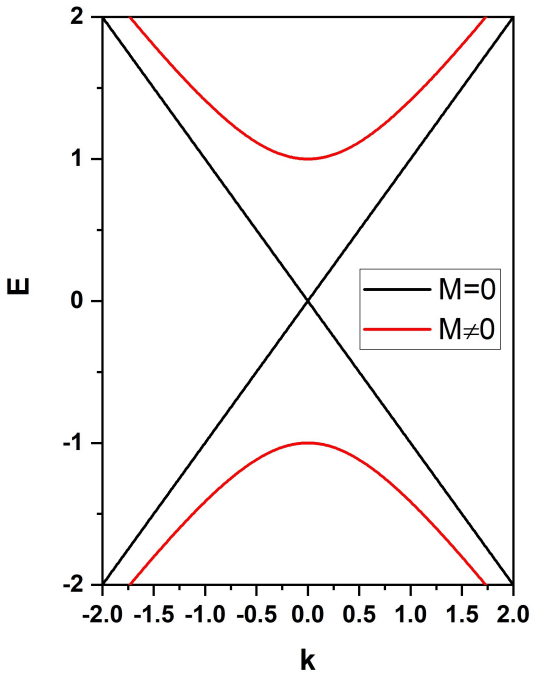

Figure 2.11: The 2D band structure of topological surface states in a 3D topological insulator, in presence of a magnetization or not. A finite component perpendicular to the surface induces a band gap.

in classical and quantum information technologies. A major remaining issue though is the limited operating temperature of present QAHE devices, which call for further developments in material science, so as to increase both the topological gap and the stability of the magnetic states.

Chapter 3

Magnetic topological insulators

The interplay of magnetism and the large spin-orbit coupling in magnetic topological insulators opens new quantum phases such as the quantum anomalous Hall effect (QAHE) and the quantized magnetoelectric effect. Experimentally, magnetic topological insulators can be realized by doping magnetic elements in 3D topological insulators. However, the inhomogeneous distribution of the local magnetic moments hinders the observation of the QAHE. Optimizing the observation requires a relative strong coupling between the local moments and the Dirac electrons, so that a larger surface band gap can be opened. Furthermore, The bulk conductivity should remain suppressed with the magnetic elements. The newly discovered $[MnBi_2Te_4][Bi_2Te_3]_n$ is promising for studies of the QAHE at higher temperature due to its homogeneous magnetic structure (A-type antiferromagnet with perpendicular magnetic anisotropy). Besides, as one of the first van der Waals antiferromagnets, $[MnBi_2Te_4][Bi_2Te_3]_n$ also provides a good platform for investigating the layer-dependent antiferromagnetism. In particular, the interplay between the bulk states and the surface states can also result in novel magnetism, which is still an open topic.

3.1 Three-dimensional topological insulators (3DTIs)

In a $\mathbb{Z}_2$ topological insulator, the non-trivial band gap leads to metallic states at its boundaries. First discovered in 2D systems, this concept was soon generalized to 3D topological insulators[79], where the non-trivial topological bulk band gap is associated to gapless surface states.. Similar to the case of 2D topological insulators, their Hamiltonian is time-reversal symmetry invariant, but it breaks the spin-rotation symmetry. This can be achieved in small-gap semiconductors for which the spin-orbit coupling is large enough to induce a band inversion and assure spin-momentum locking.

One of the straightforward ways to realize a three-dimensional topological insulator is by stacking the two-dimensional topological insulators. In this case, the gapless states are built from coupled 1D edge states, so these states exist only on the side faces. Such materials are called weak topological insulators, This was shown to be related to the connectivity of high-symmetry points (Dirac points) in the Brillouin zone, in the case of an even number of Dirac points. In this case, pairs of time-reversal invariant momenta can be connected within the bulk gap, and disorder can induce a gap in the band structure of topological surface states. For an odd number of Dirac points, the so-called strong 3D TIs, there is always a surface band connected to bulk states throughout the bulk band. Four Z_2 topological indices (ν_0, ν_1, ν_2, ν_3) have been assigned to describe the topological classes, which correspond to the parity effect for the number of Dirac points and to the orientation of surfaces supporting gapless states. It was shown that these 3D bulk topological invariants can be related to the 2D surface band structure. And indeed in the 2D Brillouin zone of surface states in a 3D topological insulator, there can be four time-reversal invariant momentum (TRIM) points Γ_{1-4} as shown in Fig. 3.1. Apart from these points, the

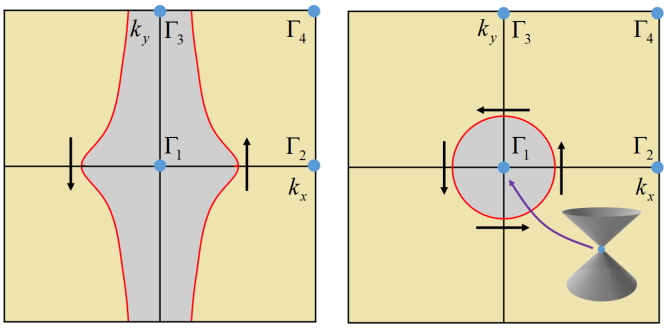

Figure 3.1: The topological index ν_0 having a value of 0 or 1 depending on the time reversal invariant point(s) enclosed by the Fermi circle. (a) The Fermi surface encloses even time reversal invariant points. The energy band between $\Gamma_{1,3}$ and $\Gamma_{2,4}$ crosses nevertheless the Fermi circle for odd numbered times and hence here is an example of a weak topological insulator ($\nu_0 = 0$). (b) The Fermi circle encloses odd time reversal invariant point(s). We can see here the energy band that connects Γ_1 and other Γ-points crosses and only crosses the Fermi level for odd times. This is the case for a strong topological insulator ($\nu_0 = 1$).

degeneracy is lifted up by spin-orbit coupling. The main invariant $\nu_0 = 0$ or $\nu_0 = 1$ indicates whether the Fermi circle encloses even or odd TRIM point(s). The latter three topological indices ν_1, ν_2 and ν_3 denote how the energy bands connect the TRIM points, similar to the two-dimensional case. The indices take values of zero or one depending on whether the energy bands cross even-numbered or odd-numbered times the Fermi surfaces. If $\nu_0 = 1$, the material is classified as a strong topological insulator. If $\nu_0 = 0$ but ν_1, ν_2 and ν_3 are not all zero, the material is classified as a weak topological insulator. If all indices are zero, the material is topologically trivial.

In contrast to 2D topological insulators which have intrinsic quantum spin Hall effect (QSHE), the strong three-dimensional topological insulators have no localized effects due to the existence of gapless states throughout the surface. Furthermore, whereas the backscattering of gapless states by a non-magnetic disorder is forbidden in a 2D TI, due to spin-momentum locking, this is not the case anymore for a 3D TI. In this case, quasiparticles can be scattered to any direction. Although direct backscattering is still forbidden, it is allowed by successive elastic scattering events, on a finite length scale given by the transport length.

The strong three dimensional topological insulator Bi_2Te_3

Since 2007, a couple of materials were predicted to be strong topological insulators, including the bismuth compounds, $Bi_{1-x}Sb_x$[80], $Bi_2(Se, Te)_3$[81], as well as Sb_2Te_3[81], and α-Sn[80], which have surface gapless states as evidenced by angle resolved photoemission spectroscopy (ARPES)[82, 83, 84]. The Bi_2Te_3 will be introduced with details here. Here, we focus on Bi_2Te_3, from which the magnetic topological insulators $[MnBi_2Te_4][Bi_2Te_3]_n$ are derived.

Bi_2Te_3 is a van der Waals layered material. Each layer (called a quintuple layer) consists of five atomic layers with covalent bonds, in the sequence of Te-Bi-Te-Bi-Te (Fig. 3.2(a)). The ARPES result shows the linear energy dispersion close to the single time-reversal invariant point (Γ-point). The energy surface close to the Γ-point is represented by the Dirac cone and it has a spin helical texture. It is of particular interest to study the physics in the vicinity of the Dirac point by applying a gate voltage to adjust the Fermi level. For example, when the Fermi level is above the Dirac point, the spins are locked to the direction that is opposite to the one when the Fermi level is located below the Dirac point. The specific spin textures of the topological surface states can serve as an intrinsic filter for different spin-momentum locking chiralities. However,

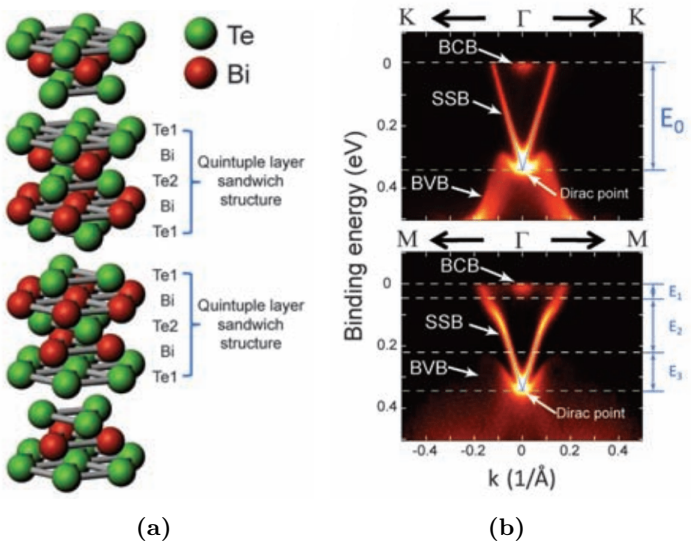

(a) **(b)**

Figure 3.2: (a) Crystal structure of Bi_2Te_3, with 2D quintuple layers separated by van der Waals bounds. b) Dispersion bands of Bi_2Te_3 measured by ARPES, along two different direction in the Brillouin zone, revealing the presence of gapless surface states.[84]

for Bi_2Te_3, the Dirac point is unfortunately below the top of the bulk valence band (Fig. 3.2(b)), and therefore low-energy surface Dirac quasiparticles coexist with bulk valence-band states.

In comparison, Bi_2Se_3 has a single Dirac point located within the bulk band gap. However, it is generally heavily n-doped due to the significant amount of Se vacancies, making it difficult to adjust the Fermi level close to the Dirac point. Still, it is possible to adjust both the bulk band gap and the relative position of the Dirac point by combining different topological insulators in the X_2Y_3 family (X=Bi, Sb; Y=Se, Te) by growing ternary or quaternary compounds[85, 86]. For instance, Sb_2Te_3 has the Dirac point in the bulk band gap, while the Fermi level is in the valence band. By tuning the Sb content in $(Bi_{1-x}Sb_x)_2Te_3$, the Dirac point can be tuned to the Fermi level. Optimized $(Bi_{1-x}Sb_x)_2Te_3$ compositions were found for molecular beam epitaxy (MBE) growth compounds with $x \approx 0.94$, where the 2D carrier density was strongly suppressed by one order of magnitude (reaching $1.4 \times 10^{-12}\text{cm}^{-2}$) and the bulk contribution can be almost excluded[87].

3.2 Realization of magnetic topological insulators

As stated, the QAHE requires the Fermi level being in the exchange band gap, which is opened by breaking the time-reversal symmetry of the surface states in three-dimensional topological insulators. Researchers have put many efforts into the experimental realization of the QAHE. Here, we review the materials and mechanisms considered so far as platforms to realize the QAHE. Among them the different mechanisms of magnetic interactions considered: the Ruderman-Kittel-Kasuya-Yosida (RKKY) interaction, the van Vleck paramagnetism, the magnetic proximity effect and the superexchange interaction. In general, the core issue of them remains on how to induce magnetic interaction in topological insulators without bulk conductivity involved. Importantly, a new symmetry arises in regularly ordered magnetic topological insulators, such as $[MnBi_2Te_4][Bi_2Te_3]_n$, which results in novel topological phases that can be tuned by modifying the magnetic textures.

3.2.1 Mn-doped $Bi_2(Se, Te)_3$

One of the ways to introduce magnetism in topological insulators is by doping with $3d$ transition metal elements, which is an idea inspired by the extensively studied diluted magnetic semiconductors. Generally speaking, in diluted magnetic systems the on-site $3d$ core spins, which do not have direct exchange coupling due to the large spacing, can nevertheless have indirect exchange interaction. In diluted magnetic metals, the itinerant electrons induce a finite coupling. The indirect exchange interaction is described by the RKKY interaction. The effective coupling coefficient of this interaction oscillates with the distance R_{12} between two magnetic impurities[88]

$$J_{12} = \frac{\sin(2k_F R_{12}) - 2k_F R_{12}\cos(2k_F R_{12})}{(R_{12})^4}. \tag{3.1}$$

Depending on the distribution of the magnetic dopants in the metal, the alloy can have ferromagnetic or spin glass characteristics. In the case of diluted magnetic semiconductors, the delocalized s-orbital electrons or the p-orbital holes have exchange interaction with the on-site $3d$ core spins of those transition metals (also referred to as the sp-d exchange), which can lead to the polarized electrons or holes due to very large Zeeman splitting in comparison with the Fermi energy. The physics of this exchange interaction can be explained by the generalized RKKY interaction[89].

Doping $Bi_2(Se, Te)_3$ with Mn may therefore introduce long-range (ferro-)magnetic order in such topological materials. In the case of carrier-mediated ferromagnetism, the magnetic order can be further controlled by tuning the carrier density. For example, the Curie temperature T_c is usually increasing with the carrier density. The experimental results showed in Fig. 3.3 manifest this property[6], but with an opposite trend: As the carrier density is suppressed, the material has a higher Curie temperature T_c. The authors argued that it is due to the elevated contribution from Dirac fermions. After suppressing the bulk carriers, the Dirac fermions are dominating the exchange interaction. However, the authors argued that the contribution from the bulk states hindered the observation of QAHE.

There could be another dominating factor which hinders the observation of QAHE. As is mentioned in the last chapter, for Bi_2Te_3, the Dirac point is below the top of the bulk valence band. A relatively larger exchange band gap is required to have the surface band gap in the bulk band gap. On the other hand, in a similar material, the Mn-doped (p-type doping) Bi_2Se_3, the ARPES results showed that it is possible to have the Fermi level in the exchange band gap of surface states[90]. Yet, the magnetic impurities contribute to both magnetic and electric doping. The surface band gap opening remains much smaller than the change in the chemical potential. For this reason, it remains very difficult to realize the conditions to investigate the QAHE in this system.

3.2.2 Cr- and V-doped $Bi_xSb_{2-x}Te_3$

The issue to have the Fermi level pinned into the exchange gap of surface states remains a challenge with Mn-based diluted 3D topological insulators. In 2010, Rui Yu *et al.*[3] proposed that in a diluted magnetic system, a sufficiently large magnetic susceptibility of electrons, which is the key to generate a spontaneous ferromagnetic order, can be provided by the enhanced Van Vleck paramagnetism in Bi_2Te_3, Bi_2Se_3 and Sb_2Te_3. The Van Vleck susceptibility is the appropriate theory to describe the susceptibility of the non-magnetic ground state with a strong spin-orbit coupling. Unlike the Langevin susceptibility that includes only the contribution from unperturbed eigenstates ($B = 0$), the Van Vleck mechanism considers also contribution from the perturbed eigenstates due to external magnetic field ($B \neq 0$), namely the mixing of the ground state with excited states due to the Zeeman interaction. While the Langevin susceptibility strongly depends on the temperature and follows the Curie's Law at $T > T_c$, the Van Vleck susceptibility is temperature independent at low temperatures. Thanks to the large spin-orbit coupling in Bi_2Se_3-family materials, they can have substantial Van Vleck susceptibility, which is

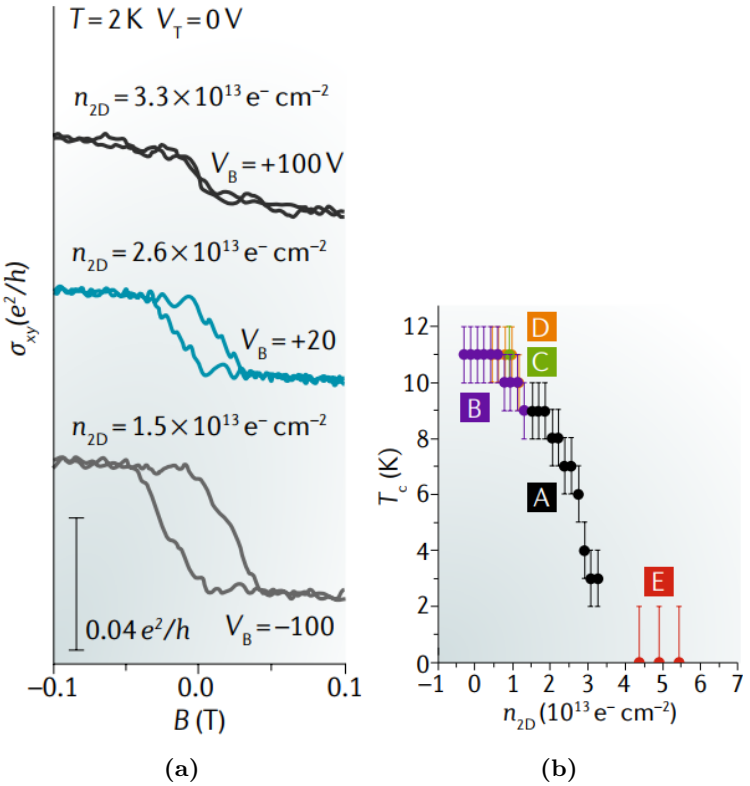

Figure 3.3: The carrier density dependent magnetic ordering in $Mn_xBi_{2-x}Se_yTe_{3-y}$ ($x = 0.04$, $y = 0.12$) single crystal. (a) The voltage controlled AHE. (b) The T_c increases with suppressed carrier density. According to the authors, this trend verifies the Dirac-fermion-mediated exchange interaction. (Adopted from [91], originally from [6].)

in general negligible in semiconductors. This susceptibility can be even enhanced by the inversed band structure. The positive aspect of van Vleck paramagnetism is that it does not rely on the carrier density as the RKKY interaction does. Rui Yu *et al.* reported that 3+ ions of V, Cr or Fe will substitute mostly the 3+ ions of Bi, leaving a low amount of free carriers introduced by the dopants. By performing first principle calculation, they demonstrated that in Cr or Fe doped Bi_2Se_3, an insulating magnetic state can be obtained.

The idea was later proven in Cr-doped and V-doped $Bi_xSb_{2-x}Te_3$ [4, 5]. Fig. 3.4(a) and (b) show the observed QAHE in Cr-doped $Bi_xSb_{2-x}Te_3$. The material itself is ferromagnetic with a relatively high Curie temperature $T_c \sim 15$K. By tuning the Fermi level in the energy gap with the applied gate voltage, the Hall resistivity has the quantized values $\pm h/e^2$, while the longitudinal resistivity vanishes. Notice that this state can be reached at zero field, indicating that the surface states are gapped by the remanent magnetization. However, this observation was only possible at very low temperature (a few tens of mK). It hinders the further study of the QAHE. The reason for that could be attributed to the inhomogeneous distribution of magnetic dopants, which leads to fluctuation of the energy landscape over the surface, including the distribution of the gap size of topological surface states. Fig. 3.4(c) shows the fact that in a Cr-doped $Bi_xSb_{2-x}Te_3$ sample, the opening of the energy gap varies from one position to another. Due to this limitation, the search for other materials appeared to be crucial in order to observe the QAHE at higher temperatures.

V-doped Sb_2Te_3 systems have certain advantages over the Cr-doped systems, which are shown by the more stable magnetic order and the less electric doping[93]. Specifically, with the same doping level, the Curie temperature and the coercivity of V-doped Sb_2Te_3 has been increased

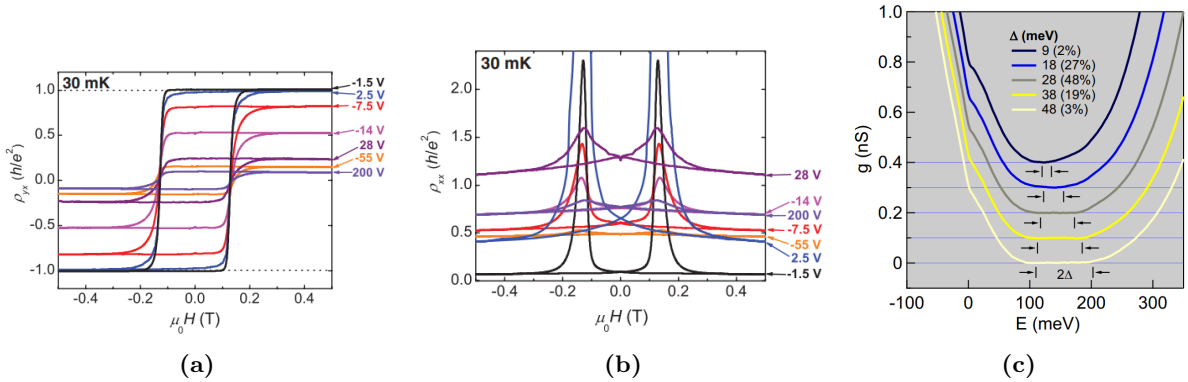

Figure 3.4: The QAHE in Cr-doped $Bi_xSb_{2-x}Te_3$. (a) The Hall resistivity shows quantized values $\pm h/e^2$. (b) The vanishing longitudinal resistivity. (from [4]) (c) The conductance at different positions of a Cr-doped $Bi_xSb_{2-x}Te_3$ sample measured by scanning tunnelling spectroscopy. The zero-conductance region was evaluated by 2Δ. Curves were shifted for clarity. (from [92])

compared with Cr-doped systems. At low temperatures, the spontaneous magnetization of V-doped Sb_2Te_3 is sufficient to drive the QAHE, whereas Cr-doped systems require an external field to initialize the magnetization. In addition, the carrier density of V-doped systems is typically lower than that of Cr-doped systems. However, one should note that the magnetic moment of V atoms is $\approx 1.5\mu_B$ per atom, while the magnetic moment of Cr atoms is $\approx 3\mu_B$ per atom[93]. The observation of the QAHE is still limited to a low temperature (<1K)[5], which demands other opportunities for realizing magnetic topological insulators.

3.2.3 TI/FMI heterostructures

It was also proposed that by proximity coupling of topological insulators with ferromagnetic insulators one can obtain an exchange gap on the surface. Unlike doping with magnetic elements, the proximity contact of ferromagnetic insulators will not introduce disorders into the crystal lattice, which could be detrimental to the mobility of carriers. Since in insulators the electrons are localized, the magnetic interaction here does not evolve with conductive electrons, and therefore the exchange interaction will be limited to the interfacial magnetic proximity effect, making it possible to achieve an insulating magnetic state on the surface. Although people have studied the AHE in such heterostructures, there is not much evidence about the opening of a desirable band gap on the surface. In fact, by tuning the Sb content in $(Bi, Sb)_2Te_3$ and the applied gate voltage, the Fermi level can be very close to the Dirac point. However, in a $(Bi, Sb)_2Te_3/Y_3Fe_5O_{12}$(YIG) heterostructure, there is no observed QAHE[94]. There is also a lack of induced magnetization in topological insulators by using the $(Bi, Sb)_2Te_3$/EuS interface[95]. Rare successes were only found when Watanabe *et al.* reported the QAHE in a (Zn, Cr)Te/$(Bi, Sb)_2Te_3$/(Zn, Cr)Te heterostructure in 2019[7]. They found that since Te would present both in the topological insulator and the ferromagnetic insulator, there would be a large chance that the topological surface states would penetrate into the ferromagnetic insulator, and would result in a large exchange gap, given the fact that ZnTe has a band gap as large as 2.28eV. Fig. 3.5 shows the observed QAHE in such heterostructure. Though it is an outstanding work among the studies of TI/FMI heterostructures, the detailed mechanism of gap opening by the proximity coupling of ferromagnetic insulators remains to be clarified. Furthermore, their observation remained limited to very low temperature.

A similar design, where the magnetization of the topological insulator Bi_2Te_3 was induced by tailoring an additional MnTe layer, resulted pronounced AHE signals[96]. This suggests the magnetic moment in MnTe can couple effectively with Bi_2Te_3 topological surface states. Indeed,

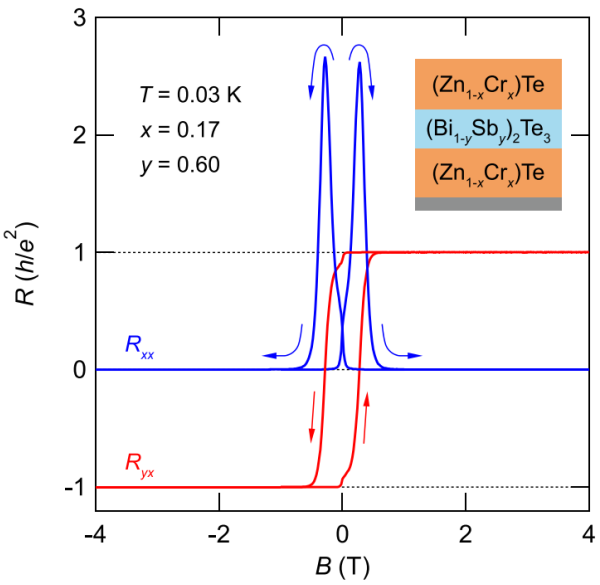

Figure 3.5: The QAHE in a $(Zn_{1-x}Cr_x)Te/(Bi_{1-y}Sb_y)_2Te_3/(Zn_{1-x}Cr_x)Te$ heterostructure.[7]

in $[MnBi_2Te_4][Bi_2Te_3]_n$ compounds, as stated in the following section, the coupling between the Mn moments and surface state electrons allow the opening of a non-trivial band gap.

3.2.4 Intrinsic magnetic topological insulators

As a matter of fact, the high temperature QAHE demands the large surface band gap, in other words, a large and homogenous magnetization with a perpendicular anisotropy, as well as a high Curie temperature of the material. While a high T_c can be found in many materials, the large surface band gap remained difficult to achieve. The limitation of Cr- and V-doped $Bi_xSb_{2-x}Te_3$ for realizing the QAHE, that is the low temperature requirement due to the shrunk gap size, calls for novel magnetic topological materials with homogenous intrinsic magnetism. Moreover, regularly ordered magnetic structure offer new possibilities to control topological quantum phases. In 2010, R. S. K. Mong, A. M. Essin and J. E. Moore proposed the antiferromagnetic topological insulators[8], which break both the time-reversal symmetry Θ and the primitive-lattice translational symmetry $T_{1/2}$ but preserve the symmetry $S = \Theta T_{1/2}$. Such materials can have gapped top and bottom surfaces. The change of Chern number occurs whenever there is an edge step, which may enable the quantized magnetoelectric effect.

The proposition of R. S. K. Mong *et al.* carves new paths to the search of magnetic topological insulators. The layer-wise properties of the proposed antiferromagnetic topological insulator can be perfectly realized by van der Waals magnets. By alternating the layers in the van der Waals heterostructures, topological properties and long-range magnetic order can be integrated in one material. Therefore, without further doping or other surface extensions, intrinsic magnetic topological insulators can be realized.

3.2.4.1 van der Waals materials and 2D magnetism

Van der Waals materials are layered materials with strong in-plane covalent bonds and relatively weak coupling between layers via the van der Waals interaction. In many cases, the layers can be separated rather easily by taping or ultrasonic exfoliation. Before the work of K. S. Novoselov and A. K. Geim *et al.*[97], it was unclear whether 2D materials could in principle exist due to their thermodynamic instability. However, they have used the simple Scotch taping method to

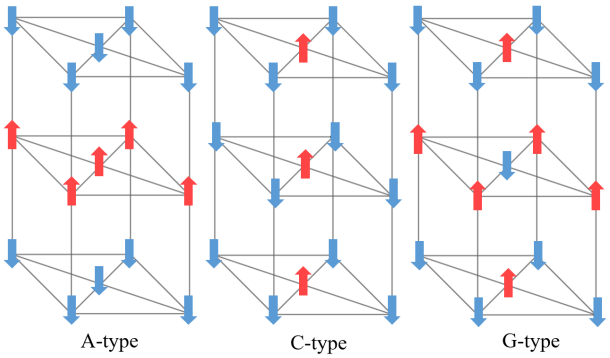

Figure 3.6: Different types of antiferromagnetic order.

yield monolayers of graphite (called graphene), MoS_2, $NbSe_2$, BN *etc.*. This paves the way to study the properties of confined electrons in 2D and also their layer dependence.

Interestingly, these 2D materials can have long range magnetic order. Precluded by the Mermin-Wagner theorem, in fact, the long range order in a two dimensional ferromagnetism system can be stabilized at a finite temperature by introducing the anisotropy[98]. Experimentally the 2D long range magnetic order has been shown in ferromagnetic CrI_3[51], Fe_3GeTe_2[99], $Cr_2Ge_2Te_6$[53], and antiferromagnetic $FePS_3$[100], $MnPS_3$[101], $CrPS_4$[102], as well as in the antiferromagnetic topological insulators $[MnBi_2Te_4][Bi_2Te_3]_n$.

Some of these materials could have magnetism independent of conduction electrons. This allows materials to have simultaneously the long-range magnetic order for time-reversal symmetry breaking and an insulating bulk state. For example, the bulk insulating ferromagnetic CrI_3 has the intralayer ferromagnetism introduced by the Cr-I-Cr superexchange coupling[103]. Here, the magnetic moments of Cr are indirectly exchanged coupled. The I atom in the middle serves as the interaction mediator. The interlayer antiferromagnetism is rather introduced by the Cr-I·I-Cr superexchange interaction[104].

Specially, the antiferromagnetic topological insulators $[MnBi_2Te_4][Bi_2Te_3]_n$ and the $CrPS_4$ has similar A-type antiferromagnetic order. Examples of antiferromagnetic order are shown in Fig. 3.6. They have the Néel vector along the c-axis, while in the ab-plane the exchange coupling is ferromagnetic. A single layer of such material has intrinsic 2D ferromagnetism. For few-layer systems, the material can have layer-dependent properties. The magnetic moments of odd-numbered layers are not compensated. They can have magnetization curves similar to those of typical ferromagnets. Whereas, for even-numbered layers, they behave as bulk crystals with typical antiferromagnetic properties. In general, the interlayer exchange coupling of van der Waals A-type antiferromagnets is weak. The spin-flop transition field is relatively low. By increasing the field along the c axis, one can modify the initial antiferromagnetic state, the canted state, and the (nearly) fully magnetized state. This was shown in bulk $CrPS_4$ crystals (Fig. 3.7). The properties of $[MnBi_2Te_4][Bi_2Te_3]_n$ will be discussed in the following chapters.

3.2.4.2 Topological properties of $[MnBi_2Te_4][Bi_2Te_3]_n$

$CrPS_4$ already was a good candidate to search for antiferromagnetic topological insulators. However, it is topologically trivial. In 2019, there were predictions of the intrinsic antiferromagnetic topological insulator $MnBi_2Te_4$[11], which belongs to the family of $[MnBi_2Te_4][Bi_2Te_3]_n$. This material combines both the non-trivial band structure and long-range magnetic order, and it was indeed identified as the first 3D antiferromagnetic topological insulator[9]. Therefore, it is a very promising material for the study of the QAHE.

$MnBi_2Te_4$ is a van der Waals layered material. Each van der Waals layer, called one septuple

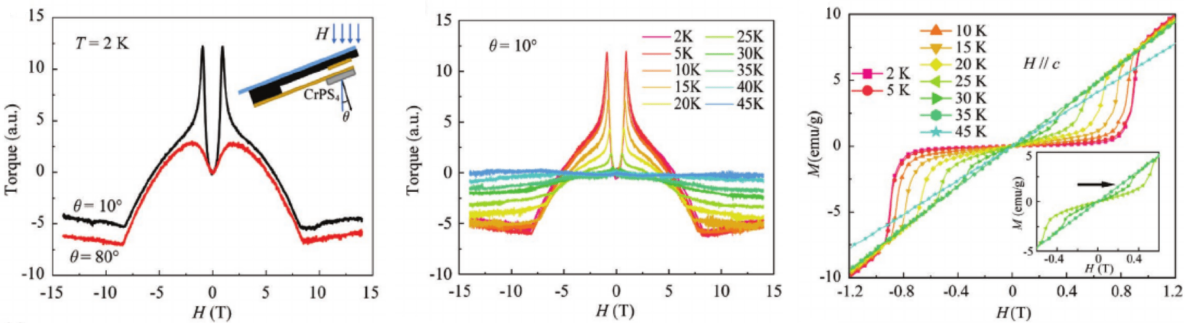

Figure 3.7: Magnetic properties of $CrPS_4$. (a) Magnetic torque of $\theta = 10°$ and $\theta = 80°$. (b) Magnetic torque at different temperature. (c) Field-dependent magnetization at different temperature.[102]

Thickness (SL)	$\Delta E_{A/F}$ (meV/(Mn pair))	Order	MAE (meV/Mn)	T_c (K)	Topology	Band gap (meV)
1	14.77	FM	0.125	12(1)	Trivial	321
2	-1.22	cAFM	0.236	24.4(1)	ZPQAH	107
3	-1.63	uAFM	0.215		QAH	66
4	-1.92	cAFM	0.210		ZPQAH	97
5	-2.00	uAFM	0.205		QAH	77
6	-2.05	cAFM			ZPQAH	87
7	-2.09	uAFM			QAH	85
(bulk)	-2.80	cAFM	0.225	25.42(1)	3D AFM TI	225

Table 3.1: Thickness dependence of $MnBi_2Te_4$ calculated by Monte Carlo simulations. $\Delta E_{A/F} = E_{AFM} - E_{FM}$ is the total energy difference of the antiferromagnetic and ferromagnetic states. cAFM and uAFM stand for the compensated and the uncompensated antiferromagnetic state. T_c is the Curie (for single layer) or the Néel temperature (for multilayers).[11]

layer, contains 7 atomic layers, ordered in a sequence of Te-Bi-Te-Mn-Te-Bi-Te (Fig. 3.8a). The van der Waals layers stack with the A-B-C sequence. The Mn atoms in the middle of the septuple layer carries the magnetic moment. In contrast with Cr- or V- doped topological insulators, ideally, $MnBi_2Te_4$ has a stoichiometric crystal structure, which allows a homogeneous magnetic structure in the material. The material can be grown by depositing alternatively Bi_2Te_3 and MnTe layers. Most Mn atoms will substitute Bi atoms with a Te octahedron crystal-field environment, providing an out-of-plane local magnetic moment of $\pm 4.607 \mu_B$[9]. The A-type antiferromagnetic order was predicted by Monte Carlo simulations. The intralayer coupling is ferromagnetic, while the interlayer coupling is antiferromagnetic, mediated by the Mn-Te·Te-Mn superexchange interaction. According to the density functional theory calculation, the material is topologically non-trivial. The top and bottom faces are gapped, while the side faces remain gapless (Fig. 3.8b and 3.8c)[49]. A surface band gap as large as 160meV was predicted.

$MnBi_2Te_4$ provides a platform to study the interplay between the magnetic properties and the topological properties. Monte Carlo calculation showed that these properties have layer dependence (Table. 3.1)[11]. Odd-numbered layers (except a single layer, which is predicted to be a trivial ferromagnetic insulator) are uncompensated antiferromagnets, in which the zero-field QAHE can be observed. On the other hand, the even-numbered layers are compensated anti-

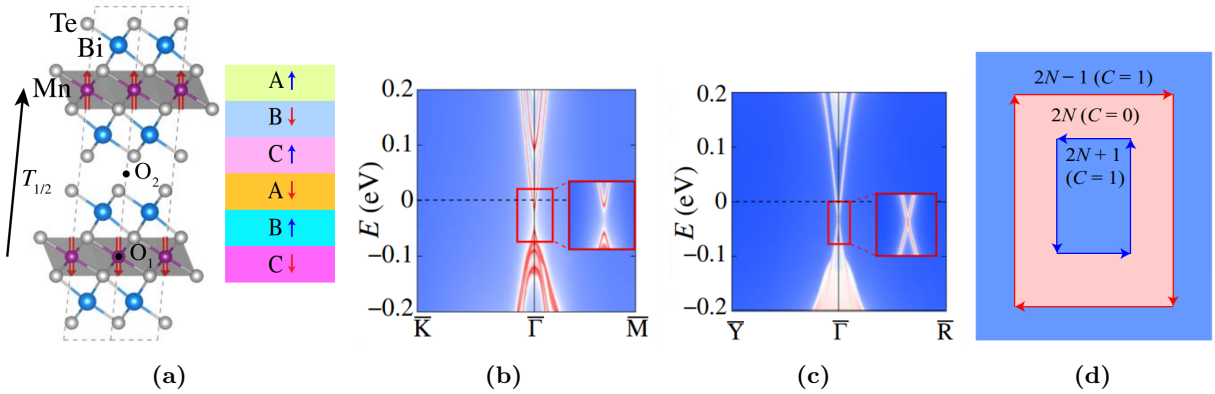

Figure 3.8: The $MnBi_2Te_4$ as an antiferromagnetic topological insulator. (a) The crystal structure of $MnBi_2Te_4$. (b) and (c) The gapped (111) face and the gapless (110) face. (d) The $MnBi_2Te_4$ shows a layer-dependent properties. For odd-numbered layers, the material is an intrinsic quantum anomalous Hall insulator, with $C = 1$. For even-numbered layers, the material is an axion insulator with quantized magnetoelectric effect ($C = 0$), or in other words, the QAHE with zero plateaus. At the edge steps, the Chern number changes.[49]

ferromagnets, in which the topological axion states can exist and the quantized magnetoelectric effect can be observed[105]. The quantized magnetoelectric effect can be also viewed as the QAHE with zero plateaus. This layer-dependent property suggests that the surfaces, in contrast with the conventional topological insulators, are not insensitive to disorders. For, there will be a change of Chern number at each edge step (Fig. 3.8d). In fact, as mentioned earlier, the time-reversal symmetry in an antiferromagnetic topological insulator is broken. Although the S symmetry $S = \Theta T_{1/2}$ gives a Z_2 topological invariant, the preservation of symmetry $S = \Theta T_{1/2}$ involves space translation symmetry, which can be vulnerable to disorders. In general, $MnBi_2Te_4$ is considered as a weak topological insulator[8].

The antiferromagnetic topological insulator phase of $MnBi_2Te_4$ was experimentally realized after the theoretical prediction[9]. It can be grown by controlled annealing of a melt 1:1 mixture of Bi_2Te_3 and α-MnTe, or with the vertical Bridgman method. The magnetic properties of samples grown by Anna Isaeva *et al.* (Technische Universität Dresden, Dresden, Germany) were investigated with the superconducting quantum interference device (SQUID) and the vibrating-sample magnetometer (VSM) (Fig. 3.9a and 3.9b). The results revealed that the bulk single crystal of $MnBi_2Te_4$ has an antiferromagnetic order with perpendicular anisotropy below the Néel temperature $T_N = 24.2(5)$K. By applying the magnetic field along the easy-anisotropy axis, A spin-flop transition was observed at 3.5T. The ARPES results confirmed the relatively large gap (about 70meV) opened at the Γ point (Fig. 3.9c, 3.9d and 3.9e). This proves that the material is very promising for the study of the QAHE as well as the quantized magnetoelectric effect at a higher temperature.

Recently (in 2020), the QAHE was evidenced in a few septuple layers of $MnBi_2Te_4$ at 1.4K (Fig. 3.10)[52]. At high magnetic field (∼10T), the sample was fully magnetized and the Hall resistance was close to the quantized value, reaching the plateau at $0.998h/e^2$. The longitudinal resistance almost vanished. However, the quantization of the Hall resistance was not perfect at zero field, with $R_{yx} \sim 0.97h/e^2$, and the longitudinal resistance had a large value (∼kΩ). Furthermore, the observation was still limited to relatively low temperature. These limitations could be due to the weak interaction between the local moments and Dirac electrons. Remarkably, the quantized magnetoelectric effect was observed in even-numbered-layered systems[106]. With such nanostructures, C. Liu *et al.* reproduced the spin-flop transition at ±3.5T. Beyond the spin-flop transition field, at 9T, they were able to observe quantized Hall plateau at $\sim 0.974h/e^2$, whereas below 3.5T, they observed a Hall plateau with $\rho_{yx} \approx 0$ ($T = 1.6$K). These findings verify

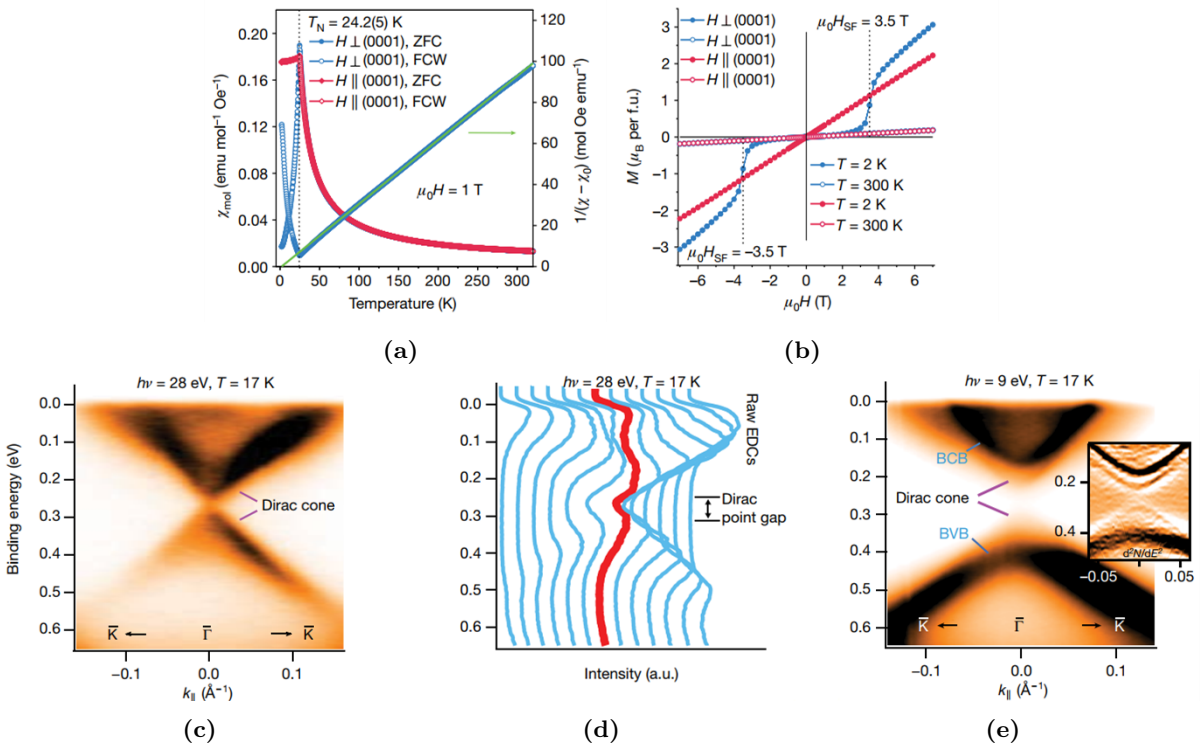

Figure 3.9: Experimental realization of $MnBi_2Te_4$. (a) The out-of-plane and in-plane magnetic susceptibility of $MnBi_2Te_4$ measured in zero-field-cooled (ZFC) and field-cooled-warming (FCW) conditions. (b) The field-dependent magnetization curve of $MnBi_2Te_4$. (c), (d) and (e) The ARPES results of $MnBi_2Te_4$.[9]

that magnetism influences topological properties in stoichiometric magnetic topological insulators. However, in order to apply these novel properties, the barriers for observation of QAHE need to be further removed.

The growth of other phases of $[MnBi_2Te_4][Bi_2Te_3]_n$ with $n > 1$ such as $MnBi_4Te_7$ and $MnBi_6Te_{10}$ is possible[107]. The crystal structures for $n > 1$ members are similar in that the magnetic septuple layers of $MnBi_2Te_4$ are separated by $n - 1$ quintuple layers of non-magnetic Bi_2Te_3 (Fig. 3.11). Due to these non-magnetic spacers, the strength of the interlayer coupling is weaker for the materials with larger n values. This allows tunable magnetism for $[MnBi_2Te_4][Bi_2Te_3]_n$ with different n. In the next chapters, we will discuss how the interlayer coupling affects their magnetic properties. Understanding the magnetism of these materials is crucial since the QAHE and the quantized magnetoelectric effect will be controlled by the magnetic structure. The stability of the magnetic structure at elevated temperature will be one of our concerns. Long-range magnetic order at higher temperature gives the possibilities of applications at high temperature. The magnetization process is another concern as a relatively low magnetic transition field allows the manipulation of these topological effects without bulky superconducting magnets.

How the magnetic layers in $n > 1$ systems are coupled is still unclear. The Mn-Te·Te-Mn superexchange interaction, which seems to be the possible mechanism of interlayer coupling in $MnBi_2Te_4$, may not play a role as well in $n > 1$ systems since the distance between the layers is large. Another possible mechanism for magnetic coupling could be the indirect exchange with conduction electrons. But this would rather suggest the magnetism depends on the density of carriers. There are however no studies studying this mechanism so far. Another related question is whether the magnetic layers are coupled ferromagnetically or antiferromagnetically. As far as the recent studies[108] and the results of this work suggest, the interlayer coupling in

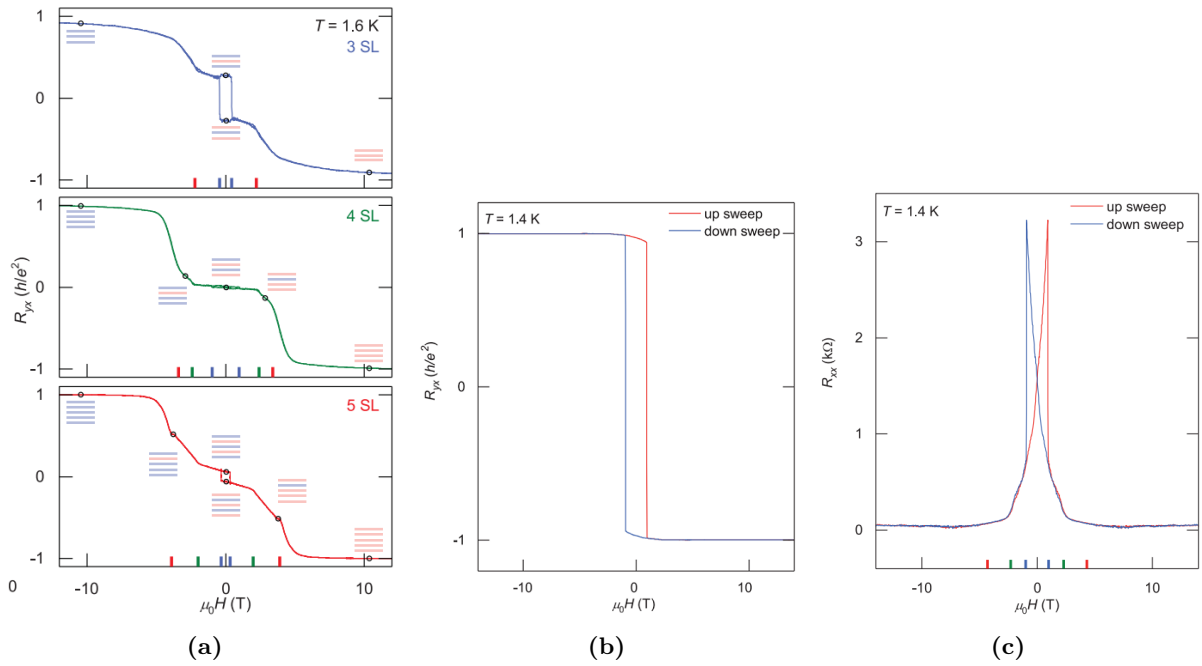

Figure 3.10: The QAHE in $MnBi_2Te_4$. (a) The Hall resistance for 3-, 4- and 5-layers of $MnBi_2Te_4$. (b) and (c) The quantized anomalous Hall resistance and the vanishing longitudinal resistance in a 5-layer sample.[52]

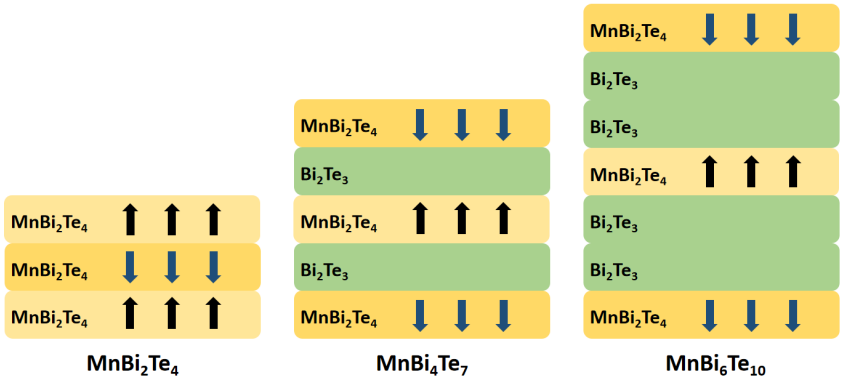

Figure 3.11: The layering of $MnBi_2Te_4$, $MnBi_4Te_7$ and $MnBi_6Te_{10}$.

$[MnBi_2Te_4][Bi_2Te_3]_n$ systems, however weak it is, is antiferromagnetic.

Gapped or gapless?

The observation of the QAHE and the quantized magnetoelectric effect confirms the gapped surface states of $MnBi_2Te_4$ in certain conditions. However, there is no consensus so far about the temperature evolution of the gap size. It was reported that gapped topological surface states were observed up to 300K with ARPES[9], which is well beyond the critical temperatures for the transition to the paramagnetic regime.. The observation was attributed to the anisotropic spin fluctuation which resulted in an instantaneous out-of-plane field acting on the surface state electrons, considering that the time scale of the ARPES photoexcitation process (10^{-15}s) is much shorter than the spin relaxation time (10^{-10}s). However, in a transport measurement, the average effect over time may result in a gapless state even when the temperature is close to T_N, since the measurement time scale can be as long as 1s. There were studies that reported the size of

the surface state energy gap of $MnBi_2Te_4$[109] or $MnBi_2Te_4/Bi_2Te_3$ heterostructures[110, 111] becomes smaller as temperature increases. This confirms the interplay between magnetism and topological properties of the material. However, there were also studies showing the surface states are persistently gapless even across the Néel transition[112, 113]. Y. Hao *et al.* proposed that the unexpected magnetic structures could be the reason for the gapless surface state, which includes: (i) Magnetic disorder due to intermixing of Mn and Bi or dislocation and reconstruction of crystal structure; (ii) Formation of in-plane A-type antiferromagnetic order instead of out-of-plane A-type antiferromagnetic order; (iii) Formation of G-type antiferromagnetic order. H. Li *et al.* on the other hand, suggested the magnetic order is coupled only weakly with the topological surface states. This can explain that although the Néel temperature is as high as ∼25K, the observation of the QAHE (or the quantized magnetoelectric effect) was still limited to $T < 2K$. In this case, further studies are required to strengthen the magnetic hybridization. Overall, the situation remains unclear and needs more studies so as to clarify this issue with the band gap size.

The situation becomes more complicated when it comes to the other members of $[MnBi_2Te_4][Bi_2Te_3]_n$ family ($n > 1$). Unlike $MnBi_2Te_4$, they can have alternative surface terminations: The termination layer can be a single layer of $MnBi_2Te_4$, a single layer of Bi_2Te_3, or multiple layers of Bi_2Te_3. It could be possible that the size of the band gap of $n > 1$ members is relatively smaller, since the hybridization between the local moments and the electrons was suggested to be weak in $MnBi_2Te_4$. Nevertheless, it was reported by J. Wu *et al.*[114] that, with ARPES a surface band gap as large as 120±10 meV can be observed (20K). The surface gap was observable up to 300K and similarly, the observation was attributed to anisotropic spin fluctuation. More detailed studies suggest that all septuple-layer-terminated $n > 1$ systems have gapless surface states[108, 115], possibly due to the fact that the surface $MnBi_2Te_4$ layer might not be well protected as those layers in the bulk. But on the other hand, the strongly gapped surface states can be protected by the termination of a single quintuple layer of Bi_2Te_3, where the gap can be as large as 100meV, similar to the gap size of $MnBi_2Te_4$. With such controversies about the gap opening on surface states, it will be important to carry out other studies, such as transport measurements, to further confirm the interplay between magnetism and topology in such systems.

3.2.5 Comparison with synthetic antiferromagnets

The development of the epitaxial growth of thin metallic layers in the 1980s allowed insightful studies of exchange coupling between magnetic layers. It was found out that changing the thickness of the non-magnetic spacer between the magnetic layers can lead to oscillatory behaviors of the exchange coupling[116]. For certain spacer thickness, the interlayer exchange coupling can be antiferromagnetic, as shown in the Fe(100)/Cr/Fe(100) stacks[117]. Such antiferromagnetically coupled metallic layers are called synthetic antiferromagnets, or sometimes referred as artificial antiferromagnets.

The exchange interaction between the magnetic layers can be used for pinning the magnetization of the layers in spintronics devices such as magnetic tunnel junctions. One of the first explanations for the oscillatory exchange interaction was given by the RKKY model, which describes the oscillating spin polarization of free carriers. They calculated the interaction of magnetic impurities in non-magnetic host materials, which is oscillating with the separation between the impurities (Eqn. 3.1). The interaction was then generalized to layers containing magnetic impurities. However, the quantum interference model is now more accepted[118]. In the quantum interference model, quantum well states are formed due to spin-dependent reflections at the NM (non-magnet)/FM (ferromagnet) interfaces. By changing the thickness of the spacer, the discrete quantum well states cross the Fermi level and give oscillatory behaviors.

The van der Waals antiferromagnets $[MnBi_2Te_4][Bi_2Te_3]_n$ are similar to the synthetic antiferromagnets to some extent. The stacked geometry is rather similar, with intralayer ferromagnetic

coupling and interlayer antiferromagnetic coupling present in both systems. Also, both systems have relatively weak interlayer exchange coupling as compared with crystal antiferromagnets. For synthetic antiferromagnets, the thickness of each layer is typically in the order of a few nanometers. This allows one to treat the spin transport through the layers with semiclassical models[119]. The situation for van der Waals antiferromagnets is somehow between the synthetic antiferromagnets and typical antiferromagnets. The thickness of each van der Waals layer (∼1nm) is larger than the interatomic distance (a few Å), but not as large as the thickness of the layers in synthetic antiferromagnets. Epitaxy growth of layers with such small thicknesses (∼1nm) is delicate since the layer may not be continuous. Van der Waals magnets, on the other hand, allow spin transport studies in this range of thickness. Even in their insulating regime, van der Waals magnets can have some significant exchange couplings, with exchange fields comparable to laboratory magnetic fields. Another important aspect that distinguishes $[MnBi_2Te_4][Bi_2Te_3]_n$ is the perpendicular magnetic anisotropy. The magnetic anisotropy for synthetic antiferromagnets is typically dominated by their shape anisotropy, in which case the shape of the sample will affect its anisotropy and a specific aspect ratio is required for strong anisotropy. On the contrary, the anisotropy of $[MnBi_2Te_4][Bi_2Te_3]_n$ is dominated by the crystalline anisotropy of the 2D ferromagnet (the septuple layer). Thin-film samples can maintain their intrinsic uniaxial perpendicular anisotropy. This allows thickness-dependent studies of magnetism in such systems without deliberate control of aspect ratio.

Chapter 4

Experimental methods

4.1 Growth of $MnBi_2Te_4$ and $MnBi_4Te_7$

The $MnBi_2Te_4$ and $MnBi_4Te_7$ crystals were grown by Anna Isaeva's group in Technische Universität Dresden[12, 10, 120]. The growth was achieved by annealing the melted mixture of stoichiometric Bi_2Te_3 and α-MnTe in a furnace. Both $MnBi_2Te_4$ and $MnBi_4Te_7$ are not thermodynamically stable at room temperature, but can be obtained by quenching the metastable product at a temperature slightly below the melting point of the material. For $MnBi_2Te_4$, the melting temperature is 600(5)°C. Optimized crystal growth of $MnBi_2Te_4$ was performed by annealing the ingot in a very narrow Ostwald-Miers region (∼3°C below 600(5)°C) for several days, followed by rapid quenching with water. In terms of thermodynamic stability of the sample, temperature-programmed powder X-ray diffraction (PXRD) experiments showed that the powder $MnBi_2Te_4$ ingot started to decompose into non-stoichiometric Bi_2Te_3 and MnTe at around 150°C. Therefore, one needs to take special caution during the nanofabrication processes in order to maintain the physical properties of the crystals. For $MnBi_4Te_7$, the melting temperature is 590(5)°C, which is only slightly higher than the solidification temperature of Bi_2Te_3 (∼585°C). A pure ingot was obtained by annealing at 590°C for 3 days, subsequent slow cooling to 585°C (just above the solidification point of Bi_2Te_3), annealing for another day, and quenching in water. The decomposition of the material starts at around 210°C according to the temperature programmed PXRD experiments. Others compounds with more non-magnetic spacers such as $MnBi_6Te_{10}$, are stable in a very narrow temperature range, and therefore they are more difficult to grow as a single phase.

The crystal structures of both crystals were refined with single-crystal X-ray diffraction (SCXRD) results, which contradicts the ideal picture where Mn and Bi positions are fully occupied. Hence, disorders of Mn/Bi antisites and cation vacancies (denoted as □) were considered. The refinement of $MnBi_2Te_4$ leads to a non-stoichiometric composition of $Mn_{1-x}\square_{x/3}Bi_{2+2x/3}Te_4$, with $x \approx 0.15$ for our samples. The structure model yields that vacancies are only allowed in Mn positions. Similarly, the refinement of $MnBi_4Te_7$ leads to a non-stoichiometric composition of $Mn_{1-x}\square_{x/3}Bi_{4+2x/3}Te_7$, with $x = 0.15 - 0.2$ for our samples. The refinement also suggests antisite defects predominantly locate in the septuple layers of $Mn_{1-x}\square_{x/3}Bi_{2+2x/3}Te_4$, while the quintuple Bi_2Te_3 layers are less affected. During the transmission electron microscope (TEM) investigation, structured diffuse scattering was not prominent. This suggests there is not significant amount of stacking faults in the material.

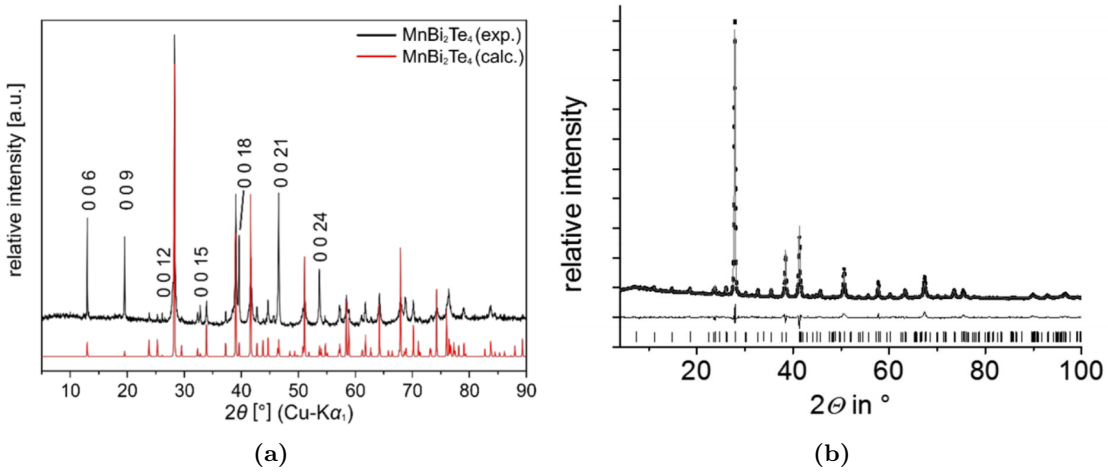

Figure 4.1: PXRD results of (a) ground crystals of $Mn_{0.85(3)}Bi_{2.10(3)}Te_4$[12] and (b) powder $Mn_{0.85}Bi_{4.10}Te_7$[120] by taking into account Rietveld refinements.

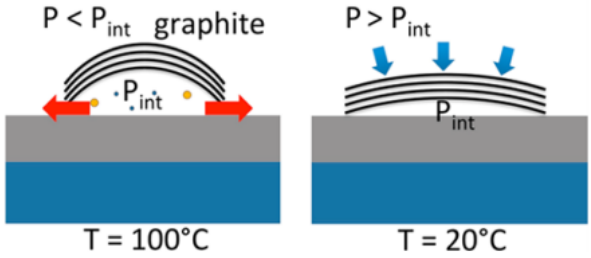

Figure 4.2: The encapsulated air between the substrate and the tape can be driven out by heating. This can improve the contact between the tape and the substrate and therefore improve the size of the flakes transferred on the substrate. The figure is taken from [121].

4.2 Mechanical exfoliation and characterization of nanostructures

To produce thin nanostructures for the measurements, we performed mechanical exfoliation on the crystal ingots by using adhesive tapes. Different techniques were developed, including a completely "cold" processing, but optimized methods requires a small heating of the substrates. Similar to the exfoliation of graphite[24], the crystals of $MnBi_2Te_4$ or $MnBi_4Te_7$ were first placed on the adhesive tape. Then the tape was folded and unfolded to generate thin flakes. The crystals were further transferred to the Si/SiO_2^{++} substrates by contacting directly the tape and the substrates. Possibly due to the air encapsulated between the tape and the substrate while contacting them, normally the flakes transferred on the substrates do not have a large area, especially for the ones with small thickness[121]. The situation can be improved by heating the substrate before removing the tape. When heating the substrate, the pressure of the encapsulated air will increase. The air will then be forced to release at the edges (Fig. 4.2). Note that the crystals are thermodynamically unstable. It decomposes around 150°C as mentioned previously. Therefore, in this work, the substrates were only heated at 90°C. Gently pressing the tape and the substrate while contacting them also helps to remove the excessive air inside. Once the substrate is back to room temperature, the tape can be removed and there will be flakes left on the substrate. During the exfoliation, the 3M Scotch tape and the Nitto blue tape were tested. The two tapes produce flakes of similar size and thickness. However, the latter one leaves fewer residues on the substrates. If there are an excessive amount of residues, the substrates can then

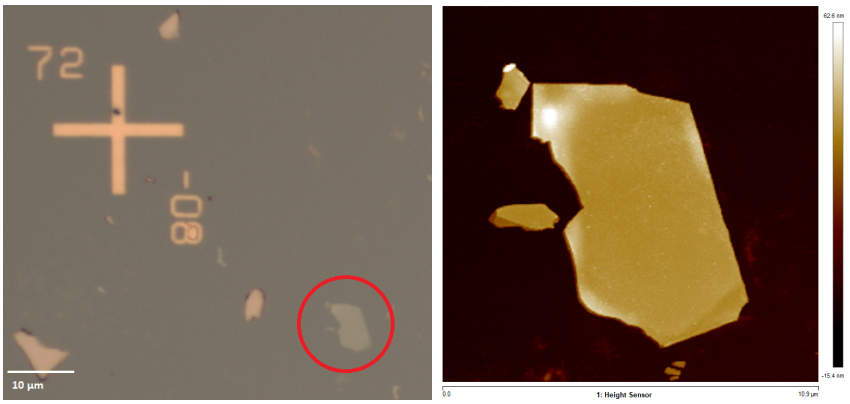

(a) (b)

Figure 4.3: Characterization of nanostructures with (a) optical microscope and (b) atomic force microscope. The thickness of the flake is around 39nm according to the atomic force microscopy result.

be partly cleaned with acetone and isopropanol. A rough search for thin nanostructures under the optical microscope is possible according to the shadow and the colour of the nanostructures (Fig. 4.3a). Thin nanostructures tend to be transparent and have less shadow area at the edges. As steps on the surface of the nanostructure will affect its topological properties, smooth surfaces will be favored. The thickness and the detailed topography of the nanostructures can be further confirmed by scanning electron microscope (SEM) or atomic force microscopy (Fig. 4.3b). From the image, one can see that the flake may not sit flat on the substrate. Instead, the edges of the flake can be curvy. However, it is possible to obtain atomic flat surfaces with the exfoliation technique. The surface roughness of the flake will be discussed later.

4.3 Nanofabrication

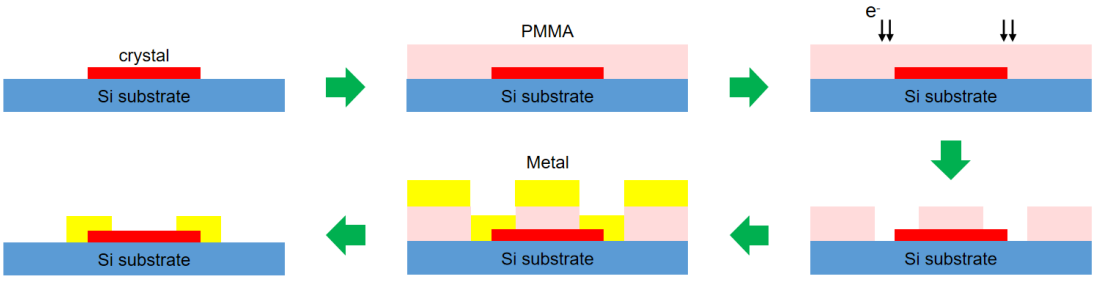

Figure 4.4: The typical procedures of the electron beam lithography process.

After a careful selection of nanostructures, the samples went through the typical electron beam lithography process (Fig. 4.4), the details of which are stated as the following:

1. 4% polymethyl methacrylate (PMMA) with molecular mass ~950000g/mol was spin-coated on the substrate. The rotating speed for the spin-coater was 4000rpm and the spin-coating time was 60s. Since the $[MnBi_2Te_4][Bi_2Te_3]_n$ decomposes at a temperature above 150°C and the physical properties of the materials can hence be affected, there was no baking after the spin-coating.
2. The exposure was done with a 100kV JEOL nano-writer. The writing dose was 1400-

1600µC/cm^2. After the exposure, the sample was developed in methyl isobutyl ketone (MIBK) solution (MIBK:isopropanol=1:3) for 90s. The development of the resist was terminated by rinsing the sample in isopropanol.

3. Before the evaporation of the metals, the sample was treated with Ar ion beam for 30s to remove the unwanted surface oxidation. The Ar ion beam used in this work has an energy of 400eV and the fluence is 24mA. The etched depth as a function of the etching time is shown in Fig. 4.5a. A rough estimation gives an etching rate of 0.18nm/s. It is possible that the etching can increase the surface roughness of the sample and therefore induces extra scattering events. In order to identify the change of surface roughness, the average roughness

$$R_a = \frac{1}{S}\iint |\Delta z| dS \tag{4.1}$$

and the root-mean-squared roughness

$$R_s = \sqrt{\frac{1}{S}\iint (\Delta z)^2 dS} \tag{4.2}$$

can be measured with atomic force microscopy. For the flake shown in Fig. 4.3, the surface roughness measured before and after the Ar ion beam treatment is shown in Table. 4.1. The result suggests the surface roughness does not increase with Ar ion beam treatment in this specific condition. To further verify the change of the density of surface features, the power spectral density (PSD) is shown in Fig. 4.5b. It confirms there was no significant increase of the density of rough features after the Ar ion beam treatment. After removing the surface oxidation, 10nm Ti, 80nm Au and 10 Al are then deposited on the substrate successively. The bottom Ti layer is intended to help the adhesion of Au to the substrate. The top Al layer will protect the contacts in the further patterning processes since the ion beam etching rate for Al is much smaller than that of other materials.

Etching time (s)	Average thickness (nm)	Average roughness R_a (nm)	RMS roughness R_q (nm)
0	39	0.428	0.578
150	20	0.223	0.293

Table 4.1: The surface roughness of a $MnBi_2Te_4$ flake measured before and after the Ar ion beam treatment.

4. After the metal evaporation, the sample will be dipped in acetone for a couple of hours. The PMMA and the metals on top of it can then be removed by a gentle flow of acetone. The remaining acetone will be cleaned with isopropanol.

To pattern the nanostructures into Hall geometry, an additional electron beam lithography process is followed:

1. The negative resist MaN-2403 (Micro Resist Technology) is spin-coated on the substrate with a speed of 4000rpm and a period of 60s. The sample is then baked on a hot plate at 90°C for 60s.
2. The electron beam writing is taken on the area to be protected. After the exposure, the sample is developed in MF-26 (tetramethylammonium hydroxide (TMAH) concentration: 1.0%∼5.0%) for 45s. The remaining MF-26 will be rinsed with deionized water.
3. The sample will then be treated with Ar ion beam etching. The etching time depends on the thickness of the flake. It may take as long as it needs to define a proper Hall geometry. The etching process is shown in Fig. 4.6.

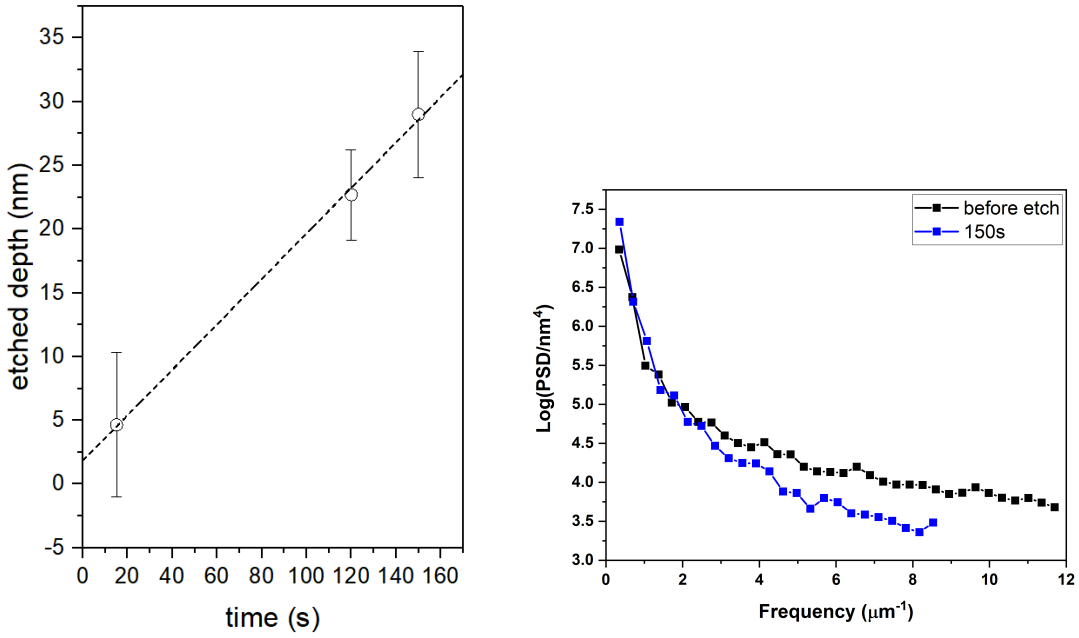

(a) (b)

Figure 4.5: (a) The etched depth of $MnBi_2Te_4$ as a function of the etching time. (b) The power spectral density (PSD) of a $MnBi_2Te_4$ flake before and after the Ar ion beam treatment.

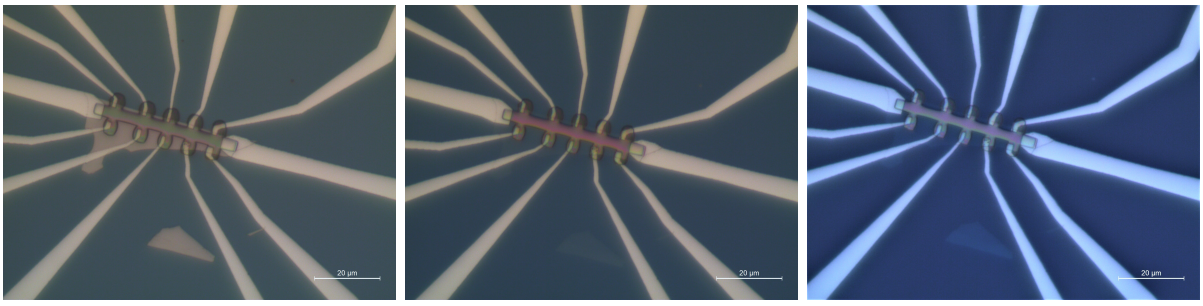

(a) (b) (c)

Figure 4.6: The etching process of a $MnBi_4Te_7$ flake during the patterning of proper Hall geometry. (a) After the patterning of metallic contacts, an additional electron beam lithography is taken on the flake to pattern the Hall geometry. After the development of the MF-26 resist, only the part that has been exposed remains. (b) The sample after 5min of Ar ion beam etching. (c) The sample after 10min of Ar ion beam etching. (Sample FMBT1)

4.4 Principle of low temperature measurement

The thermal effect at room temperature hinders the observation of many physical properties. For instance, the conductivity of good conductors is often dominated by phonon scattering at room temperature, which makes studies of other scattering events (electron-electron scattering, electron-magnon scattering, scattering by disorders *etc.*) difficult. In fact, there are quite some interesting physics phenomena which were discovered first at low temperature. The superconductivity of Hg below T_c =4.15K was discovered in 1911 by Heike Kamerlingh Onnes after his success in liquefying ^{4}He in 1908. For his work at low-temperature physics, he won the Nobel prize in 1913. In order to study the temperature dependence of physical properties of $MnBi_2Te_4$ and $MnBi_4Te_7$, the measurements performed in this work cover a wide range of temperature (0.1K-300K). Different refrigerators were used, including Compact VTI (2K-300K) and KelvinoxMT (0.1K-300K) from Oxford Instruments, and the physical properties measurement system (PPMS) (2K-300K) from Quantum Design in order to perform magneto-transport either with a rotating sample or a rotating magnetic field.

Measurements at a stable temperature above ∼2K can be achieved by PPMS and the Compact VTI. The variable temperature insert (VTI) is operated in ^{4}He liquid bath, which is shielded by a liquid N_2 bath. The ^{4}He liquid bath provides an environment at the temperature as the boiling point of ^{4}He (4.21K at a vapour pressure of 1bar). The cooling effect results from the heat transfer during the evaporation of ^{4}He. The latent heat of evaporation of ^{4}He is 2.56 kJ/L[122]. Temperature above the boiling point of ^{4}He can be simply reached by applying heat with the heater. However, in general in the design of a measurement system dedicated for 2K-300K range, the direct heat sink for the sample is not the ^{4}He bath, otherwise, there can be significant consumption of ^{4}He at high temperature. In the Compact VTI, a flow of ^{4}He will be pumped into a small tube and the cooling results from a Joule-Thomson expansion in a thermal exchanger. ^{4}He has a positive Joule-Thomson coefficient $\mu_{JT} = (\partial T/\partial P)_H$ below around 30K, and therefore the isoenthalpical expansion in the impedance leads to cooling of liquid ^{4}He. The ^{4}He flow can be controlled by opening of a the needle valve. In the tube the ^{4}He has heat exchange with the cold finger onto which the sample is mounted. Furthermore, before the He gas reaches the cold finger exchanger, it can be heated with a heating resistor, so that the stable temperature of the cold finger can be increased up to about 200K (an intrinsic limitation of the compact VTI, for which the heat loss to the ^{4}He bath in the cryostat becomes too large above 200K). The temperature control in the PPMS is achieved in a similar way.

For measurements down to 0.1K, a ^{3}He-^{4}He dilution refrigerator was used, the main part of which is a closed circuit filled with a ^{3}He and ^{4}He mixture. The main components of a typical ^{3}He-^{4}He dilution refrigerator are shown in 4.7a. It includes a continuous ^{4}He evaporator, which is also known as the 1K pot unit, for pre-cooling of the circulating ^{3}He-^{4}He mixture. Liquid ^{4}He in the reservoir enters the 1K bath through the impedance, where the liquid ^{4}He expands isoenthalpically. This process is also similar to the Joule-Thomson experiment. The filling level of liquid ^{4}He in the 1K bath reaches a certain height when the heat of the Joule-Thomson effect is balanced out by the heat exchanged with the ^{3}He-^{4}He mixture and the liquid ^{4}He bath. After exchanging heat with the incoming ^{3}He-^{4}He mixture, the evaporated ^{4}He is pumped out and recycled.

Thanks to the finite solubility of ^{3}He in ^{4}He at low temperature (<0.87K), the further cooling of ^{3}He-^{4}He mixture can be achieved by the cooling power generated when liquid ^{3}He enters from the concentrated phase to the dilute phase. The phase diagram of liquid ^{3}He–^{4}He mixtures at saturated vapour pressure is shown in 4.7b. Below 2.18K, pure liquid ^{4}He experiences a superfluid transition and becomes a frictionless liquid that can climb on the walls of the container without the impedance of friction. Liquid ^{3}He, on the other hand, because the ^{3}He nucleus is a Fermi particle, has a superfluid transition only in the millikelvin range, where it starts to follow Bose-Einstein statistics by pairing of ^{3}He. Therefore, as the concentration of ^{3}He increases, the ^{3}He–^{4}He

mixture has a lower superfluid transition temperature and no superfluid phase is possible for sufficiently large ^{3}He concentration. Below 0.87K, the mixture starts to separate into liquid ^{3}He phase and liquid ^{4}He phase. However, there is a finite solubility of ^{3}He in ^{4}He (∼6.6%). In the mixing chamber, the heavier dilute phase (∼6.6% ^{3}He) will be at the bottom and the lighter concentrated phase (∼100% ^{3}He) will be on the top. The ^{3}He leaves the mixing chamber in the dilute phase towards the still because of the osmotic pressure caused by the difference of ^{3}He concentration in the mixing chamber (∼6.6%) and in the still (∼1%). In a series of thermal exchangers, the leaving ^{3}He is also used for pre-cooling of the incoming ^{3}He–^{4}He mixture. As soon as the ^{3}He leaves the dilute phase, the ^{3}He in the concentrated phase crosses the phase boundary and generates further cooling power. The leaving ^{3}He will in the end evaporates in the still and is pumped and re-injected.

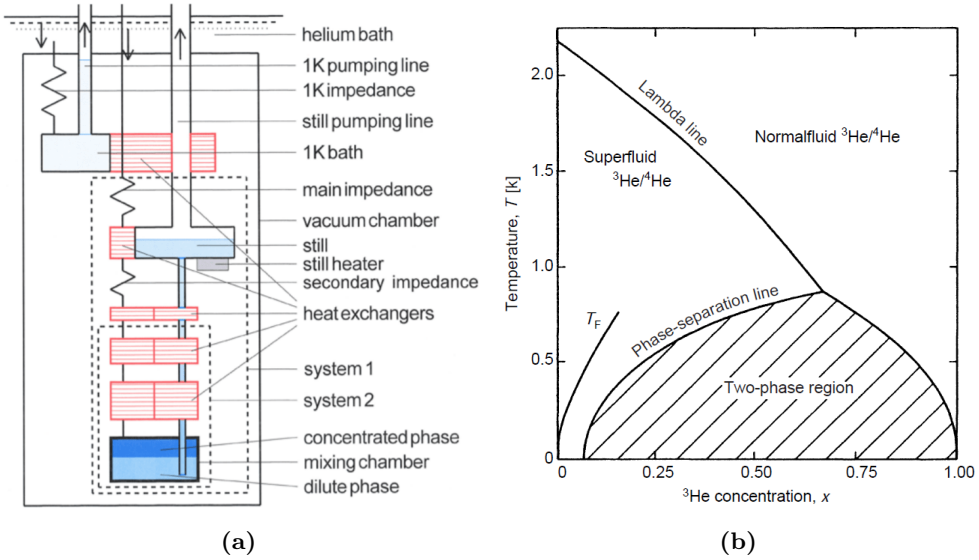

(a) **(b)**

Figure 4.7: (a) The main components of a ^{3}He-^{4}He dilution refrigerator[123]. (b) Phase diagram of liquid ^{3}He–^{4}He mixtures at saturated vapour pressure[122].

Different magneto-transport measurements setups were used:

PPMS The system is equipped with a superconducting magnet which can provide perpendicular field up to 9T. With the aid of the horizontal rotator, one can rotate the sample up to ∼180° in the out-of-plane direction. Hence, a relatively high magnetic field can be applied at an arbitrary out-of-plane angle. The Quantum Design AC transport option is using currents larger than 1μA. The signal-to-noise ratio can be improved by using an external setup for the transport measurements. The voltage source was generated by the Stanford Research Systems SR830 lock-in amplifier, with which the signals were also measured. A 485kΩ resistance was used to create a current-polarization configuration. The typical resistance of the nanostructure is less than 10kΩ, so that changes in the measured voltage are directly related to those of the sample resistance.

Compact VTI The cryostat is equipped with 2D superconducting magnets, which can provide 12T in perpendicular direction and 1T in the sample plane. The sufficient large perpendicular magnetic field provided in the system allows the studies of the magnetic systems in a fully magnetized state. The electrical measurements were performed by combining Stanford Research Systems SR830 and SR7225 (Signal Recovery) lock-in amplifiers. The polarizing resistance is 1MΩ. In order to determine the temperature close to the sample when using a perpendicular

adaptor, an additional zirconium oxy-nitride resistance thermometer, also known as the Cernox sensor, CX-1050 (Lake Shore Cryotronics) is installed near the sample. The temperature dependence of the resistance of the sensor can be fitted with Chebyshev polynomials (Appendix B).

KelvinoxMT The cryostat is equipped with 3D superconducting magnets, which can provide 6T in perpendicular direction and 2T in both other two orthogonal directions. The angular dependence study was done by by rotating the magnetic field, contrary to the PPMS, for which the sample is rotated. The electrical measurements were performed by Stanford Research Systems SR830 lock-in amplifier. The polarizing resistance is 1MΩ.

Chapter 5

The first antiferromagnetic topological insulator: $MnBi_2Te_4$

By means of mechanical exfoliation, thin $MnBi_2Te_4$ nanostructures (20nm-100nm) were obtained (Chapter 4.2). Magneto-transport measurements were carried on the exfoliated nanostructures. The results revealed a Néel transition temperature, a spin-flop transition field and a saturation field of $MnBi_2Te_4$ nanostructures that are comparable for those of bulk crystals. Further comparative studies with different samples also gave similar magnetic properties, which suggests the magnetic properties of $MnBi_2Te_4$ are robust against the change of transport properties such as the carrier density. The magnetic properties of $MnBi_2Te_4$ were further investigated with angular dependent measurements, which showed that the spin-flop transitions were limited to small field angles. The magneto-transport properties of $MnBi_2Te_4$ confirm its A-type antiferromagnetic structure.

5.1 Magneto-transport properties of $MnBi_2Te_4$ bulk crystals

Lee *et al.* reported some transport properties of $MnBi_2Te_4$ measured with bulk crystals[124]. Their results from transport measurements for $MnBi_2Te_4$ bulk crystals were in general consistent with those from SQUID or vibrating-sample magnetometer (VSM) measurements (Fig. 5.1). By applying external magnetic field along the c-axis, at 1.9K, spin-flop transitions were observed around 3.5T, where the magnetic state changed from a colinear antiferromagnetic state to the canted antiferromagnetic state, where the magnetization of two neighboring layers is at a finite angle (non-colinear). The authors further argued that the steep decrease of the magnetoresistance was due to the spin-valve effect or giant magnetoresistance effect, which has been extensively studied in thin magnetic multilayers[125]. As the field further increased after the spin-flop transition, there was a further decrease of the resistivity and a resistivity plateau was observed after 7.7T. This confirms the coherent rotation of magnetization in the canted state until saturation was reached at high fields.

The temperature dependence of the sample's resistivity at $B = 0$ showed a small peak at the Néel temperature $T_N = 25$K (Fig. 5.1g and Fig. 5.1h). The authors attributed this to the enhanced spin scattering effect. As the spin fluctuation becomes intensive when the temperature is close to the Néel temperature, there are more spin scattering events, and therefore there is an increase of resistivity. When a magnetic field larger than the spin-flop field ($B > B_{sf}$) was applied during the measurement of temperature dependence, the resistivity peak was suppressed. On the contrary, a field smaller than the spin-flop field has little influence on the Néel transition. This could be due to the relatively strong interlayer exchange coupling. In this case, only a sufficiently large field can suppress the Néel transition to a colinear antiferromagnetic state.

Despite the exciting progress Lee *et al.* have made on $MnBi_2Te_4$ bulk crystals. The magnetic

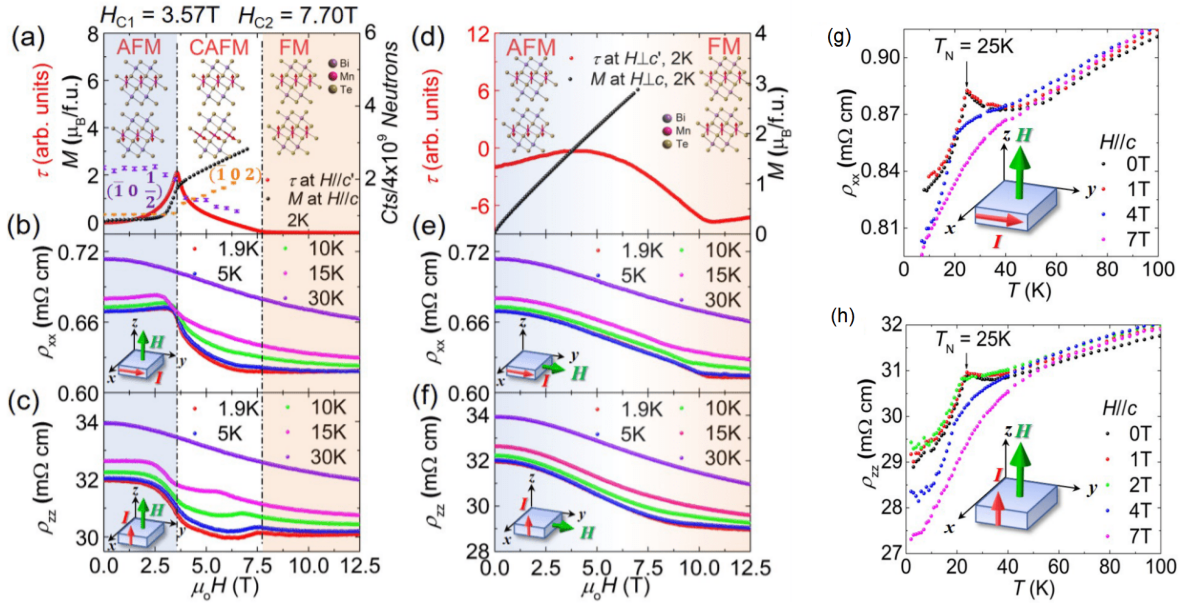

Figure 5.1: Magnetotransport and SQUID results of $MnBi_2Te_4$ bulk crystals[124]. (a) and (d) Field dependence of magnetic torque in out-of-plane direction ($H \| c'$) and in-plane direction ($H \perp c'$). (b) and (c) In-plane resistivity ρ_{xx} for $H \| c'$ and $H \perp c'$. (e) and (f) Out-of-plane resistivity ρ_{zz} for $H \| c'$ and $H \perp c'$. (g) and (h) Temperature dependence of ρ_{xx} and ρ_{zz}.

properties of thin $MnBi_2Te_4$ nanostructures were still not clarified. As $MnBi_2Te_4$ is an ideal stage to study the magnetic properties of van der Waals antiferromagnets, especially their unique layer-dependent magnetism, further studies of $MnBi_2Te_4$ nanostructures are necessary.

5.2 Magnetotransport properties of $MnBi_2Te_4$ nanostructures

5.2.1 Temperature dependence of magnetoresistivity

The longitudinal resistance of $MnBi_2Te_4$ at zero field as a function of temperature was measured during the cooling of the sample in cryogenics. It has a linear decrease at high temperature (Fig. 5.2(a)), which is typical for metals, where phonon scattering has a dominating contribution to the resistivity at high temperature. The residual resistivity ratio (RRR) of the sample (ATMBT13), which implies the amount of disorder in the material, is $\rho(300\text{K})/\rho(4.2\text{K}) \approx 2.0$. This is a relatively small value and depends on a strong degree of disorder, similar to the case of non-magnetic topological insulators Bi_2Se_3 and Bi_2Te_3[15]. At low temperatures, phonon scattering is suppressed by reduced thermal fluctuations. The scattering events will then mainly be spin scattering and scattering on disorders. If a high magnetic field ($B = 10\text{T} > B_{\text{sat}}$) is applied during the cooling, the spin scattering contribution can be suppressed, and mainly the scattering on disorders remains. The power-law fitting of the temperature dependence of resistivity at $B = 10\text{T}$ reveals a quadratic behavior $\rho \sim T^{1.9984 \pm 0.0024}$ (Fig. 5.2b), which confirms the disordered metallic nature of the material[126].

During the cooling of the sample at $B = 0$, a small resistivity peak at 23K was observed, which can be attributed to the enhanced spin scattering at the Néel transition[124]. This Néel transition temperature was slightly lower for our nanostructures than that of the previously reported bulk crystals. When a finite field is applied along the easy axis during the cooling, one can observe the shift of the resistivity peak towards lower temperature for $B < B_{\text{sf}}$. For higher magnetic field, the resistivity peak at $T < T_N$ is suppressed (Fig. 5.3), but the resistivity still

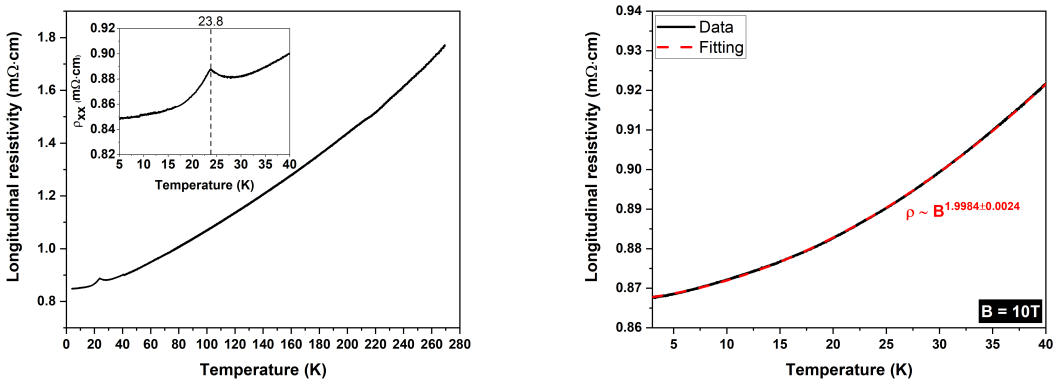

(a) (b)

Figure 5.2: Temperature dependence of longitudinal resistance of $MnBi_2Te_4$ at (a) $B = 0$ and (b) $B = 10$T (sample ATMBT13).

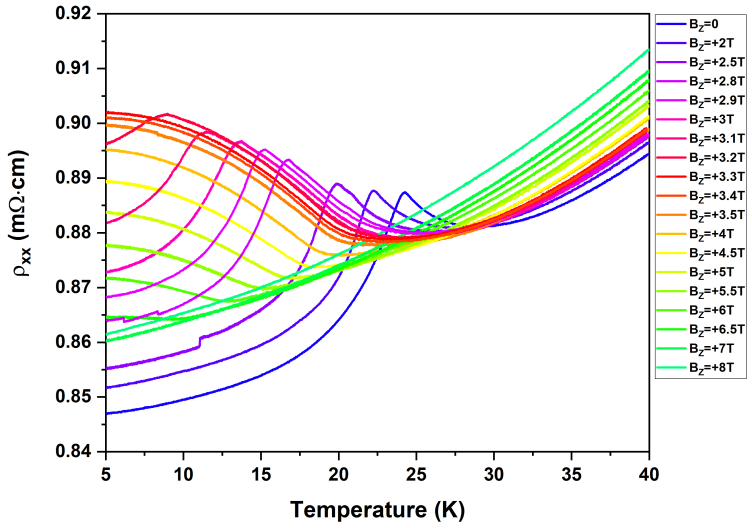

Figure 5.3: Temperature dependence of longitudinal resistance of $MnBi_2Te_4$ at finite magnetic field.

shows an upturn at low temperatures, with a smaller amplitude for larger fields. The overall trend of the magnetoresistivity implied by the results shown in Fig. 5.3a is: It increases with the external magnetic field and then decreases as soon as $B > B_{sf}$. This can be also seen in the direct measurement of magnetoresistivity at low temperatures (Fig. 5.4a).

At $T = 3$K, as the magnetic field swept along the c axis (out-of-plane direction), the longitudinal magnetoresistivity showed remarkable peaks around ± 3.2T and upturns around ± 7.2T (Fig. 5.4a). The resistivity peaks suggest the occurrence of spin-flop transitions. However, the results shown here are in contrast with the results of Lee *et al.*. The resistivity at spin-flop transitions did not experience a monotonous decrease, and hence could not be explained by the spin-valve effect. More results on the longitudinal magnetoresistivity are presented in Chapter 5.2.3, reporting on a comparative study between different exfoliated samples. The upturns around ± 7.2T on the other hand suggests that the positive magnetoresistivity is only due to disorder, as expected in

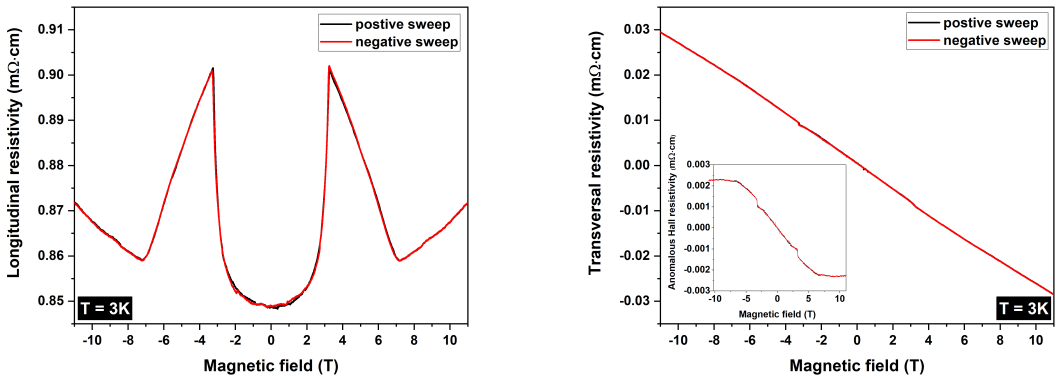

Figure 5.4: Magnetoresistivity of $MnBi_2Te_4$ measured at 3K (sample ATMBT13). (a) Longitudinal resistivity, (b) Transversal resistivity with the anomalous Hall resistivity shown in the inset.

the colinear regime above the saturation field. This evolution with the magnetic field from an A-type antiferromagnet, to an canted state and finally to a fully aligned magnetic state is also confirmed by transverse magnetoresistivity measurements.

Generally speaking, the normal Hall effect has a major contribution to the transverse magnetoresistivity. Therefore, the transverse magnetoresistivity has a dominating linear background (Fig. 5.4b). In the measurement of Hall resistivity, a misalignment contribution may follow if the patterned Hall crosses are not perfectly symmetric or the contacts are not identical[127]. This contribution is symmetric under the positive and negative magnetic field, whereas the normal Hall resistivity is antisymmetric. Therefore, one may obtain the Hall resistivity by extracting the antisymmetric component from the transverse resistivity, that is $\rho_{\mathrm{H}} = [\rho_{xy}(B) - \rho_{xy}(-B)]/2$. However, one should be careful to extract the Hall resistivity in this manner, since the anomalous Hall resistivity, unlike the normal Hall resistivity, is not necessarily antisymmetric. Here, the antisymmetric anomalous Hall resistivity is assumed, according to the fact the spin-flop transitions are symmetric and there has been no magnetic hysteresis observed in the measurement of longitudinal magnetoresistivity (Fig. 5.4a). By further subtracting the linear Hall background according to the Hall slope at high magnetic field ($B > 8$T), one can obtain the anomalous Hall resistivity as shown in the inset of Fig. 5.4b. The abrupt jump of anomalous Hall resistivity confirms the spin-flop transitions around $\pm$3.2T. However, the onset of the anomalous Hall plateaus is around $\pm$6.8T, which is slightly smaller than the upturn field inferred from the longitudinal magnetoresistivity shown in Fig. 5.4a. Importantly, a relatively large difference between the spin-flop transition field and the saturation field is confirmed. This suggests a large canting angle after the spin-flop transition, and implies relatively large interlayer exchange coupling in $MnBi_2Te_4$.

By measuring the sample at different temperatures, the temperature dependence of the transition fields was observed. (Fig. 5.5). As the temperature increases, the transition fields for spin-flop (estimated by the position of the resistance peaks) become smaller, as expected from the temperature dependence of the anisotropy constant. The temperature evolution of the spin-flop transition field could be explained by the thermal fluctuation of the magnetization. Below 5K, the transition field is barely changed around 3.2T (inset II in Fig. 5.5b). Close to the Néel temperature, the transition field decreases and approaches zero rapidly, as also can be seen from the merging of the resistance peaks (Fig. 5.5a). This confirms the Néel transition around 23K. Above the Néel temperature, the magnetoresistance typically shows a quadratic behavior due to the cyclotron motion of carriers. Close to the Néel temperature, the thermal fluctuation is

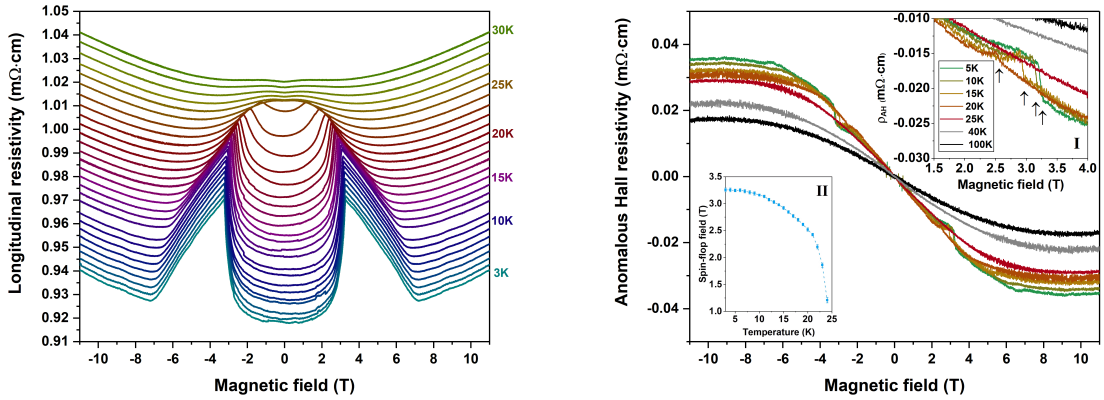

(a) (b)

Figure 5.5: (a) Temperature dependence of longitudinal magnetoresistivity. Curves are shifted for clarity. (b) Temperature dependence of anomalous Hall resistivity of $MnBi_2Te_4$. No shifting for the curves. Inset I: A Zoom-in near the spin-flop transitions. Inset II: The spin-flop transition field as a function of temperature. (Sample ATMBT13)

large enough to overcome the exchange and anisotropy barrier. Therefore, a relatively small field is sufficient for the transition. Whereas at lower temperature, the thermal fluctuation is suppressed. The transition field will be mainly determined by the magnetic anisotropy and the exchange coupling ($B_{\mathrm{sf}} \sim \sqrt{JK}$). A higher field is required for the spin-flop transition.

A summary that shows the different magnetic phases at different temperatures and magnetic fields is shown in Fig. 5.6a. In contrast to the work by J. Cui *et al.*[128], the phase diagram shown here suggests the saturation field does not drop to zero as the temperature approaches the Néel temperature, which is reasonable, since the thermal fluctuation at this temperature can prevent the system from reaching the saturated state. Also, there can be significant canting at low field near the Néel temperature, which is not suggested by the results of J. Cui *et al.*. However, the saturation transition can be extrapolated at a temperature beyond the Néel transition, which implies magnetic exchange coupling exists already before the Néel transition actually occurs. In fact, strong intraplane ferromagnetic correlations have been evidenced for another $[MnBi_2Te_4][Bi_2Te_3]_n$ derivative, $MnBi_4Te_7$ ($n = 1$), up to 30K[10].

One can notice that although the saturation value of anomalous Hall resistivity decreases with increasing temperature, it does not vanish when $T > T_{\mathrm{N}}$. To further confirm this, the Hall resistivity was measured at higher temperatures up to 200K. The Hall resistivity $\rho_{\mathrm{H}} = R_0 B + \rho_{\mathrm{AH}}(M_{\mathrm{s}})$ can be separated into normal Hall resistivity and anomalous Hall resistivity by using the method mentioned before. The normal Hall coefficient $R_0 = \rho_{\mathrm{xx}}\mu$ has a behavior similar to that of longitudinal resistivity (Fig. 5.6b cf. Fig. 5.2a). The overall decreasing trend of R_0 with the decreasing temperature suggests an increasing of carrier density at lower temperature ($R_0 = 1/ne$), which is uncommon for metallic systems. The extracted mobility is shown in the inset in Fig. 5.6. It is in the range of 300-500 $\mathrm{cm^2V^{-1}s^{-1}}$ (cf. Appendix C), and is less than one half of the mobility of pure Bi_2Te_3 ($\sim 1000\mathrm{cm^2V^{-1}s^{-1}}$)[129, 130]. For bulk crystals, even poorer mobility has been reported (79 $\mathrm{cm^2V^{-1}s^{-1}}$[124], 100 $\mathrm{cm^2V^{-1}s^{-1}}$[9]). This could be due to the nonnegligible amount of Mn/Bi antisites and cation vacancies (cf. Chapter 4.1). Due to the low mobility of the material, no Shubnikov-de-Haas oscillation has been observed so far.

The saturation value of anomalous Hall resistivity decreases dramatically around the Néel temperature. However, it decreases slowly after crossing T_{N} and maintains a finite value up to 200K (highest temperature in the measurement). The reason for the finite anomalous Hall

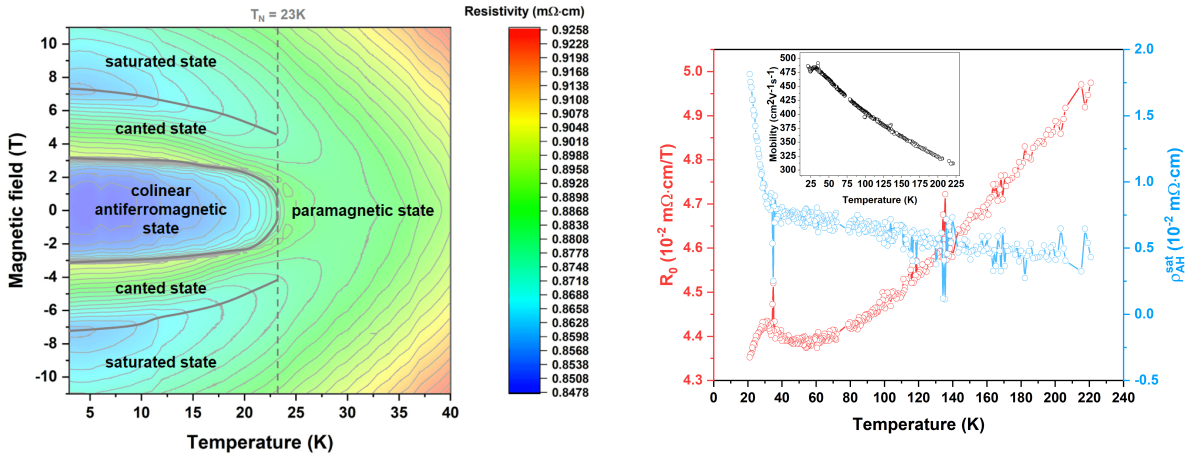

(a) (b)

Figure 5.6: (a) The contour plot of longitudinal resistivity as a function of the temperature and the magnetic field. The transition boundaries between different magnetic phases were determined by the contour lines. The Néel temperature is depicted with the dashed line as a guide to the eye. (b) The Hall coefficient R_0 and saturation value of anomalous Hall resistivity of $MnBi_2Te_4$ as a function of temperature. Inset: The mobility $\mu = R_0/\rho_{xx}$ as a function of temperature. (Sample ATMBT13)

resistivity at high temperature is still unclear. It could be due to Van Vleck susceptibility. Materials belong to the Bi_2Se_3-family can have substantial Van Vleck susceptibility and this susceptibility depends weakly on the temperature (cf. Chapter 3.2.2). Another possibility can come from the contribution from different bands. In the previous discussion, a linear response of normal Hall resistivity is assumed. This is valid only for the single-band case. In the case of multiband, the normal Hall resistivity can have nonlinear behaviors. Therefore, there can be finite values of Hall resistivity residues.

5.2.2 Angular dependence of magnetoresistance

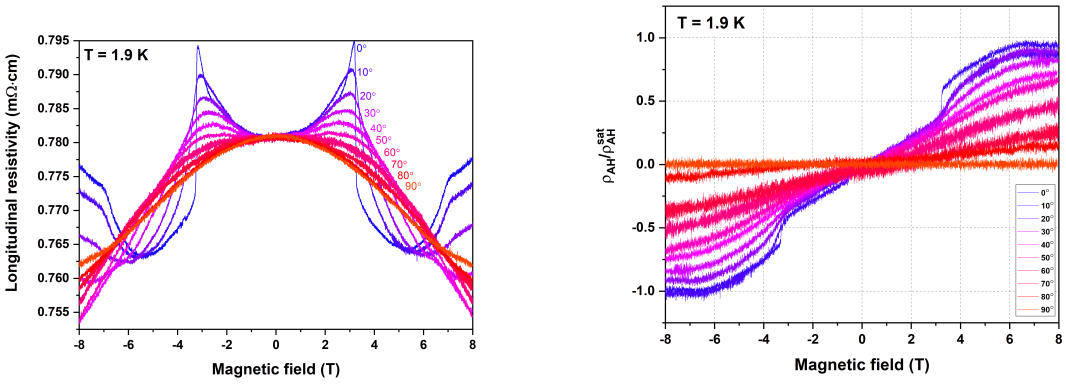

(a) (b)

Figure 5.7: Angular dependence of magnetoresistivity of $MnBi_2Te_4$ (sample ATMBT7). (a) The longitudinal magnetoresistivity measured at different angles. (b) The normalized anomalous Hall resistivity measured at different angles.

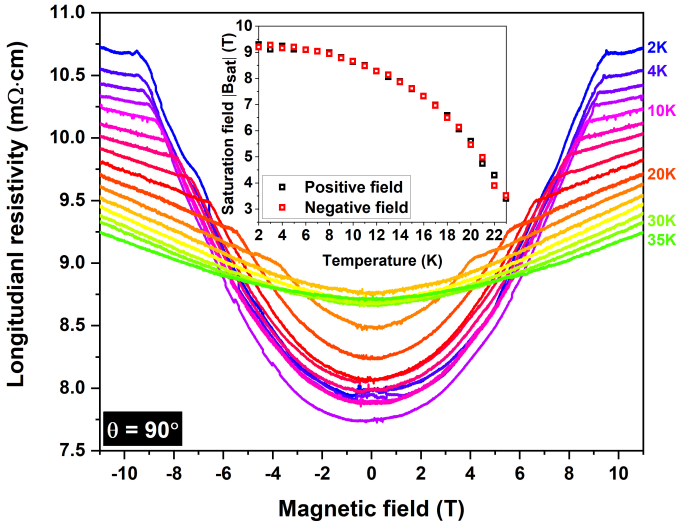

Figure 5.8: Magnetoresistivity measured at different temperatures when the external magnetic field is applied in the ab plane ($\theta = 90°$). (Sample ATMBT13)

In order to further investigate the magnetic properties of $MnBi_2Te_4$, the magnetoresistivity was measured at different field angles. By varying the angle θ between the applied field and the easy axis ($\theta = 0°$ for magnetic field along the easy axis), a strong angular dependence of the magnetoresistivity was observed. The magnetoresistivity peaks at the spin-flop transition decreased rapidly upon increasing field angle and it vanished at an angle of about 40° (Fig. 5.7a). This behavior is typical for A-type antiferromagnets with an exchange coupling much larger than the anisotropy ($J \gg K$), for which the spin-flop transitions are only limited to small field angles. For large angles, the longitudinal magnetoresistivity decreased smoothly, due to the coherent rotation of the multilayer magnetization.

The strong angular dependence of magnetic properties of $MnBi_2Te_4$ can be also verified by the anomalous Hall resistivity (Fig. 5.7b). The anomalous Hall resistivity here is normalized to the value at saturation ($\theta = 0°$). At $\theta = 0°$, the spin-flop transition rendered a sharp jump in the anomalous Hall resistivity. As soon as θ increases, this sharp change disappeared. The saturated value of ρ_{AH} also became smaller, as expected for a reduced component of the magnetization perpendicular to the plane. In particular, the anomalous Hall resistivity remained unchanged for $\theta = 90°$. This implies the coherent rotation is accompanied by perfect compensation of magnetization along the c axis. These results show consistency with the results in Fig. 5.7a, and confirm the easy axis being the c axis and the proper alignment of the measurement setup.

When the field was applied in the *ab* plane, remarkable kinks in the magneto-resistance which implies the saturation of magnetization appeared at high magnetic field. The saturation field was around 9.4T at T=2K (Fig. 5.8), which is considerably larger than the out-of-plane saturation field (∼7T). This can be easily understood since a larger Zeeman energy is required to overcome the anisotropy energy barrier in addition to the interlayer exchange coupling. Also, the temperature dependence of this saturation field is similar to that of the magnetization. Below the saturation field, the magnetoresistivity has a quadratic (or sub-quadratic) behavior, and beyond the saturation field, the magnetoresistivity increases more mildly. The increase of magnetoresistivity when $T < T_N$, $B < B_{sat}$ is significantly stronger than the increase of magnetoresistivity at $T > T_N$. This implies that this large increase of magnetoresistivity can not be explained by the cyclotronic motion of carriers alone, but there could rather be an anisotropic magnetoresistance

contribution, which changes as the magnetic moments are aligned in the plane as the field increases. The saturation field, despite its decreasing trend, does not drop rapidly to zero as the spin-flop transition field (cf. Fig.5.5). But the kinks that suggest the saturation (as well as the large change of magnetoresistivity at $B < B_{\mathrm{sat}}$) disappear suddenly as soon as the temperature is larger than T_{N}. This behavior is similar to the case where the field is applied along the easy axis, as in both cases the saturation field can have finite values when extrapolated beyond the Néel temperature (cf. Fig. 5.6a), suggesting that a strong intralayer coupling exists at $T > T_{\mathrm{N}}$.

5.2.3 Comparative studies of $MnBi_2Te_4$ nanostructures

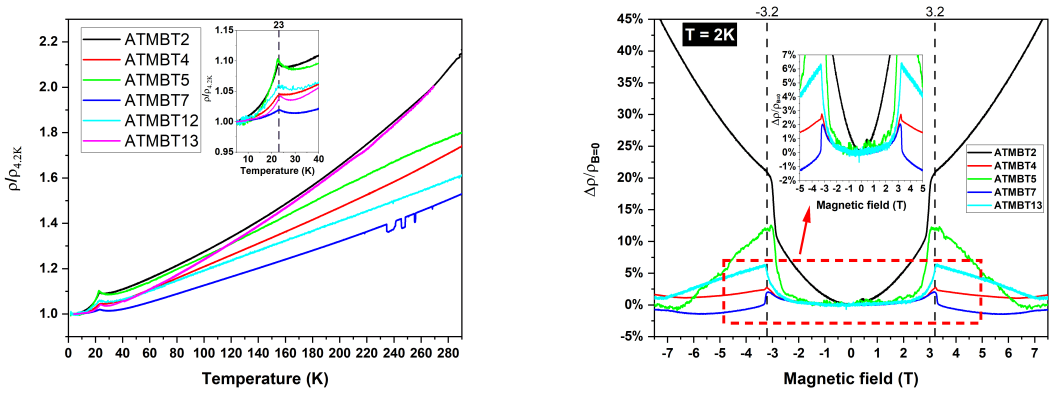

(a) (b)

Figure 5.9: (a) The temperature dependence of the relative longitudinal resistivity $\rho/\rho_{4.2\mathrm{K}}$ and (b) the relative magnetoresistivity $\Delta\rho/\rho_{B=0}$ of different $MnBi_2Te_4$ nanostructures.

J. Cui *et al.* reported there can be large inhomogeneities in bulk $MnBi_2Te_4$ crystal which results in large chemical potential fluctuation among exfoliated nanostructures[128]. The authors suggested that the transport properties of $MnBi_2Te_4$ nanostructures may vary from being metallic to being insulating. However, such observations may also arise from the qualities of the contacts. In order to identify the sample-dependent and sample-independent properties of the material, several different samples were studied in this work. The temperature dependence of the relative longitudinal resistivity $\rho/\rho_{4.2\mathrm{K}}$ is shown in Fig. 5.9a. For all the samples studied in this work, the RRR remains small, as expected in the dirty metal regime. At $T > 50$K, their temperature dependence of resistivity has similar metallic behaviors. These results suggest these samples have similar levels of disorders, and should have transport properties that remained dominated by the bulk. The RRR, mobility, carrier density and thickness of these samples are summarized in Table 5.1. For all sample shown here, the carrier density is typically large and the mobility remains poor.

The Néel transition temperature $T_{\mathrm{N}} \approx 23$K does not vary from sample to sample as inferred by the resistivity peaks. In a first approximation, it suggests the magnetic ordering is independent of the carrier density. This is a remarkable distinction between stoichiometric and diluted Mn-magnetic topological insulators. In diluted Mn-magnetic topological insulators, the magnetic ordering temperature can rather depend on the carrier density, since the magnetic exchange interaction is mediated by the carriers, as has been shown in $Mn_xBi_{2-x}Se_yTe_{3-y}$[6] (cf. Chapter 3.2.1). In contrast, in metallic $MnBi_2Te_4$, there can be other exchange mechanisms that coexist with the carrier-mediated exchange interaction, such as the superexchange coupling, which may dominate in this system so that the influence of the carrier density is small. In addition, the spin-flop transition field also does not vary much regardless of the large difference of carrier density

from sample to sample (Fig. 5.9b). At $T = 2$K, all samples have similar spin-flop transition field around ± 3.2T. It is an evidence of that both the exchange interaction and the anisotropy are independent of the carrier density. This on one hand allows us to maintain the magnetic properties of $MnBi_2Te_4$ when tuning the Fermi level, which is crucial so as to realize the quantum anomalous Hall state in ultra-thin $MnBi_2Te_4$ samples, but on the other hand this limits the possibility to modify the magnetic properties, with an electrical gate for instance.

Sample	Resistivity at 2K (mΩ·cm)	Mobility at 2K (cm·V^{-1}s^{-1})	Carrier density at 2K (cm^{-3})	Thickness (nm)
ATMBT2	1.53±0.04	225±11	$1.80 \pm 0.040 \times 10^{19}$	99±2
ATMBT4	0.506±0.047	286±37	$4.31 \pm 0.16 \times 10^{19}$	54±2
ATMBT5	1.87±0.21	523±99	$6.37 \pm 0.49 \times 10^{18}$	26±2
ATMBT7	1.11±0.07	149±15	$3.74 \pm 0.13 \times 10^{19}$	56±2
ATMBT13	0.85±0.06	456±57	$1.61 \pm 0.09 \times 10^{19}$	40±2

Table 5.1: Summary of main physical parameters of $MnBi_2Te_4$ nanostructures studied in this work.

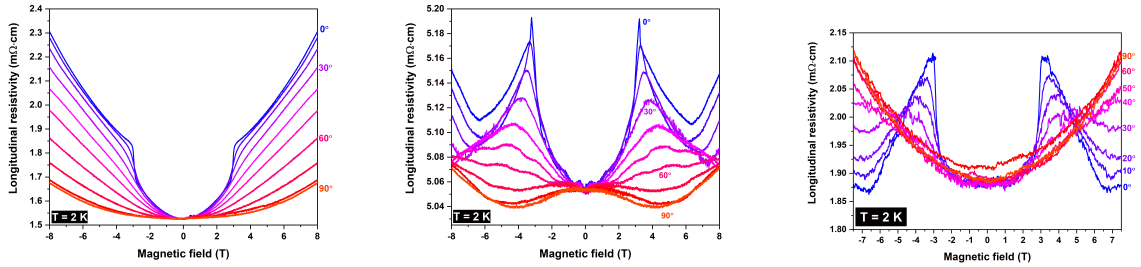

(a) **(b)** **(c)**

Figure 5.10: The angular dependence of magnetoresistivity of sample (a) ATMBT2 (b) ATMBT4 and (c) ATMBT5.

However, it is worth noting that the magnetoresistivity of different samples showed different behaviors. For sample ATMBT4, ATMBT5 and ATMBT13, they have a similar sharp increase of magnetoresistivity close to the spin-flop transition, followed by a decrease before the saturation is reached. For ATMBT7, the magnetoresistivity shows a similar increase at low field, but along with a sharp decrease close to the spin-flop transition. Then a milder decrease follows until the saturation is reached. In contrast, the sample ATMBT2 has a much stronger resistivity increase at the spin-flop transition when compared with others, and has a general increasing trend over the full field range in the measurement. Furthermore, there is also a large discrepancy of the relative magnetoresistivity $\Delta\rho/\rho_{B=0}$ amplitude among the samples. At $B = 8$T, its value can vary from ∼-1% to ∼45%.

In the measurements, differences of angular dependence among the samples were also identified (Fig. 5.10, cf. Fig. 5.7). Having the fact that the spin-flop transitions were suppressed as the field angle increased, we can safely conclude the proper alignment of the samples in the field and perpendicular anisotropy of $MnBi_2Te_4$. However, it was unexpected that for large angle ($\theta \sim 90°$), there can be positive or negative magnetoresistivity. For sample ATMBT4, the magnetoresistivity at $\theta = 90°$ even shows a small hysteresis. Even at high field, $\rho(\theta = 0°, B = 8\text{T})$ can be larger or smaller than $\rho(\theta = 90°, B = 8\text{T})$.

The discrepancy of the magnetoresistivity among the samples remains unclear. Lee *et al.* explained the change of magnetoresistivity by the spin-valve effect in their work[124]. However, it could not explain the discrepancy in our observation. Small differences of Néel temperature T_N

and spin-flop transition field B_{sf} among the samples suggest the discrepancy does not arise from the different magnetic properties. There are several possible explanation for this discrepancy:

1. Geometric effects may exist. For samples with different thickness, surface contribution can vary. For example, surface-related scattering may happen on different field range for different thicknesses when the in-plane field increases.
2. It should be noticed that for all n-doped samples, they have similar decreases after the spin-flop transitions, while the p-doped sample has nevertheless increases and large magnetoresistivity at $B > B_{sf}$. This implies the Fermi level can affect the magnetoresistivity. For n-doped samples, as the carrier density decreases (Table 5.1), the change of magnetoresistivity at the spin-flop transition $\Delta\rho(B = B_{sf})/\rho(B = 0)$ tends to increase. When the sample is p-doped, there is an even large $\Delta\rho(B = B_{sf})/\rho(B = 0)$ value. Nevertheless, this should be further proved by tuning the Fermi level by an applied gate voltage.
3. One may also notice that the detail of the magnetoresistivity depends also on the chemical doping, which was reported by B. Chen *et al.* for Sb-doped $MnBi_2Te_4$[131]. Such chemical doping changes not only the chemical potential, but also the band structure, as evidenced with the closing of topological surface band gap with increasing Sb content. The results in this work (in particular for sample ATMBT4, ATMBT5 and ATMBT7) are similar with the reported results of 25% Sb-doped $MnBi_2Te_4$, which showed a increase of magnetoresistivity near the spin-flop transition, further followed by a slow decrease. In addition, the Néel transition temperature of the samples studied in our work (around 23K) is also comparable with that of 25% Sb-doped $MnBi_2Te_4$. These samples have slightly lower T_N compared with pure $MnBi_2Te_4$ ($T_N = 25$K). Note that our materials do not have any chemical doping. The results of B. Chen *et al.* suggest that not only the chemical potential, but also the band structure have an influence on the details of the magnetoresistivity. The change of the chemical potential and the band structure can be caused by the chemical doping, or in our case, possibly by Mn/Bi intermixing.

Chapter 6

The weakly coupled antiferromagnetic topological insulator: $MnBi_4Te_7$

By inserting non-magnetic Bi_2Te_3 spacers, derivatives of $MnBi_2Te_4$ can be obtained. Here we show that the single-spacer compound $MnBi_4Te_7$ already realizes the weak interlayer exchange coupling regime, and its magnetic properties are actually representative of all $[MnBi_2Te_4][Bi_2Te_3]_n$ compounds with $n \geq 1$. Importantly, contrary to 124 for which $J > K$, other compounds can have a dominant anisotropy, as compared to the interlayer exchange, which favors a fully-magnetized metamagnetic state at low temperatures.

6.1 Magneto-transport properties of $MnBi_4Te_7$ bulk crystals

The magnetic properties of $MnBi_4Te_7$ bulk crystals have been reported by Wu *et al.*[114]. The measured susceptibility shows that the $MnBi_4Te_7$ remains an antiferromagnet with perpendicular anisotropy (Fig. 6.1a). The Néel temperature is around 12.7K, as shown by the abrupt increase of the magnetic susceptibility in the zero-field-cooled curve and the field-cooled curve obtained by the VSM measurement (Fig. 6.1a). The T_N here is noticeably lower than that of $MnBi_2Te_4$. Below the Néel temperature and above around 8K, typical spin-flop transitions of antiferromagnets are observed (Fig. 6.1b-f). The onset of the transitions is in general between 0.1T and 0.2T, which is much smaller than the spin-flop transition field of $MnBi_2Te_4$ at the same temperature. Surprisingly, at a lower temperature, magnetic hysteresis can be observed and the material evolves into a state similar to the ferromagnetic state, where saturated magnetic remanence can exist (Fig. 6.1b-d). The same behavior is also visible in the longitudinal resistivity shown in Fig. 6.1e and Fig. 6.1f. Below T_N, symmetric peaks in the magnetoresistance are observed at the spin-flop transition, as observed for $MnBi_2Te_4$. However, a non-monotonous behavior is evidenced at lower temperatures, with a decrease of the switching field and the onset of a hysteresis behavior, below about 5K.

Similar results have also been reported by Vidal *et al.*[10]. They identified a Néel transition at 13K. In addition to the results similar to that of Wu *et al.*, they further reported a anomaly in the longitudinal resistivity and the FC/ZFC magnetization near 5K (Fig. 6.2a-6.2c), which corresponds to the transition from the colinear antiferromagnetic state to a ferromagnetic-like state (Fig. 6.2d-6.2f). However, both the work of Wu *et al.* and Vidal *et al.* suggest a ferromagnetic state below about 5K. In this work, it is shown that despite the magnetization curves are similar to that of ferromagnets, the low temperature magnetic properties of $MnBi_4Te_7$ is controlled by its dominating uniaxial magnetic anisotropy. The interlayer exchange remains nonetheless antiferromagnetic, however small it is.

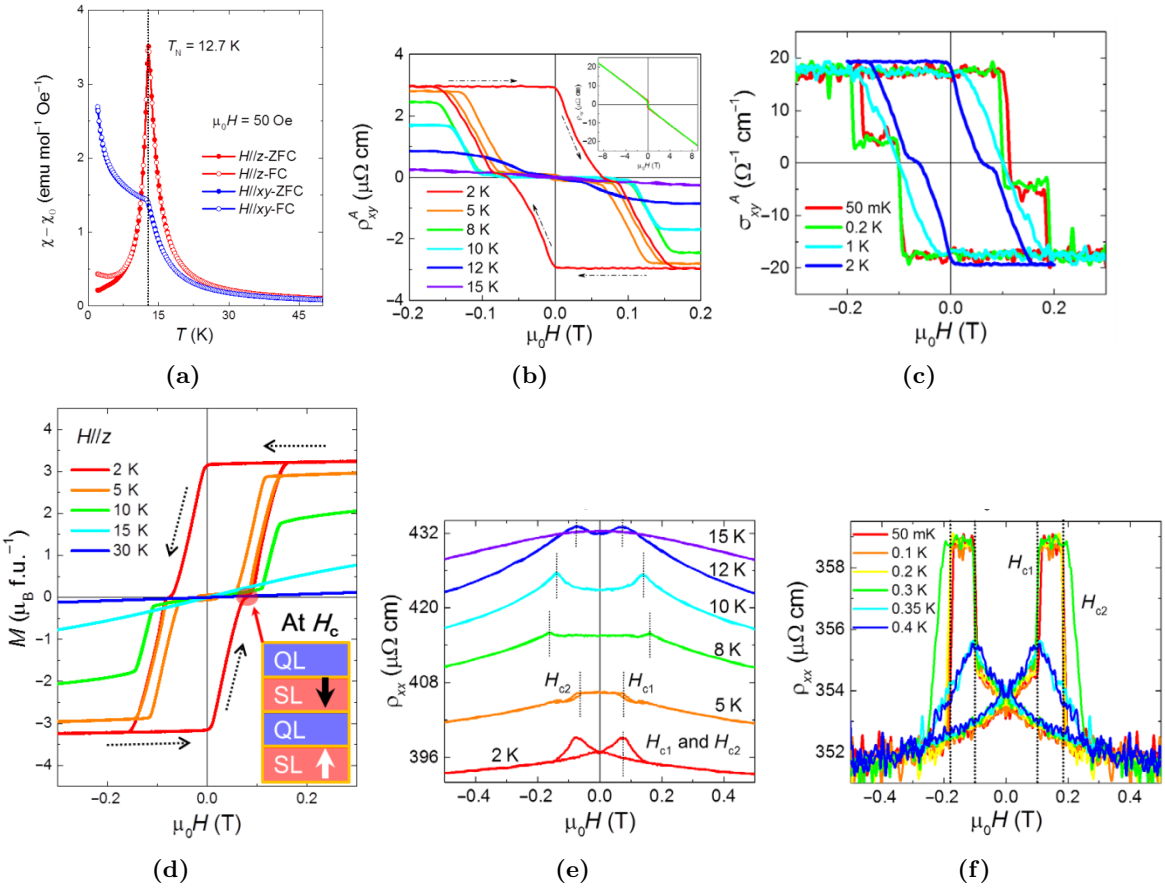

Figure 6.1: VSM and magnetotransport results of $MnBi_4Te_7$ bulk crystals. (a) Magnetic susceptibility measured in field-cooled and zero-field-cooled conditions. (b) and (c) The anomalous Hall resistivity and the anomalous Hall conductivity at different temperature. (d) The magnetization curves measured by VSM at different temperature. (e) and (f) The longitudinal resistivity at different temperature. (Adapted from [114])

6.2 Magnetotransport properties of thin $MnBi_4Te_7$ nanostructures

6.2.1 Magnetoresistance above T_B

In this work, patterned $MnBi_4Te_7$ nanostructures were measured (sample FMBT1 and FMBT7, comparison of their basic transport properties is shown in Appendix C). The temperature dependence of the longitudinal resistance of $MnBi_4Te_7$ is similar to that of $MnBi_2Te_4$, having a typical metallic behavior ($\rho \sim aT + b$) at higher temperature ($T > 50$K). The residual resistance ratio $\rho(300\text{K})/\rho(4.2\text{K}) \approx 1.96$ is typical of highly-disordered topological insulators, as found also for non-magnetic binary compounds such as Bi_2Se_3 and Bi_2Te_3. This implies that the material has a similar degree of microscopic disorder with $MnBi_2Te_4$. The resistivity peak that indicates the Néel transition appeared at 12K, which is consistent with the results of Wu *et al.*[114]. This noticeable difference between the Néel temperature of $MnBi_2Te_4$ and that of $MnBi_4Te_7$ suggests a difference of the relative interlayer coupling strength J_{AF}/J_F for the two materials. For a stack of 2D ferromagnets with an intralayer ferromagnetic exchange coupling J_F and an interlayer antiferromagnetic coupling J_{AF}, the Néel temperature given by the mean-field theory is[132]

$$T_N = C'(J_F - J_{AF}) \tag{6.1}$$

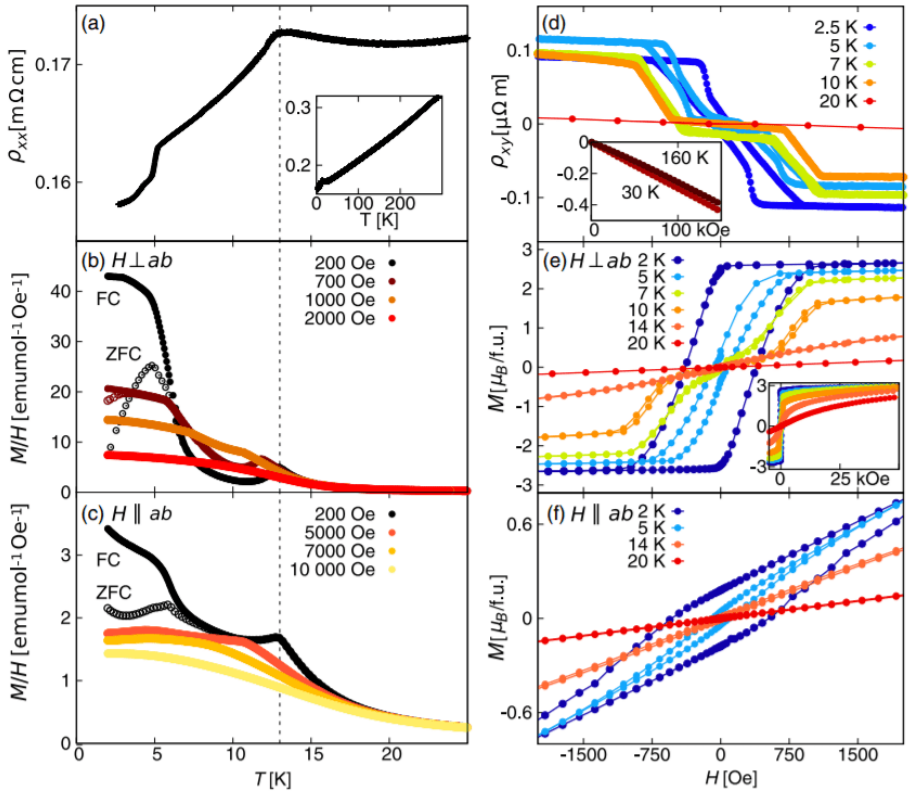

Figure 6.2: Magnetic and magneto-transport properties of $MnBi_4Te_7$ bulk crystals. (a) The in-plane resistivity as a function of the temperature. (b) and (c) The field-cooled (FC) and zero-field-cooled (ZFC) magnetization under a magnetic field applied perpendicular and parallel to the *ab* plane, respectively. (d) The Hall resistivity as a function of temperature with the field applied perpendicular to the *ab* plane. (e) and (f) The magnetization curves at different temperatures with the field applied perpendicular and parallel to the *ab* plane, respectively. (Adapted from [10])

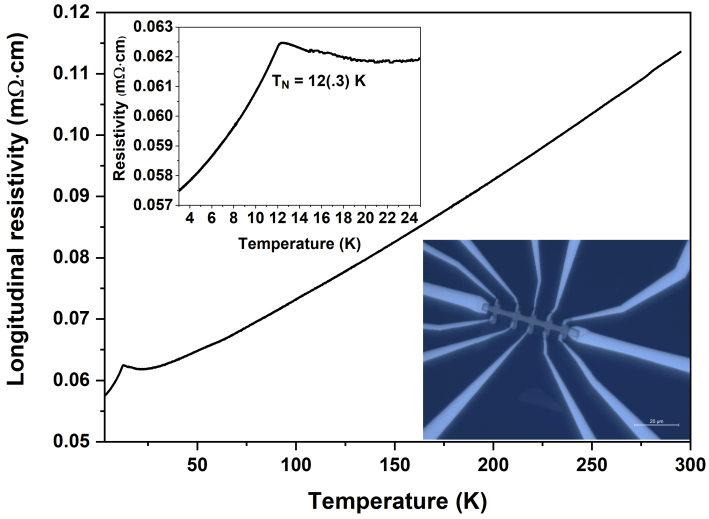

Figure 6.3: The longitudinal resistance of $MnBi_4Te_7$ as a function of temperature measured during the zero-field-cooled. (Sample FMBT1)

and the paramagnetic Curie temperature is given by

$$\theta_p = C'(J_{\mathrm{F}} + J_{\mathrm{AF}}), \tag{6.2}$$

where $C' = C/2$ and C is the Curie constant. Combining the two equations, one can obtain $J_{\mathrm{AF}}/J_{\mathrm{F}} = (1 - \theta_p/T_N)/(1 + \theta_p/T_N)$. It shows that the relative interlayer coupling strength is related to the ratio between the Curie-Weiss temperature and the Néel temperature. The Curie-Weiss temperature can be obtained by fitting the temperature dependence of the magnetic susceptibility with the Curie-Weiss law in the high-temperature region. It turns out that the Curie-Weiss temperature is small for $MnBi_2Te_4$ ($\theta_p \sim 3(3)K$)[9] compared with that of $MnBi_4Te_7$ ($\theta_p \sim 13.7K$)[10]. The relative interlayer coupling strength for $MnBi_2Te_4$ obtained is $J_{\mathrm{AF}}/J_{\mathrm{F}} \approx -0.86$. For a such value, it seems there is in fact competing interlayer and intralayer coupling in $MnBi_2Te_4$. In contrast, $MnBi_4Te_7$ has $J_{\mathrm{AF}}/J_{\mathrm{F}} \approx -0.066$, which indicates the interlayer coupling is significantly smaller than the intralayer coupling, given that the exchange interaction in the septuple layers is unchanged. This suggests that the magnetic ordering at 12K for $MnBi_4Te_7$ is actually dominated by the intralayer coupling rather than the interlayer coupling as in $MnBi_2Te_4$. $MnBi_4Te_7$ is close to a situation of weakly-coupled 2D ferromagnets, whereas $MnBi_2Te_4$ has a 3D long-range order. In fact, Monte Carlo simulation predicts the Curie temperature at 12K for a single septuple layer of $MnBi_2Te_4$ (Table. 3.1)[11], but that all other multilayers have Néel temperature around 25K. Both theory and experimental results thus reveal that that because of the non-magnetic spacer Bi_2Te_3, the magnetic layers in $MnBi_4Te_7$ are only weakly coupled, and that these magnetic layers can have behaviors similar to nearly-isolated 2D magnetic planes. It is therefore reasonable to conclude that for other members in the $[MnBi_2Te_4][Bi_2Te_3]_n$ family ($n > 1$), the magnetic ordering temperature should be close to 12K as well, since magnetic septuple layers are even more decoupled from each other. This was indeed confirmed by the recent study on $MnBi_6Te_10$, $MnBi_8Te_{13}$ and $MnBi_{10}Te_{16}$[108]. Here, we can further conclude that $n > 1$ members of $[MnBi_2Te_4][Bi_2Te_3]_n$ have similar magnetism, which can be represented by the magnetic properties of $MnBi_4Te_7$ studied in detail in this chapter. On the other hand, for $MnBi_2Te_4$, the magnetic ordering of multilayers, as suggested by Otrokov *et al.*[11], is stabilized by both the intralayer and the interlayer coupling. Due to its relatively large interlayer exchange coupling, $MnBi_2Te_4$ is the only member in the family that has a higher ordering temperature and prominent A-type antiferromagnetism.

Fig. 6.4a and Fig. 6.4b show the longitudinal and transversal magnetoresistivity measured at different temperatures (including the trace and retrace curves). The longitudinal resistivity peaks appear at $T < 12$K, which confirms the Néel transition at 12K. For results at $T > 8$K, no magnetic hysteresis could be identified. Remarkable jumps of transversal resistivity around ± 0.1T indicate spin-flop transitions similar to those of $MnBi_2Te_4$. However, these spin-flop transitions were observed at a much lower field. The transversal resistivity reaches a plateau after the spin-flop transition, which suggests that the saturation is reached shortly after the spin-flop transition, and that the canting after the spin-flop transition is small. In fact, one can estimate the spin-flop transition field by the anisotropy and exchange coupling of that material through $B_{\mathrm{sf}} \sim \sqrt{JK}$[1]. If we assume $MnBi_2Te_4$ and $MnBi_4Te_7$ have a similar anisotropy, which is indeed intrinsic to the Te-Mn-Te bonds in septuple layers, we will again obtain a much weaker interlayer coupling in $MnBi_4Te_7$. For the magnetization process at a lower temperature, as shown in the next section, the spin-flop transition becomes a spin-flip event and magnetic hysteresis can be observed. For the temperature dependence of spin-flop transition field at $T > 8$K, B_{sf} increases rapidly near T_{N} as temperature decreases, but it goes to a maximum value around 10K and then slowly decreases. However, the amplitude of the Hall resistivity at 0.2T, which is directly related to the out-of-plane magnetization at 0.2T if a constant anomalous Hall coefficient is assumed, increases rapidly

[1]This in general applies when $J \gg K$. However, if $J \sim K$, it should be rewritten as $B_{\mathrm{sf}} \sim \sqrt{JK + K^2}$. Read Chapter 7 for detailed discussions.

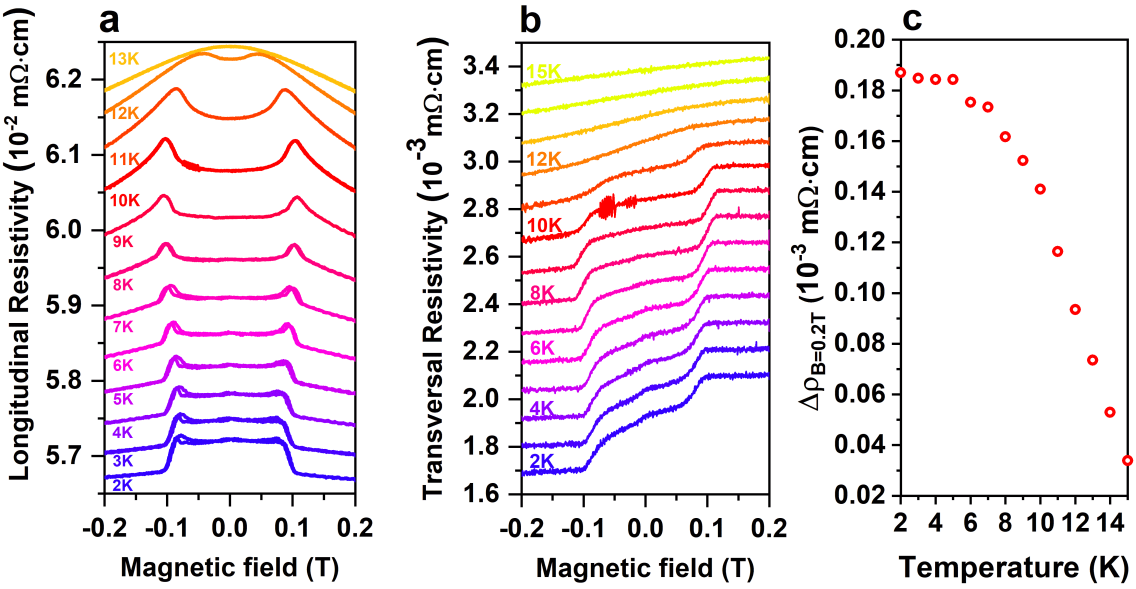

Figure 6.4: (a) The longitudinal magnetoresistivity (no shifts) and (b) the transversal magnetoresistivity (shifted for clarity) measured at different temperature. (c) The amplitude of change of Hall resistivity at 0.2T as a function of temperature. (Sample FMBT1)

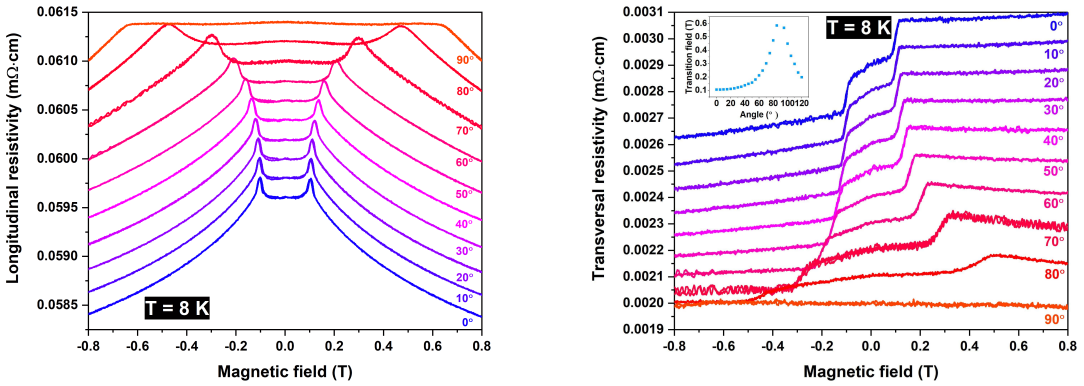

(a) (b)

Figure 6.5: (a) The longitudinal and (b) the transversal magnetoresistivity of $MnBi_4Te_7$ measured at different field angles ($T = 8$K). $\theta = 0°$ represents the field perpendicular to the sample plane (along the easy axis). All curves were shifted for visualization. The inset of (b): The spin-flop transition field as a function of field angle. (Sample FMBT1)

from 15K to 5K. This corresponds well to the reduction of the magnon density of states at lower temperature, and therefore to the increase of the spontaneous magnetization as well as of the effective anisotropy. Therefore the temperature dependence of B_{sf} is not directly related to that of the magnetization, which suggests a change in the magnetic ground state below about 8K.

Similar to the studies on $MnBi_2Te_4$, the angular dependence of magnetoresistivity of $MnBi_4Te_7$ was investigated as well in order to better understand the nature of the spin-flop transition. The angular dependence of the longitudinal and transversal magnetoresistivity at 8K are shown in Fig. 6.5a and Fig. 6.5b. As the field angle increases, the spin-flop transition field increases.

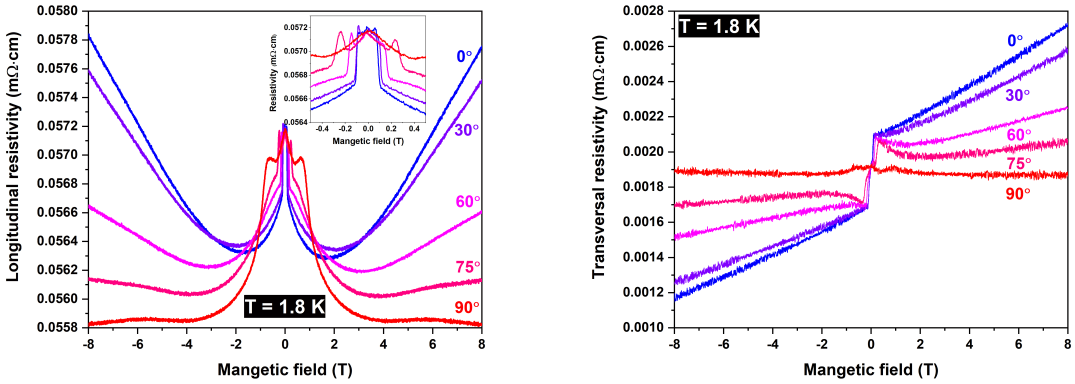

(a) **(b)**

Figure 6.6: (a) and (b) The longitudinal and transverse magnetoresistance of $MnBi_4Te_7$ measured up to 8T. (Sample FMBT1)

The angular dependence of the observed transition field is shown in the inset of Fig. 6.5b. The perpendicular magnetic anisotropy of $MnBi_4Te_7$ is therefore confirmed. In contrast to $MnBi_2Te_4$, the spin-flop transition of $MnBi_4Te_7$ does not disappear rapidly but still remains visible for large angles. This relatively weak angular dependence is typical for a regime $K \sim J$, contrary to the regime $J \gg K$, as shown by the model to be introduced in Chapter 7.

6.2.2 High-field magnetoresistance

The physical properties of $MnBi_4Te_7$ nanostructures were further investigated by measuring the magnetoresistivity up to higher magnetic field. Fig. 6.6 shows such measurements up to 8T. When the external field is applied along the easy axis, after the abrupt decrease at the coercive field, the longitudinal resistivity experiences milder decreases, followed then by stable increases at higher field. For higher field angles, the increasing trend at high field becomes weaker. At $\theta = 90°$, the increasing trend can no longer be observed and the longitudinal resistivity is still slowly decreasing near 8T. Here, the subtlety about the change of longitudinal magnetoresistivity remains veiled. These changes can have different origins. First, there is a low-field negative magnetoresistance, which could be attributed to a spin-valve effect, but this scenario proposed by Lee *et al.* fails to give an explanation about the low-field longitudinal resistivity plateau, since below T_B the magnetization state at zero field can be saturated and with magnetic moments aligned, a higher magnetoresistivity state should not be expected. A more likely explanation is related to a reduction of the magnetic disorder under an applied field, which reduces the spin-dependent scattering contribution to the carriers' mobility. On the other hand, the transversal resistivity has typical linear dependence on the applied field. It follows well the $\cos\theta$ angular dependence. One can identify similar behaviors of longitudinal and transversal resistivity at high field. This suggests the longitudinal resistivity at high field does not depend on the absolute value of the field, but depends on the perpendicular component of the field. This could also be that the angular dependence of the positive high-field magnetoresistivity is intrinsic to the 2D nature of the magnetic sublayers, which in this case is visible in the weak coupling regime.

The carrier density for $MnBi_4Te_7$ can be extracted from the high field Hall resistivity $n_{3D} \approx 1.52(9) \pm 0.034 \times 10^{20}$ cm^{-3} (n-type, $T = 1.8$K, sample FMBT1), which is similar to the result of Wu *et al.*[114] ($n_{3D} \approx 2.85 \times 10^{20}$ cm^{-3}, $T = 2$K). This reveals the carrier density of $MnBi_4Te_7$ is typically one order of magnitude higher than the carrier density of $MnBi_2Te_4$, and therefore it has smaller longitudinal resistivity (∼0.06 mΩ cm, sample FMBT1, compared with

$\sim$1 mΩ cm for $MnBi_2Te_4$). This difference may come from the structural difference of both material. The in-plane conductivity of the septuple layers could be different from that of the quintuple Bi_2Te_3 layers. In addition, these layers can have different structural disorders. While the disorders in the quintuple layers are mainly Te vacancies, Mn/Bi intermixing can exist in septuple layers. The electron mobility of $MnBi_4Te_7$ $\mu \approx 713 \pm 34$ cm^{2}V^{-1}s^{-1} ($T = 1.8$K, sample FMBT1). The observation of quantum transport phenomena is still hindered by the large carrier density contributed by the bulk. Therefore the evidence of the quantum anomalous Hall effect (QAHE) still requires ultra-thin nanostructures.

6.2.3 Meta-magnetism below T_B

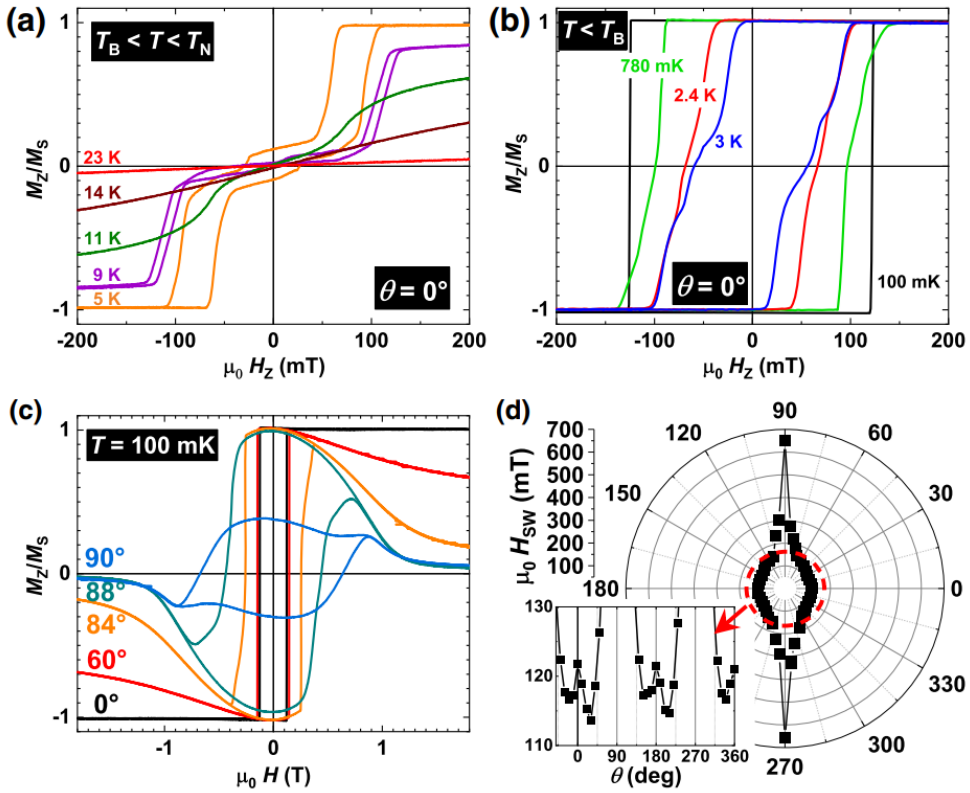

Figure 6.7: (a) and (b) The magnetization along the c axis of $MnBi_4Te_7$ at different temperature. The magnetization values M_Z/M_S were obtained from the Hall resistance normalized by its saturated value at 200mT and at T =100mK . (c) The magnetization curve for different applied field angles. (d) The switching field H_{SW} as a function of applied field angle with respect to the c axis.(Figure taken from [16]) (Sample FMBT7)

The preliminary results shown in the previous section were obtained with a relatively large current ($\sim 4.1 \times 10^7$ A/m^2, due to the native limitation of PPMS), but however did not show hysteresis down to 2K (sample FMBT1, cf. Fig. 6.4), in contrast with the results reported by others[10, 114]. The reason for this remains unclear. At a first glance, near the Néel temperature, the spin-flop transition field changes in a way similar to that of $MnBi_2Te_4$: As the temperature is lowered, the transition field is larger (Fig. 6.4). Below 8K, however, one can identify small hysteresis have been developed. However, this hysteresis was not resolved in the transversal resistivity.

Further electrical measurements were performed with lock-in amplifiers, with which a much smaller current could be applied ($\sim 10^5$ A/m^2). The magnetic hysteresis for $MnBi_4Te_7$ at lower

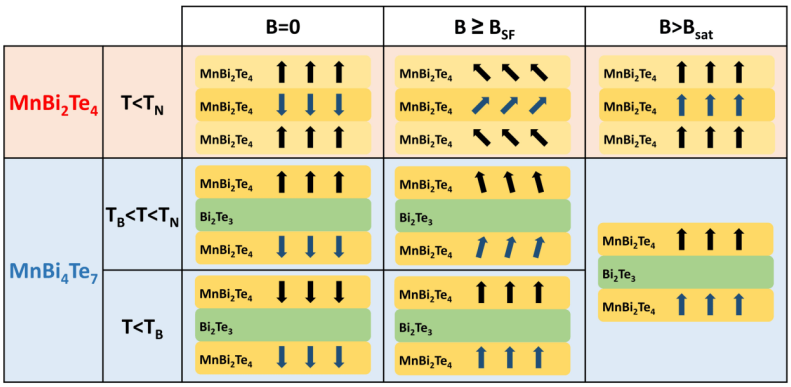

Figure 6.8: A summary of the magnetic behaviors of $MnBi_2Te_4$ and $MnBi_4Te_7$.

temperature was then further investigated (Fig. 6.7). The hysteresis clearly results from the splitting of the spin-flop transitions below 9K, with clearly identified different spin-flop fields $B_{\mathrm{sf1}}, B_{\mathrm{sf2}}$. By comparing the magnetization curves at 5K and 9K in Fig. 6.7a, one can see that instead of monotonously pushing the spin-flop transition to higher field, which is the case for $MnBi_2Te_4$, here the decreasing of temperature further brings the spin-flop transition back to lower fields. Below the blocking temperature ($T_{\mathrm{B}} \approx 3K$), this spin-flop transition field changes its sign and the remanent magnetization remains fully magnetized. The magnetization curve becomes similar to that of a typical ferromagnet. The findings are consistent with the results obtained with bulk crystals by Wu *et al.*[114] and Vidal *et al.*[10]. In this work, we show that the magnetization process is actually achieved by spin-flip events, a magnetization reversal regime that will be explained in detail in Chapter 7. If the temperature is further lowered, both spin-flip transitions (that with an initial parallel state and that with an initial anti-parallel state) occur at a larger field and evolve to the same limit so that the antiferromagnetic configuration is not an intermediate magnetization state anymore. At 100mK, the magnetization was switched sharply, seemingly equivalent to a single domain ferromagnet with a dominant uniaxial anisotropy.

To further confirm that the magnetic states and their reversal are determined by a dominant uniaxial anisotropy, we investigated the angular dependence of the magnetization curves, as shown in Fig. 6.7c and Fig. 6.7d. The magnetization is clearly rotating away from the easy anisotropy axis, and for large angles the coercive field becomes as large as the anisotropy induction, of about 1T. The switching field H_{SW} as a function of field angle shows a distorted Stoner-Wohlfarth astroid in a polar plot. For a single-domain state, H_{SW} has the same maximum for the parallel-field and the perpendicular-field configurations, and a minimum value at 45°. Therefore, this simplified situation would give an astroid with a four-fold symmetry. We attribute the distortion observed for small angles to the existence of magnetic domain walls, which can be moved by the parallel component of the applied field. This is not the case anymore for large angles, for which domain walls are pinned and the coherent rotation of magnetic domains prevails. Details will be discussed in Chapter 7.

The progressive change of the spin-flop transition field from higher field to lower field and the crossing of this transition at zero field to the ferromagnetic-like state suggests the temperature dependence of K/J. For $MnBi_4Te_7$, the condition $J > K$ is satisfied near the Néel transition, but due to the reduced J value, the K/J ratio increases at lower temperatures. The condition $K = J$ is satisfied at the blocking temperature. At even lower temperature, K becomes larger than J. The ferromagnetic-like magnetization behavior of thus comes from the anisotropy energy barrier that Zeeman energy has to overcome in order to switch the magnetization: the magnetization curve is typical of this metamagnetic state. In the case of a magnetic system dominated by its magnetic anisotropy, despite the fact that the interlayer exchange coupling is antiferromagnetic,

the parallel alignment of the magnetic sublayers is favored. The observation here is in contrast with the magnetic properties of antiferromagnets with $J \gg K$. The weak interlayer coupling in $MnBi_4Te_7$ not only leads to the condition $K > J$ at low temperatures, but it also allows us to observe the continuous transition from $K < J$ to $K > J$. This uncovers the unique feature of van der Waals A-type antiferromagnets, that is the variable spacing between the magnetic layers, similar to artificial antiferromagnets, which allows modification of magnetic properties. As a summary of different magnetic states of $MnBi_2Te_4$ and $MnBi_4Te_7$, a table is shown in Fig. 6.8.

Chapter 7

Model and discussions

$MnBi_2Te_4$ and $MnBi_4Te_7$ have different magnetization behaviors that can be understood with the difference of their interlayer exchange coupling. In this chapter, a modified Stoner-Wohlfarth model is developed for a semi-quantitative description of their different magnetic properties. And it is stressed that at low temperatures, the dominating uniaxial anisotropy over the interlayer antiferromagnetic exchange coupling controls the magnetization switching of $MnBi_4Te_7$ in the weak coupling regime. Therefore, all $[MnBi_2Te_4][Bi_2Te_3]_n$ derivatives with $n \geq 1$ can have metamagnetic behaviors, in striking contrast to $MnBi_2Te_4$.

7.1 Stoner-Wohlfarth model

Before discussing the bi-layer continuous spin model for an interlayer-coupled antiferromagnet, a short review of the Stoner-Wohlfarth model is presented here. This is the simplest model to describe the magnetization of a single domain magnet in presence of a uniaxial anisotropy[133]. In an ideal single domain magnet, since there is no compensation of magnetization from other domains or any other complex magnetic structures such as domain boundaries, the magnetization of the magnet is always uniform. However, the magnetization direction can freely rotate in space. The Stoner-Wohlfarth model considers the total energy as the sum of the Zeeman energy and the uniaxial anisotropy energy, which reads as

$$E = -\mathbf{M} \cdot \mathbf{H} + K \sin^2 \theta, \tag{7.1}$$

where $\mathbf{M}$ is the magnetization, $\mathbf{H}$ is the applied external magnetic field, K is the anisotropy constant, θ is the angle between the magnetization direction and the easy axis and for convenience $\mu_0 = 1$. Since the magnetic moment $\mathbf{M}$ is only a factor before the applied field H, for the convenience of later discussion, we let $|\mathbf{M}| = 1$. The angle between the applied field and the easy axis is defined here as θ_H, so the Zeeman energy can be written as $-H\cos(\theta - \theta_H)$. The energy landscape for different fields applied along the easy axis is shown in Fig. 7.1(a). As one can see, as the applied field increases, the Zeeman energy lowers one local minima while it is lifting up the other local minima until this minima disappears. At zero temperature, the system stays at one local energy minima as long as the Zeeman energy is not enough to compensate the anisotropy barrier. The Zeeman energy required to overcome the energy barrier between two local minima corresponds to the field at which the magnetization switches. A larger anisotropy barrier therefore gives a larger coercive field. For $\theta_H \neq 90°$, the switching and back-switching of the magnetization happened at different magnetic fields, which is also known as magnetic hysteresis. The magnetic hysteresis loops for different θ_H are shown in Fig. 7.1(b).

At the field where the magnetization switches, the stability of the system changes. The switching field fulfills

$$\frac{\partial E}{\partial \theta} = 0, \ \frac{\partial^2 E}{\partial \theta^2} = 0. \tag{7.2}$$

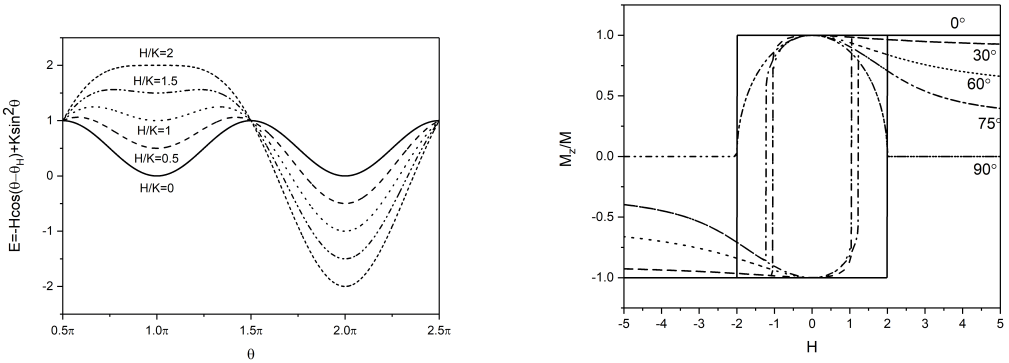

(a) **(b)**

Figure 7.1: (a) The energy landscape of a uniaxial ferromagnet for different applied field H/K along the easy axis. (b) Magnetization curves for different θ_H. The easy axis along the z axis is assumed and only the magnetization along the z axis is shown here.

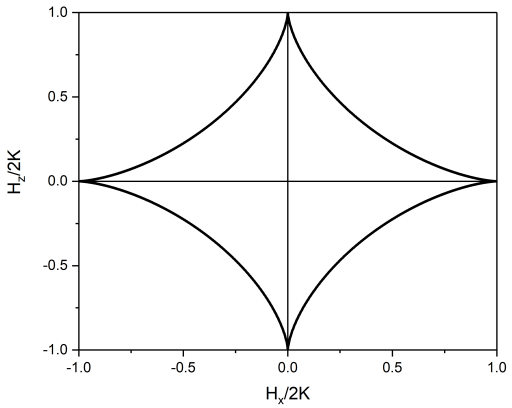

Figure 7.2: The Stoner-Wohlfarth astroid.

Then we have

$$H_z \sin\theta - H_x \cos\theta + 2K \sin\theta \cos\theta = 0, \tag{7.3}$$

$$H_z \cos\theta + H_x \sin\theta + 2K(\cos^2\theta - \sin^2\theta) = 0. \tag{7.4}$$

where $H\cos\theta = H_z$, $H\sin\theta = H_x$. To solve the equations, we can simply rewrite the them as

$$\frac{H_z}{\cos\theta} - \frac{H_x}{\sin\theta} + 2K = 0, \tag{7.5}$$

$$\frac{H_z}{\sin^2\theta\cos\theta} + \frac{H_x}{\sin\theta\cos^2\theta} + 2K\left(\frac{1}{\sin^2\theta} - \frac{1}{\cos^2\theta}\right) = 0. \tag{7.6}$$

Then one can obtain

$$H_z = -2K\cos^3\theta,\ H_x = 2K\sin^3\theta, \tag{7.7}$$

or

$$\left(\frac{H_z}{2K}\right)^{2/3} + \left(\frac{H_x}{2K}\right)^{2/3} = 1. \tag{7.8}$$

By plotting H_z versus H_x, one can obtain the so-called Stoner-Wohlfarth astroid (Fig. 7.2). The astroid indicates the field at which the magnetization switches. Inside the astroid, the magnet has two possible meta-stable states, with magnetization parallel or anti-parallel to the z-axis. Outside the astroid, the magnetization is saturated in the direction at which the field is applied, with the free energy in the stable ground state.

This model of a single-domain magnet may fail to describe the physical properties of a bulk magnet in reality since magnetic domains can form inside the magnet to reduce the magnetostatic energy. The magnetization reversal of a real magnet, instead of being an abrupt transition at a certain field, will be relatively smooth and results for the nucleation and propagation of magnetic domain walls instead of a coherent rotation of a single domain. Generally speaking, there are two types of magnetization mechanisms: propagation of pinned domains and nucleation of magnetic domains. Both of them proceed with increasing magnetic field.

7.2 The bilayer model

The $[MnBi_2Te_4][Bi_2Te_3]_n$ has antiferromagnetic interlayer coupling and ferromagnetic intralayer coupling. The simplest way to describe its magnetic state is to consider a bi-layer model by extending the Stoner-Wohlfarth model under the assumption that each of the two ferromagnetic layers is a single-domain magnet[134]. The effective colinear exchange interaction can be written as $2J\mathbf{M}_1 \cdot \mathbf{M}_2$, where $\mathbf{M}_1$, $\mathbf{M}_2$ are the magnetization of the two layers respectively, and J is the effective exchange interaction constant. The coupling constant J is positive for an antiferromagnetic exchange interaction. The total energy of the system reads as

$$E_2 = -H[\cos(\theta_1 - \theta_H) + \cos(\theta_2 - \theta_H)] + K(\sin^2\theta_1 + \sin^2\theta_2) + J\cos(\theta_1 - \theta_2), \tag{7.9}$$

where $|\mathbf{M}_1| = |\mathbf{M}_2| = 1$ is applied. Let us first consider a typical antiferromagnet that has $J \gg K$. The energy landscape E_2 is shown in Fig. 7.3. At zero field, the minima will only give compensated states where the magnetizations are antiparallel and colinear to the easy anisotropy axis. As the applied field along the easy axis increases, the Zeeman energy will lift the energy levels of those antiparallel spin states and develop another energy minima where $\theta_1 = -\theta_2 \neq 0$. The latter is known as the canted antiferromagnetic state. The transition between the canted states and the antiparallel states is called a spin-flop transition. In canted states, a finite magnetization along the easy axis arises, but the net magnetization perpendicular to the easy axis remains zero. As the field further increases, the magnetization of the two layers experiences coherent rotation to the saturated state where the magnetization of the layers aligns along the applied field. At zero temperature, the system is always trapped at the local minima. Therefore, there will be magnetic hysteresis between the field-increasing magnetization and the field-decreasing magnetization. This is sketched at the bottom part of Fig. 7.3.

The magnetization behaviors can be different when K and J compete each other. To better understand this evolution, the knowledge of the switching fields is required. At transition fields, E_2 fulfills

$$\frac{\partial E_2}{\partial \theta_1} = \frac{\partial E_2}{\partial \theta_2} = 0, \tag{7.10}$$

$$\frac{\partial^2 E_2}{\partial {\theta_1}^2}\frac{\partial^2 E_2}{\partial {\theta_2}^2} - \left(\frac{\partial^2 E_2}{\partial \theta_1 \partial \theta_2}\right)^2 = 0. \tag{7.11}$$

For $\theta_H = 0$, there are three distinct transition fields:

$$H_{\mathrm{sat}} = 2J - 2K, \tag{7.12}$$

$$H_{\mathrm{sf1}} = (2J - 2K)\sqrt{\frac{K}{J+K}}, \tag{7.13}$$

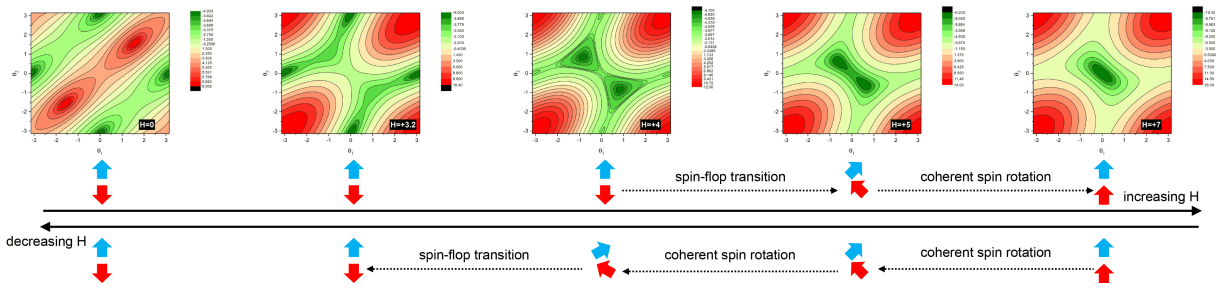

Figure 7.3: The energy landscape E_2 at different applied field H ($K = 1$, $J = 4$). The green colour and the red colour indicate the low and high energy levels respectively. The colour scale is carefully tuned to clarify the positions of these minima and maxima and it is not linearly scaled, so the density of the contour lines does not necessarily represent the energy gradient. On the bottom there show one of the scenarios how the magnetization of the two layers evolve with increasing and decreasing field.

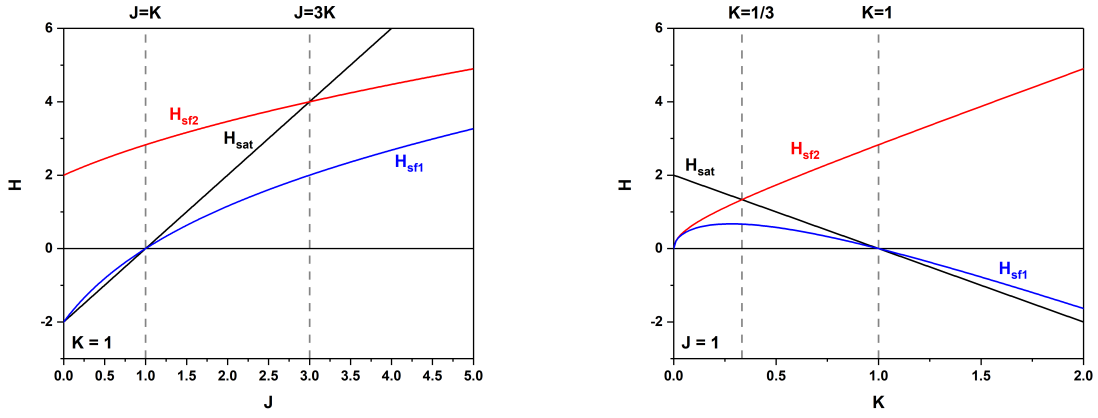

(a) **(b)**

Figure 7.4: (a) The transition fields as a function of the exchange coupling J with fixed $K = 1$. (b) The transition fields as a function of the exchange coupling K with fixed $J = 1$.

$$H_{\mathrm{sf2}} = 2\sqrt{K(J+K)}, \tag{7.14}$$

where H_{sat} is related to the saturation of magnetization along the z axis (the easy axis), since it corresponds to $\theta_1 = \theta_2 = 0(\pm\pi)$, and H_{sf1}, H_{sf2} are related to the spin-flop transitions, as they correspond to $\theta_1 = -\theta_2$. The transition fields as functions of K and J are shown in Fig. 7.4. A typical antiferromagnet has $H_{\mathrm{sat}} > H_{\mathrm{sf2}} > H_{\mathrm{sf1}}$, and it lies in the region where $K/J < 1/3$, as considered in Fig. 7.3. The magnetic hysteresis of the antiferromagnet occurs between the two spin-flop fields H_{sf1} and H_{sf2}. For an intermediate K/J ratio between 1/3 and 1, $H_{\mathrm{sf2}} > H_{\mathrm{sat}} > H_{\mathrm{sf1}}$. A saturated state is possible between the spin-flop fields. When K is larger than J, H_{sat} and H_{sf1} switch signs. It means for $K/J > 1$, the system can have a fully-saturated spontaneous magnetization along the easy axis. Therefore, the crossing of $K/J = 1$ leads to a transition to a meta-magnetic state.

Fig. 7.5 shows the typical magnetization curves for different K/J ratios. The curves were obtained from numerical calculation using the gradient descent method (see Appendix). As mentioned, the model gives some magnetic hysteresis in all cases. For $K/J < 1$, the magnetic bilayer behaves as a typical antiferromagnet, with compensated magnetization at zero field and hysteresis at the spin-flop transitions only. While for $K/J > 1$, although $J > 0$ favors the antiferromagnetic

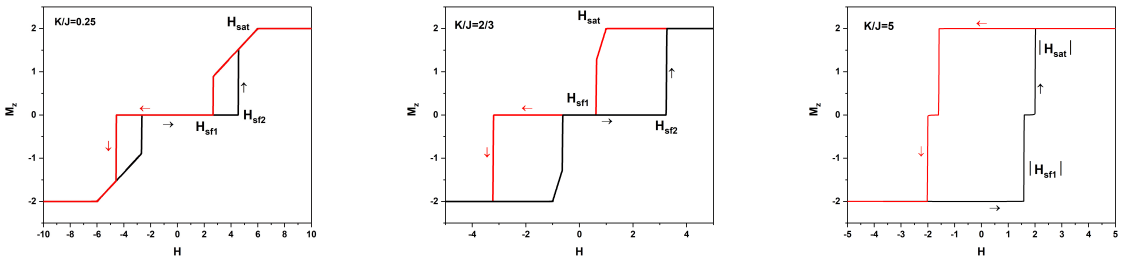

(a) **(b)** **(c)**

Figure 7.5: Typical magnetization curves for three different cases: (a) $K/J < 1/3$, (b) $1/3 < K/J < 1$, (c) $K/J > 1$. For simplicity, in the calculation $K = 1$ was used and J was changed accordingly.

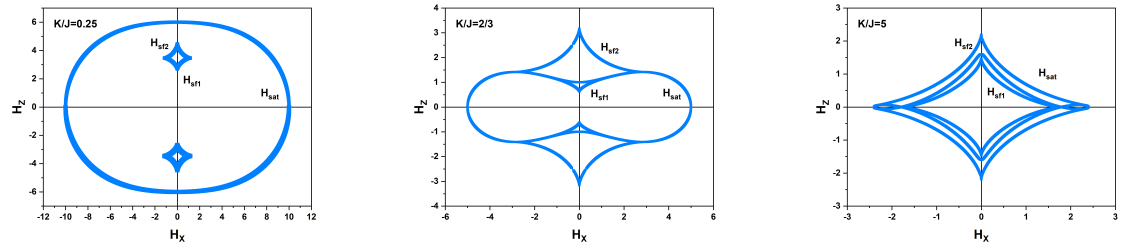

(a) **(b)** **(c)**

Figure 7.6: $H_z - H_x$ diagram for three different cases.

coupling, the bilayer behaves similar to a typical ferromagnet. The reversal of the magnetization proceeds in two steps. For each step, the magnetization of one of the layers reverses.

Bogdanov *et al.* [17] as well as Rohrer and Thomas [135] have previously mapped the phase diagram in the H_z-H_x plane for antiferromagnets having exchange energy much larger than anisotropy energy. Here numerical calculation is performed to complete the mapping for exchange energy close to anisotropy energy. The H_z-H_x phase diagrams are shown in Fig. 7.6. For $K/J < 1/3$, the results are consistent with the previous study. Two separate astroids indicating the hysteresis windows open in the $H_z > 0$ and $H_x < 0$ region. For such small K/J values, the size of the two windows is small, limiting the spin-flop transitions to only small field angles. For magnetic field outside the two windows, the magnetic moments rotate coherently. The saturation limit forms a circle, reachable for any angles. For intermediate K/J values between 1/3 and 1, the size of the two astroids becomes larger or closer to the original point. Therefore, the spin-flop transitions can be observed at larger field angles. The saturation limit circle is further distorted to a spindle. Nevertheless, with increasing field angles, the saturation field still monotonously increases.

As the K/J further increases to values larger than 1, a transition occurs, and in the H_z-H_x diagram, embedded astroids are formed. The astroids indicate the H_{sf1} limit, the H_{sat} limit and the H_{sf2} limit respectively. The case is similar to that of the Stoner-Wohlfarth astroid. The magnetic transitions and non-zero remanent magnetization are achievable at any field angle except for 90°, for which only a coherent rotation occurs. The transition fields will first decrease and then increase with increasing field angles. As one can imagine, a further increase of K or decrease of J will merge all three astroids into a single astroid and a square-like hysteresis loop is obtained.

7.3 Multilayers

The model can be extended for multilayer systems with $N > 2$. The total energy is

$$E_N = \sum_{i=1}^{N}[-\mu_0 M_s H\cos(\theta_i - \theta_H) + K\sin^2\theta_i] + \sum_{i=1}^{N-1} J\cos(\theta_{i+1} - \theta_i), \tag{7.15}$$

and at the field of transitions

$$\frac{\partial E}{\partial \theta_i} = 0, \tag{7.16}$$

$$\det\left(\frac{\partial^2 E}{\partial\theta_i \partial\theta_j}\right) = 0. \tag{7.17}$$

In order to capture the main characteristics of the magnetization process of such systems, we focus on $\theta = 0$ cases only. The hysteresis loops for different layers and K/J ratios are shown in Fig. 7.7. For multilayer systems, the K/J ratio will still play an important role in the magnetization behaviors of the system. Those with $K/J < 1$ still show spin-flop transitions while those with $K/J > 1$ have ferromagnetic-like hysteresis loops.

On one hand, strong layer dependence has been identified for small K/J (Fig. 7.7 (a)-(e)). For even-numbered layers, the hysteresis loops are similar to the bilayer case. However, for odd-numbered layers, uncompensated magnetization occurs at zero field, with the magnetization of each layer being antiparallel to that of its neighboring layer. When one increases the field, all the layers will flip their magnetization so that the Néel vector is reversed. With further increase of magnetic field, spin-flop transitions occur. The insets of Fig. 7.7 demonstrate how θ_i evolve with increasing magnetic field from low field to large positive fields. It can be noticed that the canting angles of the intermediate layers are larger than those of the layers on surfaces. If the number of layers is increased, the saturation will be more difficult to reach. For odd-numbered layers, the magnetization remanence, which is the uncompensated magnetization, will be the magnetization of a single layer regardless of the total number of layers. The calculation results obtained here are comparable with the layer-dependent properties of $MnBi_2Te_4$ shown in Fig. 3.10a.

On the other hand, for layers with $K/J > 1$, the hysteresis loops are similar for different layers (Fig. 7.7 (f)-(j)). The onset and saturation fields are also close to those in the bilayer case. As the layer number increases, the magnetization steps increase. Layer-by-layer spin-flip transitions occur at each step, which are shown by the schematics in the figure. The layers in the middle would preferably experience the reversal before the layers close to surfaces.

For intermediate K/J values, the system behaves like a combination of two aforementioned cases (Fig. 7.7 (k)-(o)). The odd layered systems have non-zero remanence while even-numbered layers have compensated magnetic structures at zero field. The magnetization processes of such systems are sequential layer-by-layer flipping transitions, but the onsets of these transitions do not necessarily require to reverse the magnetic field. When there is a spin canting, the canting angles of outer layers are still smaller than the canting angles of inner layers.

For large N values as in the bulk materials, it is expected that the situation is similar to the results for $N = 15$, but it will also be similar to the $N = 2$ case since bulk antiferromagnets are typically compensated antiferromagnets. Recall that this model is a zero-temperature model. The small magnetization steps are very likely to be smoothed out by thermal effects in reality, although this depends on the height of the anisotropy energy barrier. Meanwhile, the switching field can be reduced as discussed in the following section.

7.4 Comparison with experimental data

The magnetic properties of both $MnBi_2Te_4$ and $MnBi_4Te_7$ are well captured by the bilayer model. Importantly, it reveals that the K/J ratio plays an important role in determining the magnetic

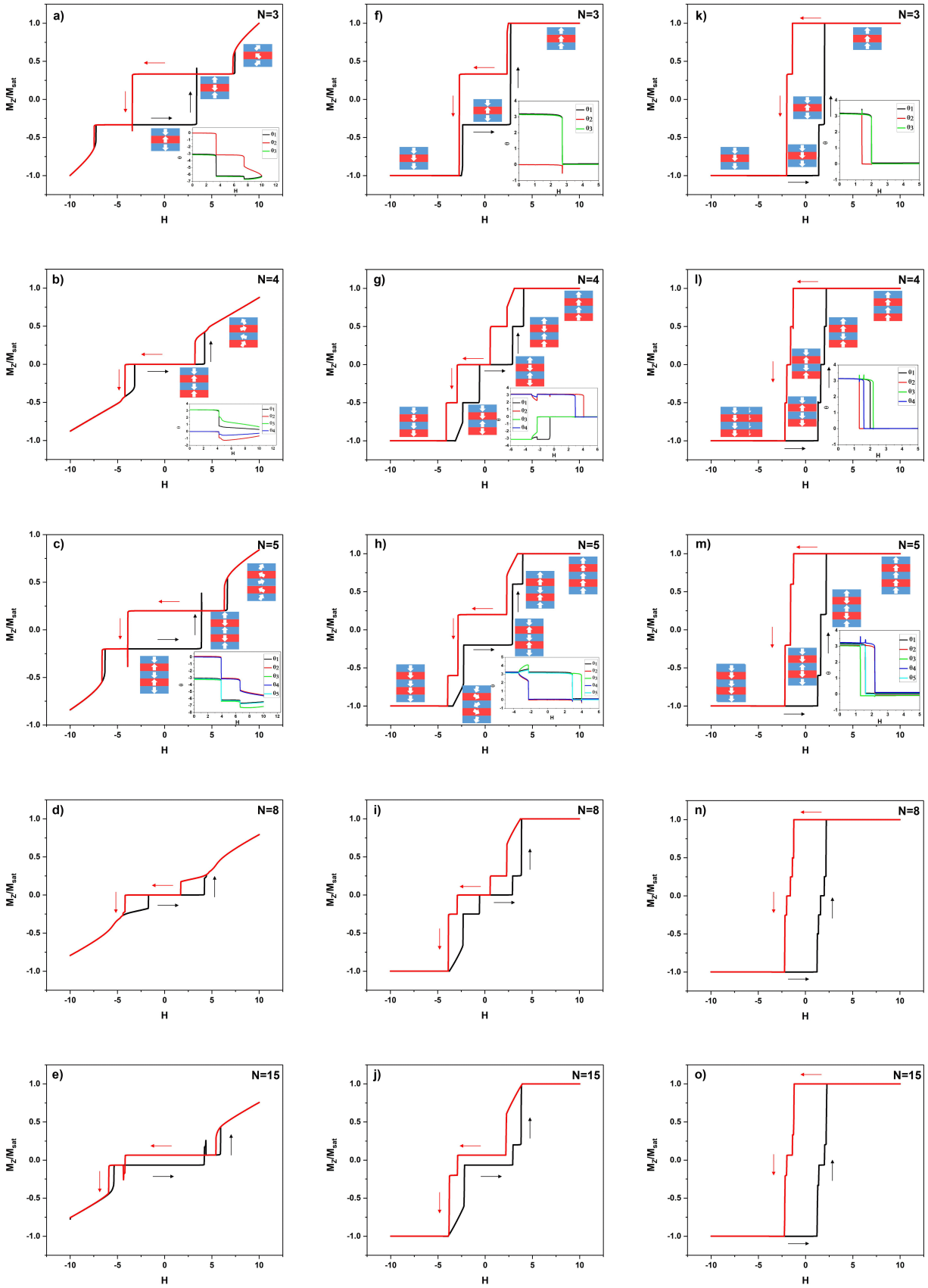

Figure 7.7: The hysteresis loops for different layers and K/J ratios. (a)-(e) $K = 1, J = 4$, (f)-(j) $K = 1, J = 1.5$, (k)-(o) $K = 1, J = 0.2$.

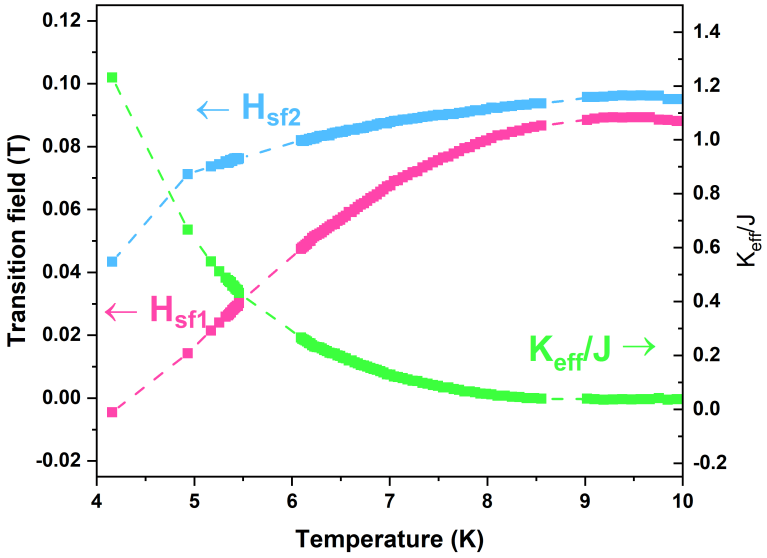

Figure 7.8: Temperature dependence of spin-flop transition fields and the ratio between effective anisotropy and exchange coupling.

state of antiferromagnetically coupled layers (bilayers and multilayers). $MnBi_2Te_4$ shows the typical behavior of an A-type antiferromagnet below the Néel temperature. It has a relatively large spin-flop field and a large canting after the spin-flop transition, which suggests the relatively large interlayer exchange coupling and a small K/J ratio. Regardless of the temperature evolution of the spin-flop field, the overall magnetic behavior of $MnBi_2Te_4$ does not change with the temperature. It implies that the interlayer exchange coupling in $MnBi_2Te_4$ is strong enough and that the temperature evolution of magnetic anisotropy is not sufficient to change significantly the K/J ratio.

The case is different for $MnBi_4Te_7$ due to the weakened exchange coupling by the non-magnetic Bi_2Te_3 spacer. Below the Néel temperature and above the blocking temperature T_B, the magnetic behavior is similar to that of $MnBi_2Te_4$. The magnetization process is accompanied by spin-flop transitions and coherent rotations in the canted states. However, the spin-flop field is much lower and the saturation is reached shortly after the spin-flop transition. This confirms the weakly coupled nature of $MnBi_4Te_7$, and also that the anisotropy is large enough to have a rather limited canting between successive sub-layer magnetizations. Since the effective anisotropy is proportional to the thermal average of saturated magnetization $\langle M_S^2 \rangle$, the effective anisotropy can increase with $\langle M_S^2 \rangle$ as the temperature decreases. As a consequence, K/J can change from smaller than 1 at a temperature $T_B < T < T_N$ to larger than 1 at lower temperatures. Contrary to the situation of $MnBi_2Te_4$, a large magnetic hysteresis develops and a fully-aligned remanent state is obtained below T_B. It is important to recall that the magnetic state realized in $MnBi_4Te_7$ below T_B is a meta-magnetic state, stabilized by the large anisotropy energy barrier. Although it results in magnetization curves that resemble those of ferromagnets, there is no ferromagnetic interlayer exchange coupling.

By using the bilayer model, one can estimate the K/J for $MnBi_2Te_4$ and $MnBi_4Te_7$. For $J \gg K$, eqn. 7.13 and eqn. 7.14 become

$$H_{sf1} = \sqrt{JK}(2 - 3\frac{K}{J} + \frac{7}{4}\frac{K^2}{J^2} - \frac{11}{8}\frac{K^3}{J^3} + ...) \approx 2\sqrt{JK}, \tag{7.18}$$

$$H_{sf2} = \sqrt{JK}(2 + \frac{K}{J} - \frac{1}{4}\frac{K^2}{J^2} + \frac{1}{8}\frac{K^3}{J^3} + ...) \approx 2\sqrt{JK}, \tag{7.19}$$

which give the same results as previous antiferromagnet model[17]. It implies the hysteresis in a strongly coupled antiferromagnet is small. In the case of $MnBi_2Te_4$, there is no observable hysteresis. One can assign $\mu_0 M_s H_{sf} = 2\sqrt{JK}$ with $\mu_0 H_{sf} = 3.2T$. The K/J ratio can be calculated by

$$\frac{K}{J} = \frac{\sqrt{B_{sat}^2 + 4B_{sf}^2} - B_{sat}}{\sqrt{B_{sat}^2 + 4B_{sf}^2} + B_{sat}}. \tag{7.20}$$

It gives $K/J \approx 0.154$ ($T = 2$K). Alternatively, one can calculate it by

$$\frac{K}{J} = \frac{H_{sat}^{90^\circ} - H_{sat}^{0^\circ}}{H_{sat}^{90^\circ} + H_{sat}^{0^\circ}}, \tag{7.21}$$

where $H_{sat}^{90^\circ} = 2J + 2K$ and $H_{sat}^{0^\circ} = 2J - 2K$ are the in-plane saturation field and the out-of-plane saturation field. The calculation gives $K/J \approx 0.132$ ($T = 2$K). The calculated values correspond well to the strong exchange coupling in $MnBi_2Te_4$.

On the other hand, $MnBi_4Te_7$ has observable spin-flop transition hysteresis. One can make use of it to calculate K/J

$$\frac{K}{J} = \frac{H_{sf2} - H_{sf1}}{H_{sf2} + H_{sf1}}. \tag{7.22}$$

This gives the results shown in Fig. 7.8. The spin-flop transition fields decrease below 10K, but on the other hand, the difference in the two spin-flop transition fields becomes large as temperature decreases. The calculated K_{eff}/J gives small values around 10K. But then it is followed by also a strong increase. This explains the typical A-type antiferromagnetic behavior around the Néel temperature, namely the spin-flop transitions away from zero field without hysteresis. But then the increase of K/J allows hysteresis at a lower temperature. It also shifts the spin-flop transition to lower field and lets it to cross the zero field. At 100mK, where J is intuitively negligible according to the single-domain-like magnetization behaviors, the anisotropy dominates the switching of the magnet and can be estimated by $K = 5\mu_B B_{SW}/2$, where $5\mu_B$ is the magnetic moment of a Mn atom, and B_{SW} is the switching field of the magnet.

Whereas the anisotropy field is well determined from measurements with the magnetic field applied in the sample plane (that is, perpendicular to the easy-anisotropy axis), the angular dependence of the switching field deviates from the Stoner-Wohlfarth astroid for small angles(Fig. 6.7). This is probably related to the existence of magnetic domain walls. In antiferromagnets with a uniaxial anisotropy, domain walls are know to exist in the region of the spin-flop transition[17]. This is also the case for the reversal of the metamagnetic state, yet with properties more similar to the case of a ferromagnet. If the activation volume of a magnetic domain wall is smaller than the sample size, the switching field of the metamagnet can be much reduced as compared to the field predicted by the Stoner-Wohlfarth model. For small angles, the magnetization reversal is due to a process of domain wall nucleation and propagation. Given the crystal quality, it is probable that the switching field is a nucleation field, which is also confirmed by the initial reduction of H_{sw} at small angles. In any case, the propagation of a domain wall becomes more difficult in a tilted field, and this contribution to Hsw varies as $1/\cos\theta$. For large angles, the coherent rotation of magnetic domains dominates and the switching field evolves as calculated for a Stoner-Wohlfarth astroid. Importantly, as found in our experiments, the switching increases to a maximum value, which is the anisotropy field.

In summary, the meta-magnetism of $MnBi_4Te_7$ below T_B arises from its relatively weak interlayer exchange coupling. Contrary to early reports, there is no ferromagnetism in $MnBi_4Te_7$ but a meta-magnetic state that reveal the importance of the perpendicular magnetic anisotropy in these systems (beyond the simple stabilization of the 2D long range order). To evidence chiral

topological phases at higher temperatures, it is important to increase the anisotropy barriers in magnetic topological insulators.

Chapter 8

Conclusions and Perspectives

In this work, the magnetic properties of $MnBi_2Te_4$ and $MnBi_4Te_7$ were investigated with transport measurements. The A-type antiferromagnetism with perpendicular magnetic anisotropy was confirmed in $MnBi_2Te_4$. The relatively large spin-flop transition field and the large spin canting after the spin-flop transition confirm the relatively strong interlayer exchange coupling of the material compared to the uniaxial anisotropy. This is typical for most antiferromagnets. For $MnBi_4Te_7$, due to the large spacing between the magnetic layers, a distinct magnetic behavior is found, typical of weakly-coupled uniaxial antiferromagnets, with a small spin-flop transition field and a small spin canting. The ordering temperature of $MnBi_4Te_7$ is close to the ordering temperature of a single layer of $MnBi_2Te_4$ (12K), which implies that the 2D ferromagnetic nature of isolated $MnBi_2Te_4$ planes can exist in such systems. With the Néel temperature and the Curie-Weiss temperature of the materials, the much weaker interlayer exchange coupling was quantitatively confirmed.

Below the blocking temperature, $MnBi_4Te_7$ showed magnetic hysteresis similar to the one of a ferromagnet, but which is shown to be related to a meta-magnetic state. To understand the uncommon magnetic properties of the material, a bi-layer Stoner-Wohlfarth model was developed. This simple model shows that the K/J ratio plays an important role in determining the magnetic behavior of antiferromagnets with uniaxial magnetic anisotropy. When $K/J \ll 1$, the system has antiferromagnetism similar to $MnBi_2Te_4$. By contrast, $K/J > 1$ allows saturated remanence and magnetic hysteresis similar to that of a ferromagnet. Such meta-magnetism exists when the magnetic anisotropy is larger than the antiferromagnetic coupling. This situation is possible for all $n \geq 1$ members of $[MnBi_2Te_4][Bi_2Te_3]_n$ family due to the non-magnetic Bi_2Te_3 spacers. The increase of effective anisotropy with decreasing temperature gives a temperature evolution of K/J and therefore an evolution from antiferromagnetism to meta-magnetism in such systems. It can be further concluded that $n \geq 1$ members in the $[MnBi_2Te_4][Bi_2Te_3]_n$ family all have similar magnetic properties, for example, magnetic ordering at $\sim$12K and meta-magnetism at low temperature, which has been recently proven[108].

These findings on the magnetic properties of $[MnBi_2Te_4][Bi_2Te_3]_n$ open possibilities to tune their magnetism with different layer stacking manners. Due to the close correlation between magnetic properties and topological properties in these systems, it will also be possible to manipulate the topology of band structures with the obtained knowledge of magnetism.

There are nevertheless open questions about the magnetism of $[MnBi_2Te_4][Bi_2Te_3]_n$, which have not been considered with in this work. $MnBi_2Te_4$ samples with different thicknesses were studied in this work. For structures with thickness $>$ 20nm, the magnetism is similar to the bulk. The study of layer dependence properties requires samples with only a few septuple layers. Furthermore, as the volume of the bulk becomes smaller, the contribution of the surfaces becomes prominent. There could be different magnetic anisotropy at the interfaces, which would modify the magnetism of the nanostructures and therefore affect the manipulation of topological effects. Topological magnetic features, such as skyrmions may also exist in few-layer systems, which have

not been investigated so far. The recent development on the molecular beam epitaxy (MBE) growth of $[MnBi_2Te_4][Bi_2Te_3]_n$ may provide new possibilities for such studies[13]. Not only that the thickness of samples can be well controlled in the growth process, but also that different heterostructures with different n values can be grown. Intercalation with other materials will be also possible. This paves the way for further studies. One of the drawbacks of MBE grown materials may be the existence of terraces. Since $[MnBi_2Te_4][Bi_2Te_3]_n$ are similar to weak topological insulators, they are not robust against surface disorders. The terraces may prevent one from observing interesting topological effects.

Besides the magnetism, the transport properties of $MnBi_2Te_4$ and $MnBi_4Te_7$ were also investigated in this work. The samples measured had large carrier densities similar to disordered Bi_2Te_3 but had much lower electron mobilities, which could be due to the antisite defects. The observation of transport properties of topological surface states was unfortunately hindered by the large contribution of the bulk. Also for this reason, it will be important to obtain nanostructures with low thicknesses. It was also proposed that doping $MnBi_2Te_4$ with Sb allows tuning the Fermi level to the band gap[131]. This creates alternatives to suppress the bulk contribution. However, it was predicted that $MnSb_2Te_4$ has a trivial band gap. Doping with Sb may reduce the size of the surface state band gap, which can cause further difficulties for the observation of the quantum anomalous Hall effect (QAHE) (for example, a lower temperature is required).

Appendix A

Gradient descent

At zero temperature, a physical system tends to stay at the state where the local energy minimum is. Although the gradient descent method has obvious disadvantages for searching for the global minimum, it is an efficient method to find out the local minimum, and hence the stable energy state in the vicinity of the given initial state. As can be inferred by its name, the path of the approaching to the minimum is determined by the gradient of the energy surface. The underlying reason for choosing a such path is that in a first-order approximation, the energy varies fastest at the opposite direction of the gradient, which can be proven as the following. For a function with multi-variables $f(x_1, x_2, ..., x_n)$, we are interested in how to choose the step $(l\delta x_1, l\delta x_2, ..., l\delta x_n) = l\delta\boldsymbol{x}$ so that $\Delta f = f(x_1, x_2, ..., x_n) - f(x_1 + l\delta x_1, x_2 + l\delta x_2, ..., x_n + l\delta x_n)$ become as large as possible. Here, l is the length of the step, x_i can be any parameters such as spatial coordinates, temperature, fields and so on. $\delta\boldsymbol{x}$ is assumed normalized. If l is sufficiently small, we can expand $f(x_1 + l\delta x_1, x_2 + l\delta x_2, ..., x_n + l\delta x_n)$ to the first order

$$\begin{aligned} f(x_1 + l\delta x_1, x_2 + l\delta x_2, ..., x_n + l\delta x_n) &\approx f(x_1, x_2, ..., x_n) + \sum_{i=1}^{n} l\delta x_i \frac{\partial f}{\partial x_i} \\ &= f(x_1, x_2, ..., x_n) + l\delta\boldsymbol{x} \cdot \nabla f \\ &= f(x_1, x_2, ..., x_n) + l|\delta\boldsymbol{x}||\nabla f| \cos\alpha, \end{aligned} \tag{A.1}$$

where $\cos\alpha$ is the angle between $\delta\boldsymbol{x}$ and ∇f. The second has its minimum when $\cos\alpha = -1$, or in other words, $\delta\boldsymbol{x}$ is antiparallel to ∇f. So we can choose

$$\delta\boldsymbol{x} = -\frac{\nabla f}{|\nabla f|}. \tag{A.2}$$

In a simplest calculation, one iterative step of the algorithm gives a new state by adding $l\delta\boldsymbol{x}$ to the initial state, that is $\boldsymbol{x}_{k+1} = \boldsymbol{x}_k - l\nabla f_k/|\nabla f_k|$. A sufficient large number of iterative steps will allow the system to find the local minimum.

Appendix B

Temperature dependence of resistance of Cernox

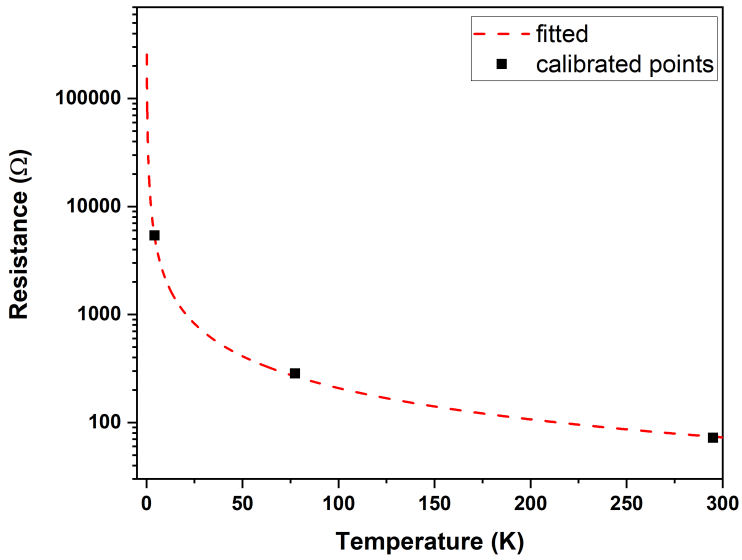

Figure B.1: The temperature dependence of resistance of Cernox CX-1050 used in this work. The black squares are calibrated points. The red dashed line is the fitting result.

The temperature dependence of the resistance of a Cernox censor can be approximated by the Chebyshev polynomials

$$\lg T_{\text{temp}} = \frac{a_0}{2} + \sum_{n=1}^{\infty} a_n T_n(x), \tag{B.1}$$

where

$$x = \frac{(Z - Z_U) + (Z - Z_L)}{Z_U - Z_L}, \; Z = \lg R. \tag{B.2}$$

Here, R is the resistance of the Cernox censor, T_{temp} is the temperature, Z_U and Z_L are the upper

and lower limit of Z respectively. The first orders of Chebyshev polynomials are shown below

$$\begin{aligned} T_1 &= x, \\ T_2 &= 2x^2 - 1, \\ T_3 &= 4x^3 - 3x, \\ T_4 &= 8x^4 - 8x^2 + 1, \\ T_5 &= 16x^5 - 20x^3 + 5x. \end{aligned} \tag{B.3}$$

Fig. B.1 shows the result of fitting the resistance of Cernox CX-1050 as a function of temperature.

Appendix C

Supplementary results

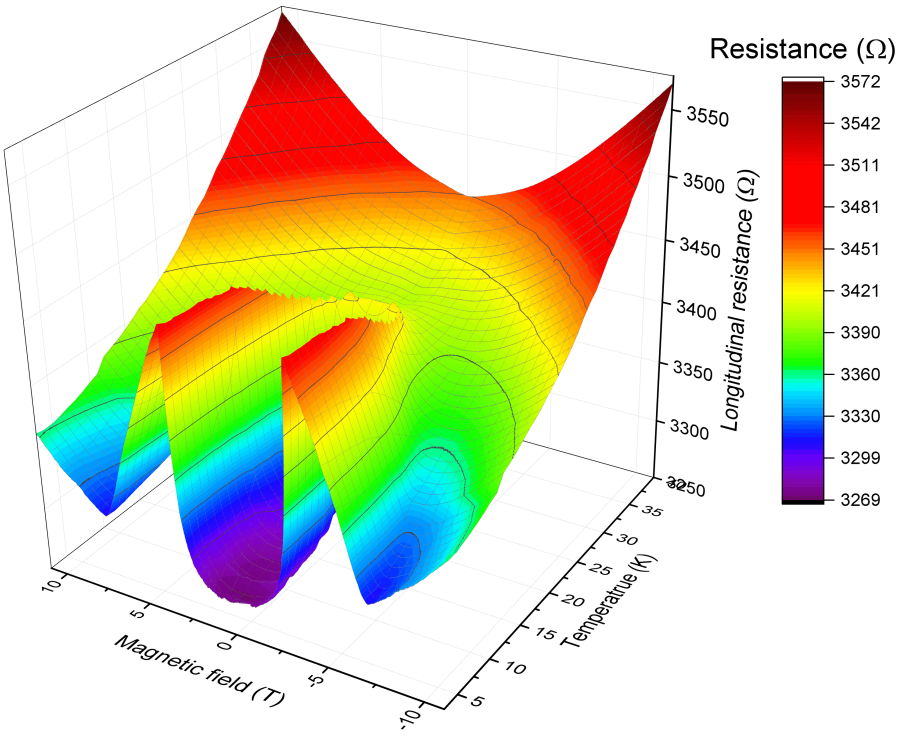

Figure C.1: The longitudinal resistance of $MnBi_2Te_4$ (sample ATMBT13) as a function of the magnetic field and the temperature plotted in a 3D space.

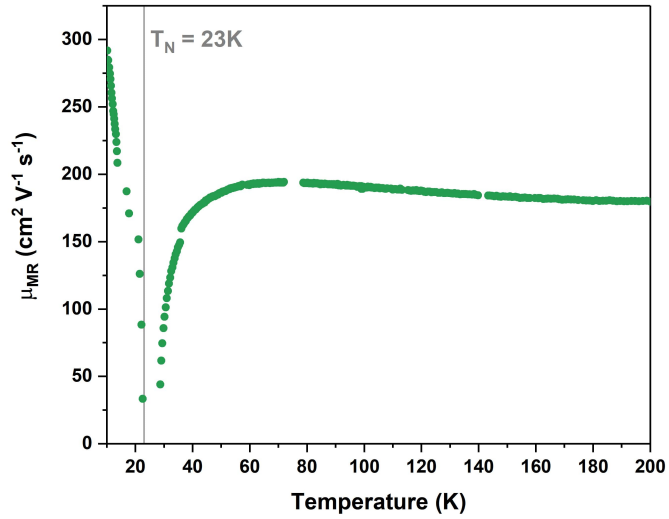

Figure C.2: The carrier mobility of $MnBi_2Te_4$ (sample ATMBT13) extracted with the magnetoresistivity. Here, only the background due to the geometric magnetoresistivity is considered (a magnetic field range with $|B| > 5$T or $|B| < 0.5$T, so that details of spin-flop transitions are avoided). The magnetoresistivity was fitted with $\rho_{xx}(B)/\rho_{xx}(0) = 1 + \mu_{\mathrm{MR}}^2 B^2$, hence the mobility. The order of magnitude of the mobility is comparable with that shown in Fig. 5.6. However, a strong decrease near the Néel temperature is shown here, which can be due to enhanced spin fluctuation.

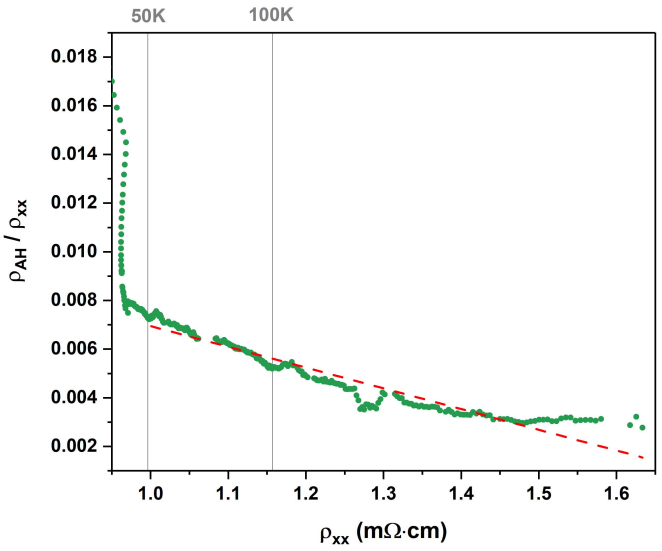

Figure C.3: The scaled anomalous Hall resistivity $\rho_{\mathrm{AH}}/\rho_{xx}$ of $MnBi_2Te_4$ (sample ATMBT13) as a function of longitudinal resistivity ρ_{xx}. The red dashed line depicted the linear fit above 50K as a guide to the eye.

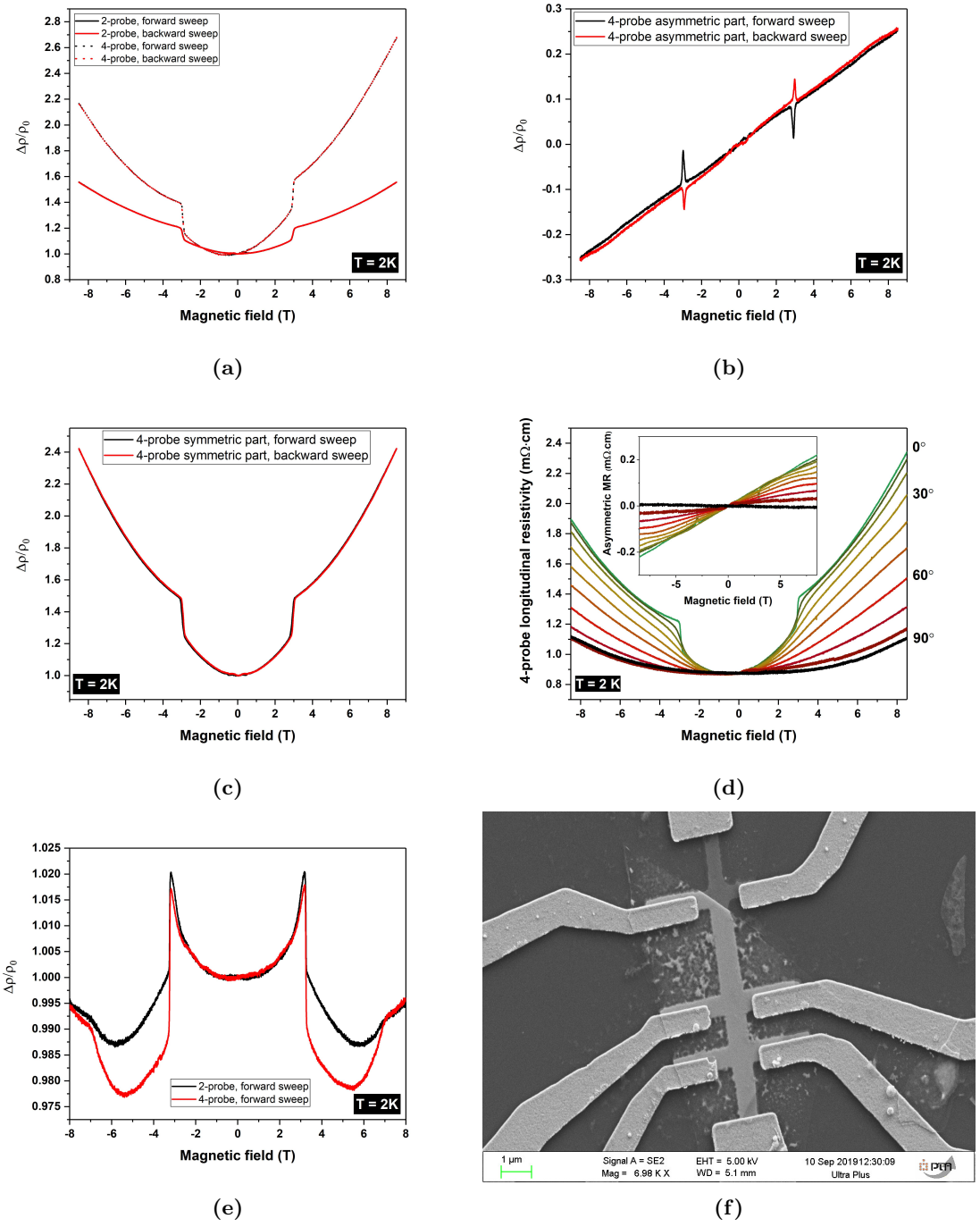

Figure C.4: Comparison of 2-probe and 4-probe magnetoresistivity. In this work, sample ATMBT2, ATMBT4 and ATMBT5 were not patterned as Hall bars. The measurement results shown in the text for these samples were measured with 2-probe configuration to exclude the Hall contribution. As shown in (a) the uncorrected 4-probe longitudinal resistivity compared with the 2-probe longitudinal resistivity, the 4-probe results have additional linear background, which can be further confirmed by separating (b) the asymmetric component and (c) the symmetric component of the magnetoresistivity (sample ATMBT2). One can carefully examine that the asymmetric component is due to the Hall contribution with (d) the angular dependence results. As the field angle increases, the asymmetric component vanished (inset in (d)), which proves the Hall contribution. With patterned Hall geometry, the linear Hall background can be significantly smaller as shown in (e) (sample ATMBT7). The SEM image of the patterned device is shown in (f).

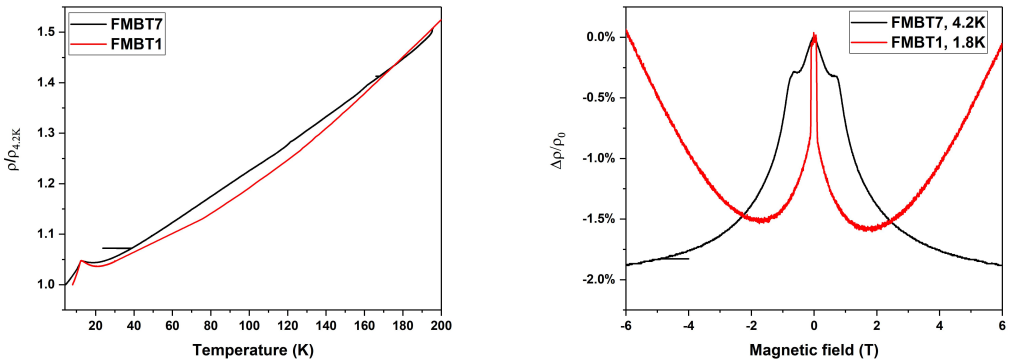

(a) **(b)**

Figure C.5: (a) The rescaled resistivity $\rho/\rho_{4.2\mathrm{K}}$ as a function of temperature for the sample FMBT1 and FMBT7. (b) The magnetoresistivity of the two $MnBi_4Te_7$ samples up to 6T.

Sample	Resistivity ($m\Omega\cdot cm$)	Mobility ($cm\cdot V^{-1}s^{-1}$)	Carrier density (cm^{-3})	Thickness (nm)
FMBT1 (1.8K)	0.0572±0.0024	713±34	$1.52(9) \pm 0.034 \times 10^{20}$	90±2
FMBT7 (4.2K)	0.347±0.018	1.55±0.10	$1.16 \pm 0.05 \times 10^{22}$	43±2

Table C.1: Summary of main physical parameters of $MnBi_4Te_7$ nanostructures studied in this work.

Appendix D

Limitations of the bi-layer Stoner-Wohlfarth model

The previously discussed model applies well in single-domain magnets, such as particle magnets with typical dimensions comparable to the size of domains. In those cases, the magnetic moments experience only coherent rotation in the magnetization process. However, in extended magnetic systems, magnetic domains can form. Two mechanisms instead can contribute to the magnetization process: domain nucleation and wall propagation. Magnetic domains can start to nucleate at a field much smaller than the value suggested by the Stoner-Wohlfarth model $2K/\mu_0 M_s - N_{\text{eff}} M_s$, which is known as the Brown's paradox. This can be attributed to the magnetic defects or minor magnetic modes which reduce the effective magnetic anisotropy. Kronmüller formulated the nucleation field by adding a factor[136]

$$H_N = \frac{2K}{\mu_0 M_s}\alpha - N_{\text{eff}} M_s. \tag{D.1}$$

The nucleated domains can then expand through the propagation of domain walls. However, the process will be hindered by disorders, which is also known as the pinning of domain walls. The disorders can be characterized by a potential barrier, the crossing of which can be achieved by gaining Zeeman energy or thermal activation.

At finite temperature, the time for magnetization reversal by thermal activation is

$$\tau = \tau_0 \exp(\Delta E/k_B T), \tag{D.2}$$

where τ_0 is typically 10^{-11}s, and in the proper time of a measurement ($t \sim 1$s), the energy barrier is approximately $E_0 - k_B T \ln t/\tau_0 \approx E_0 - 25 k_B T$[140]. Hence, the magnetization reverses when $-v\mu_0 M_s H \cos\theta_H = E_0 - 25 k_B T$, where v is the volume. The switching field here follows the $1/\cos\theta_H$ law

$$H_{\text{SW}} = -\frac{E_0 - 25 k_B T}{v\mu_0 M_s \cos\theta_H}. \tag{D.3}$$

For sintered magnets, the grains are not all aligned. The angle between the grains and the z axis has a broadened distribution, which is described as Gaussian type in Givord's formulation[141]

$$p(\theta_{gz}) = \frac{1}{\sigma}\sqrt{\frac{2}{\pi}} \exp -\frac{\theta_{gz}^2}{2\sigma^2}. \tag{D.4}$$

In high-quality crystals (single crystals), we can assume σ is small and the angular dependence of H_{SW} deviates barely from the $1/\cos\theta_H$ law.

It is important to be reminded that at finite temperature both nucleation of domains and wall propagation are dynamical processes. The switching field of an extended magnetic system depends

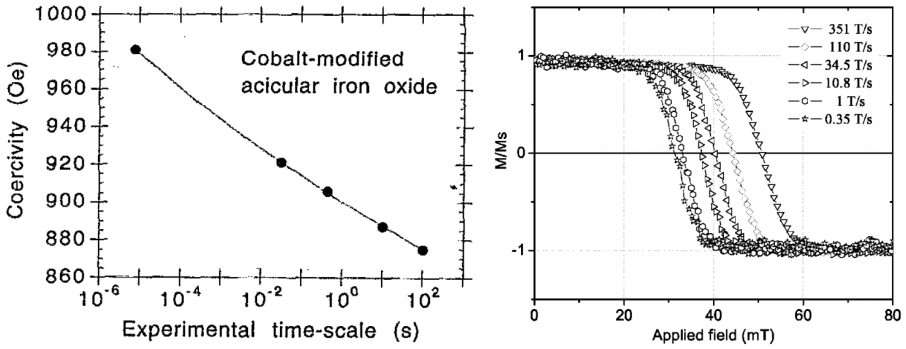

(a) (b)

Figure D.1: (a) The coercivity of acicular cobalt-modified iron oxide particles as a function of experimental time scale.[137] (b) The magnetization curves for different field sweep rates on an array of $100 \times 100\text{nm}^2$ magnetic dots.).[138]

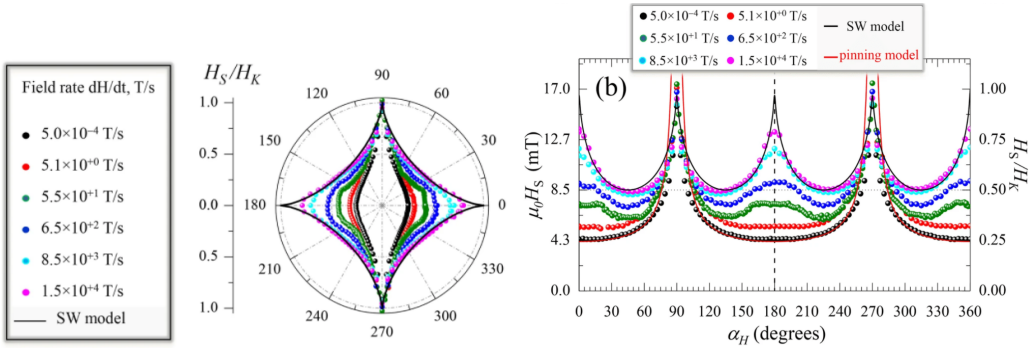

(a) (b)

Figure D.2: (a) and (b) The angular dependence of the switching field of Co thin films for different field sweep rate.[139]

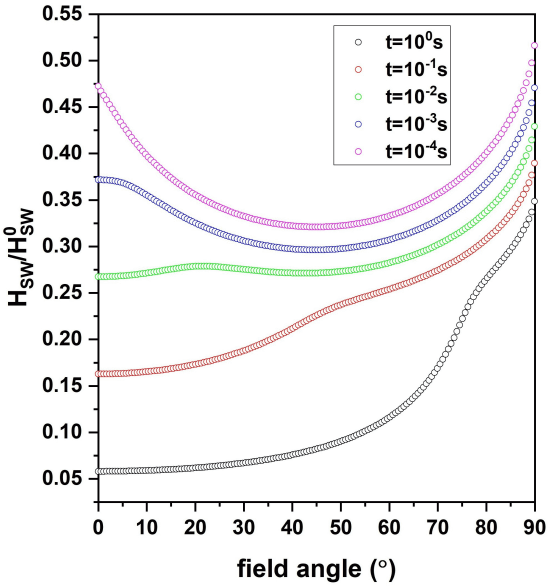

Figure D.3: Calculation results of the angular dependence of the switching field H_0/H^0_{SW} for different measurement time scale t.

on the nucleation rate and the propagation dynamics. As a consequence, the switching field is not an intrinsic physical quantity of a magnetic system, but depends on the field sweep rate and the temperature. Experimental evidence of the time dependence switching field is shown in Fig. D.1. In addition, the sweep rate has also an influence on the angular dependence of the switching field[139]. It is shown that the increase of sweep rate changes the angular dependence from the propagation-limited $1/\cos\theta_H$ dependence to the nucleation-limited Stoner-Wohlfarth-like angular dependence (Fig. D.2a and D.2b). This implies that in a fast sweep measurement, the nucleation contribution takes place of the wall propagation contribution and dominates the magnetization process. And when the nucleation dominates, the Stoner-Wohlfarth angular dependence recovers. It was also evidenced that by Olivier Fruchart *et al.* in epitaxial dots when the nucleation dominates, the angular dependence of switching field is close to a Stoner-Wohlfarth astroid[142].

By following the model discussed by Sharrock in [137], a simple model that describes the evolution of angular dependence can be developed. According to [137], the probability of per unit time of successful barrier crossing or the rate constant is

$$r = A\exp(-\Delta E/k_BT), \tag{D.5}$$

which is equivalent to the description of eqn. D.2. The magnetization changes with time as

$$M(t) = M_s(1-2e^{-rt}). \tag{D.6}$$

Here we define a successful magnetization reversal takes place when $rt \sim 1$. And the rate should include the contribution from domain nucleation and the contribution from wall propagation $r = r_\mathrm{n} + r_\mathrm{p}$. For preliminary discussion, the two contributions are considered independent here. The nucleation requires the crossing of an energy barrier described by the Stoner-Wohlfarth model, by using the Pfeiffer approximation

$$r_\mathrm{n} = A_\mathrm{n}\exp(-\Delta E_\mathrm{n}/k_BT), \tag{D.7}$$

$$\Delta E_\mathrm{n} = KV(1-H/H_0^\mathrm{n})^m, \tag{D.8}$$

where

$$H_0^\mathrm{n} = 2xK/M_s,\ m \approx 0.86 + 1.14x, \tag{D.9}$$

and x here is giving the angular dependence of the Stoner-Wohlfarth model

$$x = [\cos^{2/3}\theta_H + \sin^{2/3}\theta_H]^{-3/2}. \tag{D.10}$$

If only the nucleation contribution ($rt = r_\mathrm{n}t = 1$) is considered, we end up with the same result as in [137]

$$H_\mathrm{SW} = H_0^\mathrm{n}\{1-[(k_BT/KV)\ln(A_\mathrm{n}t)]^{1/m}\}. \tag{D.11}$$

For acicular Co-Fe oxide $1/m$ was reported to be 1.115-0.0606[$\log(A/\mathrm{s}^{-1})$][137]. The propagation requires the depinning of domain walls. This takes place when a pinning potential E_0 is overcome. In fact, the well-known droplet theory is giving the expression of the energy barrier E_0 for magnetic thin films. In other words, in stead of an energy barrier $E_0 - v\mu_0M_sH$, an energy barrier $2\pi rt(\gamma - r\mu_0M_sH)$ is given[143]. Without loss of generality, here we neglect the details of the energy barrier and write it as

$$\Delta E_\mathrm{p} = \varepsilon\left(1-\frac{H}{H_0^\mathrm{p}}\cos\theta_H\right), \tag{D.12}$$

with the rate constant

$$r_\mathrm{p} = A_\mathrm{p}\exp(-\Delta E_\mathrm{p}/k_BT), \tag{D.13}$$

Similar to eqn.D.11, if only the propagation contribution ($rt = r_{\mathrm{p}}t = 1$) is considered

$$H_{\mathrm{SW}} = \frac{H_0^{\mathrm{p}}}{\cos\theta_H}[1 - (k_BT/\varepsilon)\ln(A_{\mathrm{p}}t)]. \tag{D.14}$$

When both contributions are taken into account, $r_pt + r_nt = 1$, where independent contribution of nucleation and propagation is considered. For the ease of calculation and discussion, here we let $A_n = A_p = 10^9\ \mathrm{s}^{-1}$, $KV = 50k_BT$, $\varepsilon = 22k_BT$, $H_0^{\mathrm{n}} = H_0^{\mathrm{p}} = H_{\mathrm{SW}}^0$. The calculation result is shown in Fig. D.3. The evolution from the $1/\cos\theta_H$ law to Stoner-Wohlfarth-like angular dependence is reproduced as the measurement time scale t is reduced. The relatively weak t-dependence for large field angles, which was another consequence of this is that the field required for crossing the propagation energy barrier increases faster than the field for crossing the nucleation energy barrier as the sweep rate increases. In this case, the nucleation contribution would be possible to dominate the magnetization process. The finding is important to spintronics applications since fast writing speed is of interest. However, the writing speed will have an effect on the writing field and the angular dependence of the writing field.

List of Figures

Bibliography

[1] Q. He, L. Pan, A. L. Stern, E. C. Burks, X. Che, G. Yin, J. Wang, B. Lian, Q. Zhou, E. S. Choi, K. Murata, X. Kou, Z. Chen, T. Nie, Q. Shao, Y. Fan, S. Zhang, K. Liu, J. Xia, and K. L. Wang. Chiral Majorana fermion modes in a quantum anomalous Hall insulator–superconductor structure. *Science*, 357:294, 2017. (Cited on pages 6, 10, 14, and 26.)

[2] F. de Juan, R. Ilan, and J. H. Bardarson. Robust transport signatures of topological superconductivity in topological insulator nanowires. *Phys. Rev. Lett.*, 113:107003, 2014. (Cited on pages 6, 10, and 14.)

[3] R. Yu, W. Zhang, H. Zhang, S. Zhang, X. Dai, and Z. Fang. Quantized anomalous Hall effect in magnetic topological insulators. *Science*, 329:61, 2010. (Cited on pages 6, 14, and 45.)

[4] Cui-Zu Chang, Jinsong Zhang, Xiao Feng, Jie Shen, Zuocheng Zhang, Minghua Guo, Kang Li, Yunbo Ou, Pang Wei, Li-Li Wang, Zhong-Qing Ji, Yang Feng, Shuaihua Ji, Xi Chen, Jinfeng Jia, Xi Dai, Zhong Fang, Shou-Cheng Zhang, Ke He, Yayu Wang, Li Lu, Xu-Cun Ma, and Qi-Kun Xue. Experimental observation of the quantum anomalous Hall effect in a magnetic topological insulator. *Science*, 340:167, 2013. (Cited on pages 6, 10, 14, 24, 26, 46, and 47.)

[5] C. Chang, W. Zhao, D. Y. Kim, H. Zhang, B. A. Assaf, D. Heiman, S. Zhang, C. Liu, M. H. W. Chan, and J. S. Moodera. High-precision realization of robust quantum anomalous Hall state in a hard ferromagnetic topological insulator. *Nat. Mater.*, 14:473, 2015. (Cited on pages 6, 10, 14, 46, and 47.)

[6] J. G. Checkelsky, J. Ye, Y. Onose, Y. Iwasa, and Y. Tokura. Dirac-fermion-mediated ferromagnetism in a topological insulator. *Nat. Phys.*, 8:729, 2012. (Cited on pages 6, 10, 14, 45, 46, and 71.)

[7] R. Watanabe, R. Yoshimi, M. Kawamura, M. Mogi, A. Tsukazaki, X. Z. Yu, K. Nakajima, K. S. Takahashi, M. Kawasaki, and Y. Tokura. Quantum anomalous Hall effect driven by magnetic proximity coupling in all-telluride based heterostructure. *Appl. Phys. Lett.*, 115:102403, 2019. (Cited on pages 6, 10, 14, 47, and 48.)

[8] R. S. K. Mong, A. M. Essin, and J. E. Moore. Antiferromagnetic topological insulators. *Phys. Rev. B*, 81:245209, 2010. (Cited on pages 6, 14, 48, and 51.)

[9] M. M. Otrokov, I. I. Klimovskikh, H. Bentmann, D. Estyunin, A. Zeugner, Z. S. Aliev, S. Gaß, A. U. B. Wolter, A. V. Koroleva, A. M. Shikin, M. Blanco-Rey, M. Hoffmann, I. P. Rusinov, A. Yu. Vyazovskaya, S. V. Eremeev, Yu. M. Koroteev, V. M. Kuznetsov, F. Freyse, J. Sánchez-Barriga, I. R. Amiraslanov, M. B. Babanly, N. T. Mamedov, N. A. Abdullayev, V. N. Zverev, A. Alfonsov, V. Kataev, B. Büchner, E. F. Schwier, S. Kumar, A. Kimura, L. Petaccia, G. Di Santo, R. C. Vidal, S. Schatz, K. Kißner, M. Ünzelmann, C. H. Min,

Simon Moser, T. R. F. Peixoto, F. Reinert, A. Ernst, P. M. Echenique, Isaeva A., and E. V. Chulkov. Prediction and observation of an antiferromagnetic topological insulator. *Nature*, 576:416, 2019. (Cited on pages 6, 7, 10, 11, 15, 26, 49, 50, 51, 52, 53, 68, and 77.)

[10] R. C. Vidal, A. Zeugner, J. I. Facio, R. Ray, M. H. Haghighi, A. U. B. Wolter, L. T. Corredor Bohorquez, F. Caglieris, S. Moser, T. Figgemeier, T. R. F. Peixoto, H. B. Vasili, M. Valvidares, S. Jung, C. Cacho, A. Alfonsov, K. Mehlawat, V. Kataev, C. Hess, M. Richter, B. Büchner, J. van den Brink, M. Ruck, F. Reinert, H. Bentmann, and A. Isaeva. Topological electronic structure and intrinsic magnetization in $MnBi_4Te_7$: A Bi_2Te_3 derivative with a periodic Mn sublattice. *Phys. Rev. X*, 9:041065, 2019. (Cited on pages 6, 7, 10, 11, 15, 26, 56, 68, 74, 76, 77, 80, and 81.)

[11] M. M. Otrokov, I. P. Rusinov, M. Blanco-Rey, M. Hoffmann, A. Yu. Vyazovskaya, S. V. Eremeev, A. Ernst, P. M. Echenique, A. Arnau, and E. V. Chulkov. Unique thickness-dependent properties of the van der Waals interlayer antiferromagnet $MnBi_2Te_4$ films. *Phys. Rev. Lett.*, 122:107202, 2019. (Cited on pages 6, 11, 15, 26, 49, 50, and 77.)

[12] A. Zeugner, F. Nietschke, A. U. B. Wolter, S. Gaß, R. C. Vidal, T. R. F. Peixoto, D. Pohl, C. Damm, A. Lubk, R. Hentrich, S. K. Moser, C. Fornari, C. H. Min, S. Schatz, K. Kißner, M. Ünzelmann, M. Kaiser, F. Scaravaggi, B. Rellinghaus, K. Nielsch, C. Hess, B. Büchner, F. Reinert, H. Bentmann, O. Oeckler, T. Doert, M. Ruck, and A. Isaeva. Chemical aspects of the candidate antiferromagnetic topological insulator $MnBi_2Te_4$. *Chem. Mater.*, 31:2795, 2019. (Cited on pages 7, 56, 57, and 106.)

[13] P. Kagerer, C. I. Fornari, S. Buchberger, S. L. Morelhão, R. C. Vidal, A. Tcakaev, V. Zabolotnyy, E. Weschke, V. Hinkov, M. Kamp, B. Büchner, A. Isaeva, H. Bentmann, and F. Reinert. Molecular beam epitaxy of antiferromagnetic $(MnBi_2Te_4)(Bi_2Te_3)$ thin films on BaF_2 (111). *J. Appl. Phys.*, 128:135303, 2020. (Cited on pages 7 and 94.)

[14] L. Ding, C. Hu, F. Ye, E. Feng, N. Ni, and H. Cao. Crystal and magnetic structures of magnetic topological insulators $MnBi_2Te_4$ and $MnBi_4Te_7$. *Phys. Rev. B*, 101:020412, 2020. (Cited on pages 7 and 11.)

[15] L. Veyrat, F. Iacovella, J. Dufouleur, C. Nowka, H. Funke, M. Yang, W. Escoffier, M. Goiran, B. Eichler, O. G. Schmidt, B. Büchner, S. Hampel, and R. Giraud. Band bending inversion in Bi_2Se_3 nanostructures. *Nano Lett.*, 15:7503, 2015. (Cited on pages 7 and 65.)

[16] A. Tan, V. Labracherie, N. Kunchur, A. U. B. Wolter, J. Cornejo, J. Dufouleur, B. Büchner, A. Isaeva, and R. Giraud. Metamagnetism of weakly coupled antiferromagnetic topological insulators. *Phys. Rev. Lett.*, 124:197201, 2020. (Cited on pages 7, 11, 15, 80, and 107.)

[17] A. N. Bogdanov, A. V. Zhuravlev, and U. K. Rößler. Spin-flop transition in uniaxial antiferromagnets: Magnetic phases, reorientation effects, and multidomain states. *Phys. Rev. B*, 75:094425, 2007. (Cited on pages 8, 12, 87, and 91.)

[18] E. J. Fox, I. T. Rosen, Y. Yang, G. R. Jones, R. E. Elmquist, X. Kou, L. Pan, K. L. Wang, and D. Goldhaber-Gordon. Part-per-million quantization and current-induced breakdown of the quantum anomalous Hall effect. *Phys. Rev. B*, 98:075145, 2018. (Cited on page 10.)

[19] Y. Okazaki, T. Oe, M. Kawamura, R. Yoshimi, S. Nakamura, S. Takada, M. Mogi, K. S. Takahashi, A. Tsukazaki, M. Kawasaki, Y. Tokura, and N. Kaneko. Precise resistance measurement of quantum anomalous Hall effect in magnetic heterostructure film of topological insulator. *Appl. Phys. Lett.*, 116:143101, 2020. (Cited on page 10.)

[20] K. Dawon. Electric field controlled semiconductor device, 1960. (Cited on page 23.)

[21] K. v. Klitzing, G. Dorda, and M. Pepper. New method for high-accuracy determination of the fine-structure constant based on quantized Hall resistance. *Phys. Rev. Lett.*, 45:494, 1980. (Cited on pages 23 and 36.)

[22] K. von Klitzing. The quantized Hall effect. *Rev. Mod. Phys.*, 58:519, 1986. (Cited on pages 23 and 36.)

[23] R. Willett, H. L. Stormer, D.C. Tsui, A. C. Gossard, J. H. English, and K. W. Baldwin. Fractional quantum Hall effect in extremely high mobility GaAs/(AlGa)As heterostructures. *Surface Science*, 196:257, 1988. (Cited on page 23.)

[24] K. S. Novoselov, A. K. Geim, S. V. Morozov, D. Jiang, Y. Zhang, S. V. Dubonos, I. V. Grigorieva, and A. A. Firsov. Electric field effect in atomically thin carbon films. *Science*, 306(5696):666, 2004. (Cited on pages 23 and 57.)

[25] K.I. Bolotin, K.J. Sikes, Z. Jiang, M. Klima, G. Fudenberg, J. Hone, P. Kim, and H.L. Stormer. Ultrahigh electron mobility in suspended graphene. *Solid State Comm.*, 146:351, 2008. (Cited on page 24.)

[26] K. S. Novoselov, Z. Jiang, Y. Zhang, S. V. Morozov, H. L. Stormer, U. Zeitler, J. C. Maan, G. S. Boebinger, P. Kim, and A. K. Geim. Room-temperature quantum Hall effect in graphene. *Science*, 315(5817):1379, 2007. (Cited on page 24.)

[27] M. Z. Hasan and C. L. Kane. Colloquium: Topological insulators. *Rev. Mod. Phys.*, 82:3045, 2010. (Cited on page 24.)

[28] M. König, S. Wiedmann, C. Brüne, A. Roth, H. Buhmann, L. W. Molenkamp, X. Qi, and Zhang. S. Quantum spin Hall insulator state in HgTe quantum wells. *Science*, 318:766, 2007. (Cited on page 24.)

[29] Liang Fu and C. L. Kane. Superconducting proximity effect and Majorana fermions at the surface of a topological insulator. *Phys. Rev. Lett.*, 100:096407, 2008. (Cited on page 24.)

[30] J.-C. Rojas-Sánchez, S. Oyarzún, Y. Fu, A. Marty, C. Vergnaud, S. Gambarelli, L. Vila, M. Jamet, Y. Ohtsubo, A. Taleb-Ibrahimi, P. Le Fèvre, F. Bertran, N. Reyren, J.-M. George, and A. Fert. Spin to charge conversion at room temperature by spin pumping into a new type of topological insulator: α-Sn films. *Phys. Rev. Lett.*, 116:096602, 2016. (Cited on page 24.)

[31] J. Dufouleur, L. Veyrat, B. Dassonneville, C. Nowka, S. Hampel, P. Leksin, B. Eichler, O. G. Schmidt, B. Büchner, and R. Giraud. Enhanced mobility of spin-helical dirac fermions in disordered 3D topological insulators. *Nano Lett.*, 16:6733, 2016. (Cited on page 24.)

[32] H. C. Han, Y. S. Chen, M. D. Davydova, P. N. Petrov, P. N. Skirdkov, J. G. Lin, J. C. Wu, J. C. A. Huang, K. A. Zvezdin, and A. K. Zvezdin. Spin pumping and probe in permalloy dots-topological insulator bilayers. *Appl. Phys. Lett.*, 111:182411, 2017. (Cited on page 25.)

[33] S. Shi, A. Wang, Y. Wang, R. Ramaswamy, L. Shen, J. Moon, D. Zhu, J. Yu, S. Oh, Y. Feng, and H. Yang. Efficient charge-spin conversion and magnetization switching through the Rashba effect at topological-insulator/Ag interfaces. *Phys. Rev. B*, 97:041115, 2018. (Cited on page 25.)

[34] A. R. Mellnik, J. S. Lee, A. Richardella, J. L. Grab, P. J. Mintun, M. H. Fischer, A. Vaezi, A. Manchon, E.-A. Kim, N. Samarth, and D. C. Ralph. Spin-transfer torque generated by a topological insulator. *Nature*, 511:449, 2014. (Cited on page 25.)

[35] K. Kondou, R. Yoshimi, A. Tsukazaki, Y. Fukuma, J. Matsuno, K. S. Takahashi, M. Kawasaki1, Y. Tokura, and Y. Otani. Fermi-level-dependent charge-to-spin current conversion by Dirac surface states of topological insulators. *Nat. Phys.*, 12:1027, 2016. (Cited on page 25.)

[36] P. Deorani, J. Son, K. Banerjee, N. Koirala, M. Brahlek, S. Oh, and H. Yang. Observation of inverse spin Hall effect in bismuth selenide. *Phys. Rev. B*, 90:094403, 2014. (Cited on page 25.)

[37] K. T. Yamamoto, Y. Shiomi, Kouji Segawa, Yoichi Ando, and E. Saitoh. Universal scaling for the spin-electricity conversion on surface states of topological insulators. *Phys. Rev. B*, 94:024404, 2016. (Cited on page 25.)

[38] S. Ohya, A. Yamamoto, T. Yamaguchi, R. Ishikawa, R. Akiyama, L. D. Anh, S. Goel, Y. K. Wakabayashi, S. Kuroda, and M. Tanaka. Observation of the inverse spin Hall effect in the topological crystalline insulator SnTe using spin pumping. *Phys. Rev. B*, 96:094424, 2017. (Cited on page 25.)

[39] J. B. S. Mendes, O. Alves Santos, J. Holanda, R. P. Loreto, C. I. L. de Araujo, Cui-Zu Chang, J. S. Moodera, A. Azevedo, and S. M. Rezende. Dirac-surface-state-dominated spin to charge current conversion in the topological insulator $(Bi_{0.22}Sb_{0.78})_2Te_3$ films at room temperature. *Phys. Rev. B*, 96:180415, 2017. (Cited on page 25.)

[40] S. Shi, A. Wang, Y. Wang, R. Ramaswamy, L. Shen, J. Moon, D. Zhu, J. Yu, S. Oh, Y. Feng, and H. Yang. Efficient charge-spin conversion and magnetization switching through the rashba effect at topological-insulator\Ag interfaces. *Phys. Rev. B*, 97:041115, 2018. (Cited on page 25.)

[41] Y. Wang, P. Deorani, K. Banerjee, N. Koirala, M. Brahlek, S. Oh, and H. Yang. Topological surface states originated spin-orbit torques in Bi_2Se_3. *Phys. Rev. Lett.*, 114:257202, 2015. (Cited on page 25.)

[42] H. Wang, J. Kally, J. S. Lee, T. Liu, H. Chang, D. R. Hickey, K. A. Mkhoyan, M. Wu, A. Richardella, and N. Samarth. Surface-state-dominated spin-charge current conversion in topological-insulator–ferromagnetic-insulator heterostructures. *Phys. Rev. Lett.*, 117:076601, 2016. (Cited on page 25.)

[43] J. Han, A. Richardella, S. A. Siddiqui, J. Finley, N. Samarth, and L. Liu. Room-temperature spin-orbit torque switching induced by a topological insulator. *Phys. Rev. Lett.*, 119:077702, 2017. (Cited on page 25.)

[44] P. Noel, C. Thomas, Y. Fu, L. Vila, B. Haas, P-H. Jouneau, S. Gambarelli, T. Meunier, P. Ballet, and J. P. Attané. Highly efficient spin-to-charge current conversion in strained HgTe surface states protected by a HgCdTe layer. *Phys. Rev. Lett.*, 120:167201, 2018. (Cited on page 25.)

[45] Y. Wang, D. Zhu, Y. Wu, Y. Yang, J. Yu, R. Ramaswamy, R. Mishra, S. Shi, M. Elyasi, K. Teo, Y. Wu, and H. Yang. Room temperature magnetization switching in topological insulator-ferromagnet heterostructures by spin-orbit torques. *Nat. Comm.*, 8:1364, 2017. (Cited on page 25.)

[46] Y. Liu, J. Besbas, Y. Wang, P. He, M. Chen, D. Zhu, Y. Wu, J. M. Lee, L. Wang, J. Moon, N. Koirala, S. Oh, and H. Yang. Direct visualization of current-induced spin accumulation in topological insulators. *Nat. Comm.*, 9:2492, 2018. (Cited on page 25.)

[47] M. DC, R. Grassi, J. Chen, M. Jamali, D. Reifsnyder Hickey, D. Zhang, Z. Zhao, H. Li, P. Quarterman, Y. Lv, M. Li, A. Manchon, K. A. Mkhoyan, T. Low, and J. Wang. Room-temperature high spin–orbit torque due to quantum confinement in sputtered $Bi_xSe_{(1-x)}$ films. *Nat. Mat.*, 17:800, 2018. (Cited on page 25.)

[48] F. D. M. Haldane. Model for a quantum Hall effect without Landau levels: Condensed-matter realization of the "parity anomaly". *Phys. Rev. Lett.*, 61:2015, 1988. (Cited on page 24.)

[49] J. Li, Y. Li, S. Du, Z. Wang, B. Gu, S. Zhang, K. He, W. Duan, and Y. Xu. Intrinsic magnetic topological insulators in van der Waals layered $MnBi_2Te_4$-family materials. *Sci. Adv.*, 5(6), 2019. (Cited on pages 26, 50, and 51.)

[50] M. Z. Shi, B. Lei, C. S. Zhu, D. H. Ma, J. H. Cui, Z. L. Sun, J. J. Ying, and X. H. Chen. Magnetic and transport properties in the magnetic topological insulators $MnTe(Bi_2Te_3)_n$ $(n = 1, 2)$. *Phys. Rev. B*, 100:155144, 2019. (Cited on page 26.)

[51] B. Huang, G. Clark, E. Navarro-Moratalla, D. R. Klein, R. Cheng, K. L. Seyler, D. Zhong, E. Schmidgall, M. A. McGuire, D. H. Cobden, W. Yao, D. Xiao, P. Jarillo-Herrero, and X. Xu. Layer-dependent ferromagnetism in a van der Waals crystal down to the monolayer limit. *Nature*, 546:270, 2017. (Cited on pages 26 and 49.)

[52] Y. Deng, Y. Yu, M. Z. Shi, Z. Guo, Z. Xu, J. Wang, X. H. Chen, and Y. Zhang. Quantum anomalous Hall effect in intrinsic magnetic topological insulator $MnBi_2Te_4$. *Science*, 367:895, 2020. (Cited on pages 26, 51, and 53.)

[53] C. Gong, L. Li, Z. Li, H. Ji, A. Stern, Y. Xia, T. Cao, W. Bao, C. Wang, Y. Wang, Z. Q. Qiu, R. J. Cava, S. G. Louie, J. Xia, and X. Zhang. Discovery of intrinsic ferromagnetism in two-dimensional van der Waals crystals. *Nature*, 546:265, 2017. (Cited on pages 26 and 49.)

[54] K. Seeger. *Semiconductor physics*. Springer, Berlin, 2004. (Cited on page 29.)

[55] M. Onoda and N. Nagaosa. Topological nature of anomalous Hall effect in ferromagnets. *J. Phys. Soc. Jpn*, 71:19, 2002. (Cited on pages 29 and 31.)

[56] S. Onoda, N. Sugimoto, and N. Nagaosa. Intrinsic versus extrinsic anomalous Hall effect in ferromagnets. *Phys. Rev. Lett.*, 97:126602, 2006. (Cited on pages 29 and 30.)

[57] N. Nagaosa, J. Sinova, S. Onoda, A. H. MacDonald, and N. P. Ong. Anomalous Hall effect. *Rev. Mod. Phys.*, 82:1539, 2010. (Cited on page 30.)

[58] R. Karplus and J. M. Luttinger. Hall effect in ferromagnetics. *Phys. Rev.*, 95:1154, 1954. (Cited on page 30.)

[59] J. Smit. The spontaneous Hall effect in ferromagnetics I. *Physica (Amsterdam)*, 21:877, 1955. (Cited on page 30.)

[60] L. Berger. Side-jump mechanism for the Hall effect of ferromagnets. *Phys. Rev. B*, 2:4559, 1970. (Cited on page 30.)

[61] A. K. Nayak, J. E. Fischer, Y. Sun, B. Yan, J. Karel, A. C. Komarek, C. Shekhar, N. Kumar, W. Schnelle, J. Kübler, C. Felser, and S. S. P. Parkin. Large anomalous Hall effect driven by a nonvanishing Berry curvature in the noncolinear antiferromagnet Mn_3Ge. *Sci. Adv.*, 2(4), 2016. (Cited on page 30.)

[62] G. Metalidis and P. Bruno. Topological Hall effect studied in simple models. *Phys. Rev. B*, 74:045327, 2006. (Cited on page 30.)

[63] N. Kanazawa, Y. Onose, T. Arima, D. Okuyama, K. Ohoyama, S. Wakimoto, K. Kakurai, S. Ishiwata, and Y. Tokura. Large topological Hall effect in a short-period helimagnet MnGe. *Phys. Rev. Lett.*, 106:156603, 2011. (Cited on page 30.)

[64] K. Yasuda, R. Wakatsuki, T. Morimoto, R. Yoshimi, A. Tsukazaki, K. S. Takahashi, M. Ezawa, M. Kawasaki, N. Nagaosa, and Y. Tokura. Geometric Hall effects in topological insulator heterostructures. *Nature*, 12:555, 2016. (Cited on page 31.)

[65] C. Liu, Y. Zang, W. Ruan, Y. Gong, K. He, X. Ma, Q. Xue, and Y. Wang. Dimensional crossover-induced topological Hall effect in a magnetic topological insulator. *Phys. Rev. Lett.*, 119:176809, 2017. (Cited on page 31.)

[66] J. Jiang, D. Xiao, F. Wang, J. Shin, D. Andreoli, J. Zhang, R. Xiao, Y. Zhao, M. Kayyalha, L. Zhang, K. Wang, J. Zang, C. Liu, N. Samarth, M. H. W. Chan, and C. Chang. Geometric Hall effects in topological insulator heterostructures. *Nat. Mat.*, 19:732, 2020. (Cited on page 31.)

[67] J. J. Nakane, K. Nakazawa, and H. Kohno. Topological Hall effect in weakly canted antiferromagnets. *Phys. Rev. B*, 101:174432, 2020. (Cited on page 31.)

[68] L. Šmejkal, R. González-Hernández, T. Jungwirth, and J. Sinova. Crystal time-reversal symmetry breaking and spontaneous Hall effect in collinear antiferromagnets. *Sci. Adv.*, 6(23), 2020. (Cited on page 31.)

[69] Z. Feng, X. Zhou, L. Šmejkal, L. Wu, Z. Zhu, H. Guo, R. González-Hernández, X. Wang, H. Yan, P. Qin, X. Zhang, H. Wu, H. Chen, Z. Xia, C. Jiang, M. Coey, J. Sinova, T. Jungwirth, and Z. Liu. Observation of the anomalous Hall effect in a collinear antiferromagnet, 2021. (Cited on page 31.)

[70] J. Sinova, D. Culcer, Q. Niu, N. A. Sinitsyn, T. Jungwirth, and A. H. MacDonald. Universal intrinsic spin Hall effect. *Phys. Rev. Lett.*, 92:126603, 2004. (Cited on page 31.)

[71] J. Sinova, S. O. Valenzuela, J. Wunderlich, C. H. Back, and T. Jungwirth. Spin Hall effects. *Rev. Mod. Phys.*, 87:1213, 2015. (Cited on page 31.)

[72] M. V. Berry. Quantal phase factors accompanying adiabatic changes. *Proc. R. Soc. Lond.*, 392:45, 1984. (Cited on page 32.)

[73] R. Kubo. Statistical-mechanical theory of irreversible processes. I. General theory and simple applications to magnetic and conduction problems. *J. Phys. Soc. Jpn.*, 12:570, 1957. (Cited on page 34.)

[74] M. Kohmoto. Topological invariant and the quantization of the Hall conductance. *Ann. Phys.*, 160:343, 1985. (Cited on page 34.)

[75] C. L. Kane and E. J. Mele. Z_2 topological order and the quantum spin Hall effect. *Phys. Rev. Lett.*, 95:146802, 2005. (Cited on page 36.)

[76] B. Andrei Bernevig, Taylor L. Hughes, and Shou-Cheng Zhang. Quantum spin Hall effect and topological phase transition in HgTe quantum wells. *Science*, 314:1757, 2006. (Cited on page 37.)

[77] M. König, S. Wiedmann, C. Brüne, A. Roth, H. Buhmann, L. W. Molenkamp, X. Qi, and S. Zhang. Quantum spin Hall insulator state in HgTe quantum wells. *Science*, 318:766, 2007. (Cited on pages 37 and 38.)

[78] Y. Zhao, R. Zhang, R. Mei, L. Zhou, H. Yi, Y. Zhang, J. Yu, R. Xiao, K. Wang, N. Samarth, M. H. W. Chan, Liu C., and C. Chang. Tuning the Chern number in quantum anomalous Hall insulators. *Nature*, 588:419, 2020. (Cited on page 40.)

[79] L. Fu, C. L. Kane, and E. J. Mele. Topological insulators in three dimensions. *Phys. Rev. Lett.*, 98:106803, 2007. (Cited on page 42.)

[80] L. Fu and C. L. Kane. Topological insulators with inversion symmetry. *Phys. Rev. B*, 76:045302, 2007. (Cited on page 43.)

[81] H. Zhang, C. Liu, X. Qi, X. Dai, Z. Fang, and S. Zhang. Topological insulators in Bi_2se_3, Bi_2Te_3 and Sb_2Te_3 with a single dirac cone on the surface. *Nat. Phys.*, 5:438, 2009. (Cited on page 43.)

[82] D. Hsieh, Y. Xia, L. Wray, D. Qian, A. Pal, J. H. Dil, J. Osterwalder, F. Meier, G. Bihlmayer, C. L. Kane, Y. S. Hor, R. J. Cava, and M. Z. Hasan. Observation of unconventional quantum spin textures in topological insulators. *Science*, 323:919, 2009. (Cited on page 43.)

[83] Y. Xia, D. Qian, D. Hsieh, L. Wray, A. Pal, H. Lin, A. Bansil, D. Grauer, Y. S. Hor, R. J. Cava, and M. Z. Hasan. Observation of a large-gap topological-insulator class with a single dirac cone on the surface. *Nat. Phys.*, 5:398, 2009. (Cited on page 43.)

[84] Y. L. Chen, J. G. Analytis, J.-H. Chu, Z. K. Liu, S.-K. Mo, X. L. Qi, H. J. Zhang, D. H. Lu, X. Dai, Z. Fang, S. C. Zhang, I. R. Fisher, Z. Hussain, and Z.-X. Shen. Experimental realization of a three-dimensional topological insulator, Bi_2Te_3. *Science*, 325:178, 2009. (Cited on pages 43 and 44.)

[85] M. Neupane, S.-Y. Xu, L. A. Wray, A. Petersen, R. Shankar, N. Alidoust, Chang Liu, A. Fedorov, H. Ji, J. M. Allred, Y. S. Hor, T.-R. Chang, H.-T. Jeng, H. Lin, A. Bansil, R. J. Cava, and M. Z. Hasan. Topological surface states and Dirac point tuning in ternary topological insulators. *Phys. Rev. B*, 85:235406, 2012. (Cited on page 44.)

[86] J. Kellner, M. Eschbach, J. Kampmeier, M. Lanius, E. Młyńczak, G. Mussler, B. Holländer, L. Plucinski, M. Liebmann, D. Grützmacher, C. M. Schneider, and M. Morgenstern. Tuning the Dirac point to the Fermi level in the ternary topological insulator $(Bi_{1-x}Sb_x)_2Te_3$. *Appl. Phys. Lett.*, 107:251603, 2015. (Cited on page 44.)

[87] J. Zhang, C. Chang, Z. Zhang, J. Wen, X. Feng, K. Li, M. Liu, K. He, L. Wang, X. Chen, Q. Xue, X. Ma, and Y. Wang. Band structure engineering in $(Bi_{1-x}Sb_x)_2Te_3$ ternary topological insulators. *Nat. Comm.*, 2(574), 2011. (Cited on page 44.)

[88] J. B. Staunton, B. L. Gyorffy, J. Poulter, and P. Strange. A relativistic RKKY interaction between two magnetic impurities-the origin of a magnetic anisotropic effect. *Jour. Phys. C: Solid State*, 21:1595, 1988. (Cited on page 45.)

[89] A. Singh, A. Datta, S. K. Das, and V. A. Singh. Ferromagnetism in a dilute magnetic semiconductor: Generalized RKKY interaction and spin-wave excitations. *Phys. Rev. B*, 68:235208, 2003. (Cited on page 45.)

[90] Y. L. Chen, J.-H. Chu, J. G. Analytis, Z. K. Liu, K. Igarashi, H.-H. Kuo, X. L. Qi, S. K. Mo, R. G. Moore, D. H. Lu, M. Hashimoto, T. Sasagawa, S. C. Zhang, I. R. Fisher, Z. Hussain, and Z. X. Shen. Massive dirac fermion on the surface of a magnetically doped topological insulator. *Science*, 329:659, 2010. (Cited on page 45.)

[91] Y. Tokura, K. Yasuda, and A. Tsukazaki. Magnetic topological insulators. *Nat. Rev. Phys.*, 1:126, 2019. (Cited on page 46.)

[92] I. Lee, C. K. Kim, J. Lee, S. J. L. Billinge, R. Zhong, J. A. Schneeloch, T. Liu, T. Valla, J. M. Tranquada, G. Gu, and J. C. S. Davis. Imaging Dirac-mass disorder from magnetic dopant atoms in the ferromagnetic topological insulator $Cr_x(Bi_{0.1}Sb_{0.9})_{2-x}Te_3$. *Proc. Natl. Acad. Sci. USA*, 112:1316, 2015. (Cited on page 47.)

[93] C. Chang and M. Li. Quantum anomalous Hall effect in time-reversal-symmetry breaking topological insulators. *J. Phys.: Condense Matter*, 28:123002, mar 2016. (Cited on pages 46 and 47.)

[94] Z. Jiang, C. Chang, C. Tang, P. Wei, J. S. Moodera, and J. Shi. Independent tuning of electronic properties and induced ferromagnetism in topological insulators with heterostructure approach. *Nano Lett.*, 15:5835, 2015. (Cited on page 47.)

[95] A. I. Figueroa, F. Bonell, M. G. Cuxart, M. Valvidares, P. Gargiani, G. van der Laan, A. Mugarza, and S. O. Valenzuela. Absence of magnetic proximity effect at the interface of Bi_2Te_3 and $(Bi,Sb)_2Te_3$ with EuS. *Phys. Rev. Lett.*, 125:226801, 2020. (Cited on page 47.)

[96] P. Chen, Y. Zhang, Q. Yao, F. Tian, L. Li, Z. Qi, X. Liu, L. Liao, C. Song, J. Wang, J. Xia, G. Li, D. M. Burn, G. van der Laan, T. Hesjedal, S. Zhang, and X. Kou. Tailoring the hybrid anomalous Hall response in engineered magnetic topological insulator heterostructures. *Nano Lett.*, 20:1731, 2020. (Cited on page 47.)

[97] K. S. Novoselov, D. Jiang, F. Schedin, T. J. Booth, V. V. Khotkevich, S. V. Morozov, and A. K. Geim. Two-dimensional atomic crystals. *Proc. Nat. Acad. Sci.*, 102:10451, 2005. (Cited on page 48.)

[98] K. S. Burch, D. Mandrus, and J. Park. Magnetism in two-dimensional van der Waals materials. *Nature*, 563:47, 2018. (Cited on page 49.)

[99] Y. Deng, Y. Yu, Y. Song, J. Zhang, N. Z. Wang, Z. Sun, Y. Yi, Yi Z. Wu, S. Wu, J. Zhu, J. Wang, X. Hui Chen, and Y. Zhang. Gate-tunable room-temperature ferromagnetism in two-dimensional Fe_3GeTe_2. *Nature*, 563:94, 2018. (Cited on page 49.)

[100] J. Lee, S. Lee, J. Ryoo, S. Kang, T. Y. Kim, P. Kim, C. Park, J. Park, and H. Cheong. Ising-type magnetic ordering in atomically thin $FePS_3$. *Nano Lett.*, 16:7433, 2016. (Cited on page 49.)

[101] G. Long, H. Henck, M. Gibertini, D. Dumcenco, Z. Wang, T. Taniguchi, K. Watanabe, E. Giannini, and A. F. Morpurgo. Persistence of magnetism in atomically thin $MnPS_3$ crystals. *Nano Lett.*, 20:2452, 2020. (Cited on page 49.)

[102] Y. Peng, S. Ding, M. Cheng, Q. Hu, J. Yang, F. Wang, M. Xue, Z. Liu, Z. Lin, M. Avdeev, Y. Hou, W. Yang, Y. Zheng, and J. Yang. Magnetic structure and metamagnetic transitions in the van der Waals antiferromagnet $CrPS_4$. *Adv. Mater.*, 32:2001200, 2020. (Cited on pages 49 and 50.)

[103] P. Jiang, C. Wang, D. Chen, Z. Zhong, Z. Yuan, Z. Lu, and W. Ji. Stacking tunable interlayer magnetism in bilayer CrI_3. *Phys. Rev. B*, 99:144401, 2019. (Cited on page 49.)

[104] N. Sivadas, S. Okamoto, X. Xu, C. J. Fennie, and D. Xiao. Stacking-dependent magnetism in bilayer CrI_3. *Nano Lett.*, 18:7658, 2018. (Cited on page 49.)

[105] D. Zhang, M. Shi, T. Zhu, D. Xing, H. Zhang, and J. Wang. Topological axion states in the magnetic insulator $MnBi_2Te_4$ with the quantized magnetoelectric effect. *Phys. Rev. Lett.*, 122:206401, 2019. (Cited on page 51.)

[106] C. Liu, Y. Wang, H. Li, Y. Wu, Y. Li, J. Li, K. He, Y. Xu, Zhang J., and Y. Wang. Robust axion insulator and Chern insulator phases in a two-dimensional antiferromagnetic topological insulator. *Nat. Mat.*, 19:522, 2020. (Cited on page 51.)

[107] Z. S. Aliev, I. R. Amiraslanov, D. I. Nasonova, A. V. Shevelkov, N. A. Abdullayev, Z. A. Jahangirli, E. N. Orujlu, M. M. Otrokov, N. T. Mamedov, M. B. Babanly, and E. V. Chulkov. Novel ternary layered manganese bismuth tellurides of the $MnTe$-Bi_2Te_3 system: Synthesis and crystal structure. *J. Alloy Compd.*, 789:443, 2019. (Cited on page 52.)

[108] I. I. Klimovskikh, M. M. Otrokov, D. Estyunin, S. V. Eremeev, S. O. Filnov, A. Koroleva, E. Shevchenko, V. Voroshnin, A. G. Rybkin, I. P. Rusinov, M. Blanco-Rey, M. Hoffmann, Z. S. Aliev, M. B. Babanly, I. R. Amiraslanov, N. A. Abdullayev, V. N. Zverev, A. Kimura, O. E. Tereshchenko, K. A. Kokh, L. Petaccia, G. D. Santo, A. Ernst, P. M. Echenique, N. T. Mamedov, A. M. Shikin, and E. V. Chulkov. Tunable 3D/2D magnetism in the $(MnBi_2Te_4)(Bi_2Te_3)_m$ topological insulators family. *npj Quantum Materials*, 5, 2020. (Cited on pages 52, 54, 77, and 93.)

[109] Y. J. Chen, L. X. Xu, J. H. Li, Y. W. Li, H. Y. Wang, C. F. Zhang, H. Li, Y. Wu, A. J. Liang, C. Chen, S. W. Jung, C. Cacho, Y. H. Mao, S. Liu, M. X. Wang, Y. F. Guo, Y. Xu, Z. K. Liu, L. X. Yang, and Y. L. Chen. Topological electronic structure and its temperature evolution in antiferromagnetic topological insulator $MnBi_2Te_4$. *Phys. Rev. X*, 9:041040, 2019. (Cited on page 54.)

[110] E. D. L. Rienks, S. Wimmer, J. Sánchez-Barriga, O. Caha, P. S. Mandal, J. Růžička, A. Ney, H. Steiner, V. V. Volobuev, H. Groiss, M. Albu, G. Kothleitner, J. Michalička, S. A. Khan, J. Minár, H. Ebert, G. Bauer, F. Freyse, A. Varykhalov, O. Rader, and G. Springholz. Large magnetic gap at the dirac point in $Bi_2Te_3/MnBi_2Te_4$ heterostructures. *Nature*, 576:423, 2019. (Cited on page 54.)

[111] L. Xu, Y. Mao, H. Wang, J. Li, Y. Chen, Y. Xia, Y. Li, D. Pei, J. Zhang, H. Zheng, K. Huang, C. Zhang, S. Cui, A. Liang, W. Xia, H. Su, S. Jung, C. Cacho, M. Wang, G. Li, Y. Xu, Y. Guo, L. Yang, Z. Liu, Y. Chen, and M. Jiang. Persistent surface states with diminishing gap in $MnBi_2Te_4/Bi_2Te_3$ superlattice antiferromagnetic topological insulator. *Sci. Bull.*, 65:2086, 2020. (Cited on page 54.)

[112] H. Li, S. Gao, S. Duan, Y. Xu, K. Zhu, S. Tian, J. Gao, W. Fan, Z. Rao, J. Huang, J. Li, D. Yan, Z. Liu, W. Liu, Y. Huang, Y. Li, Y. Liu, G. Zhang, P. Zhang, T. Kondo, S. Shin, H. Lei, Y. Shi, W. Zhang, H. Weng, T. Qian, and H. Ding. Dirac surface states in intrinsic magnetic topological insulators $EuSn_2As_2$ and $MnBi_{2n}Te_{3n+1}$. *Phys. Rev. X*, 9:041039, 2019. (Cited on page 54.)

[113] Y. Hao, P. Liu, Y. Feng, X. Ma, E. F. Schwier, M. Arita, S. Kumar, C. Hu, R. Lu, M. Zeng, Y. Wang, Z. Hao, H. Sun, K. Zhang, J. Mei, Ni N., L. Wu, K. Shimada, C. Chen, Q. Liu, and C. Liu. Gapless surface dirac cone in antiferromagnetic topological insulator $MnBi_2Te_4$. *Phys. Rev. X*, 9:041038, 2019. (Cited on page 54.)

[114] J. Wu, F. Liu, M. Sasase, K. Ienaga, Y. Obata, R. Yukawa, K. Horiba, H. Kumigashira, S. Okuma, T. Inoshita, and H. Hosono. Natural van der Waals heterostructural single crystals with both magnetic and topological properties. *Sci. Adv.*, 5(11), 2019. (Cited on pages 54, 74, 75, 79, 80, and 81.)

[115] K. N. Gordon, H. S., C. Hu, A. G. Linn, H. Li, Y. Liu, P. Liu, S. Mackey, Q. Liu, N. Ni, and D. Dessau. Strongly gapped topological surface states on protected surfaces of antiferromagnetic $MnBi_4Te_7$ and $MnBi_6Te_{10}$, 2019. (Cited on page 54.)

[116] J. Unguris, R. J. Celotta, and D. T. Pierce. Observation of two different oscillation periods in the exchange coupling of Fe/Cr/Fe(100). *Phys. Rev. Lett.*, 67:140, 1991. (Cited on page 54.)

[117] P. Grünberg, R. Schreiber, Y. Pang, M. B. Brodsky, and H. Sowers. Layered magnetic structures: Evidence for antiferromagnetic coupling of Fe layers across Cr interlayers. *Phys. Rev. Lett.*, 57:2442, 1986. (Cited on page 54.)

[118] B. Heinrich. *Basics of nano-thin film magnetism, in Handbook of spin transport and magnetism.* CRC Press, New York, 2012. (Cited on page 54.)

[119] R. A. Duine, Kyung-Jin Lee, Stuart S. P. Parkin, and M. D. Stiles. Synthetic antiferromagnetic spintronics. *Nat. Phys.*, 14:217, 2018. (Cited on page 55.)

[120] D. Souchay, M. Nentwig, D. Günther, S. Keilholz, J. de Boor, A. Zeugner, A. Isaeva, M. Ruck, A. U. B. Wolter, B. Büchner, and O. Oeckler. Layered manganese bismuth tellurides with $GeBi_4Te_7$- and $GeBi_6Te_{10}$-type structures: towards multifunctional materials. *J. Mater. Chem. C*, 7:9939, 2019. (Cited on pages 56, 57, and 106.)

[121] Y. Huang, E. Sutter, N. N. Shi, J. Zheng, T. Yang, D. Englund, H. Gao, and P. Sutter. Reliable exfoliation of large-area high-quality flakes of graphene and other two-dimensional materials. *ACS Nano*, 9:10612, 2015. (Cited on pages 57 and 106.)

[122] F. Pobell. *Matter and methods at low temperatures.* Springer, Berlin, 2007. (Cited on pages 61, 62, and 107.)

[123] A. T. A. M. de Waele. Basic operation of cryocoolers and related thermal machines. *J. Low Temp. Phys.*, 164:179, 2011. (Cited on pages 62 and 107.)

[124] S. H. Lee, Y. Zhu, Y. Wang, L. Miao, T. Pillsbury, H. Yi, S. Kempinger, J. Hu, C. A. Heikes, P. Quarterman, W. Ratcliff, J. A. Borchers, H. Zhang, X. Ke, D. Graf, N. Alem, C. Chang, N. Samarth, and Z. Mao. Spin scattering and noncollinear spin structure-induced intrinsic anomalous Hall effect in antiferromagnetic topological insulator $MnBi_2Te_4$. *Phys. Rev. Research*, 1:012011, 2019. (Cited on pages 64, 65, 68, and 72.)

[125] G. Binasch, P. Grünberg, F. Saurenbach, and W. Zinn. Enhanced magnetoresistance in layered magnetic structures with antiferromagnetic interlayer exchange. *Phys. Rev. B*, 39:4828, 1989. (Cited on page 64.)

[126] F. J. Ohkawa. Temperature dependence of electrical resistivity of metals. *J. Phys. Soc. Jpn.*, 44:1105, 1978. (Cited on page 65.)

[127] F. Werner. Hall measurements on low-mobility thin films. *J. Appl. Phys.*, 122:135306, 2017. (Cited on page 67.)

[128] J. Cui, M. Shi, H. Wang, F. Yu, T. Wu, X. Luo, J. Ying, and X. Chen. Transport properties of thin flakes of the antiferromagnetic topological insulator $MnBi_2Te_4$. *Phys. Rev. B*, 99:155125, 2019. (Cited on pages 68 and 71.)

[129] G. M. Stephen, O. A. Vail, J. Lu, A. Beck W., P. J. Taylor, and A. L. Friedman. Weak antilocalization and anisotropic magnetoresistance as a probe of surface states in topological $Bi_2Te_xSe_{3-x}$ thin films. *Sci. Rep.*, 10(4845), 2020. (Cited on page 68.)

[130] D. P. A. Holgado, K. Bolaños, S. de Castro, H. S. A. Monteiro, F. S. Pena, A. K. Okazaki, C. I. Fornari, P. H. O. Rappl, E. Abramof, D. A. W. Soares, and M. L. Peres. Shubnikov–de haas oscillations and Rashba splitting in Bi_2Te_3 epitaxial film. *Appl. Phys. Lett.*, 117:102108, 2020. (Cited on page 68.)

[131] B. Chen, F. Fei, D. Zhang, B. Zhang, W. Liu, S. Zhang, P. Wang, B. Wei, Y. Zhang, Z. Zuo, J. Guo, Q. Liu, Z. Wang, X. Wu, J. Zong, X. Xie, W. Chen, Z. Sun, S. Wang, Y. Zhang, M. Zhang, X. Wang, F. Song, H. Zhang, D. Shen, and B. Wang. Intrinsic magnetic topological insulator phases in the Sb doped $MnBi_2Te_4$ bulks and thin flakes. *Nat. Comm.*, 10:4469, 2019. (Cited on pages 73 and 94.)

[132] J. M. D. Coey. *Magnetism and Magnetic Materials*. Cambridge University Press, New York, 2009. (Cited on page 75.)

[133] C. Tannous and J. Gieraltowski. The Stoner-Wohlfarth model of ferromagnetism. *Eur. J. Phys.*, 29:475, 2008. (Cited on page 83.)

[134] B. Dieny, J. P. Gavigan, and J. P. Rebouillat. Magnetisation processes, hysteresis and finite-size effects in model multilayer systems of cubic or uniaxial anisotropy with antiferromagnetic coupling between adjacent ferromagnetic layers. *J. Phys.: Condens. Matter*, 2:159, 1990. (Cited on page 85.)

[135] H. Rohrer and H. Thomas. Phase transitions in the uniaxial antiferromagnet. *J. Appl. Phys.*, 40:1025, 1969. (Cited on page 87.)

[136] H. Kronmüller. Theory of nucleation fields in inhomogeneous ferromagnets. *Phys. Stat. Sol. (b)*, 144:385, 1987. (Cited on page 102.)

[137] M. P. Sharrock. Time dependence of switching fields in magnetic recording media. *J. Appl. Phys.*, 76:6413, 1994. (Cited on pages 103 and 104.)

[138] J. Moritz, B. Dieny, J. P. Nozières, Y. Pennec, J. Camarero, and S. Pizzini. Experimental evidence of a 1/H activation law in nanostructures with perpendicular magnetic anisotropy. *Phys. Rev. B*, 71:100402, 2005. (Cited on page 103.)

[139] J. F. Cuñado, A. Bollero, T. Pérez-Castañeda, P. Perna, F. Ajejas, J. Pedrosa, A. Gudín, A. Maldonado, M. A. Niño, R. Guerrero, D. Cabrera, F. J. Terán, R. Miranda, and J. Camarero. Emergence of the Stoner-Wohlfarth astroid in thin films at dynamic regime. *Sci. Rep.*, 7:13474, 2017. (Cited on pages 103 and 104.)

[140] D. Givord, P. Tenaud, T. Viadieu, and G. Hadjipanayis. Magnetic viscosity in different Nd-Fe-B magnets. *J. Appl. Phys.*, 61:3454, 1987. (Cited on page 102.)

[141] D. Givord, P. Tenaud, and T. Viadieu. Angular dependence of coercivity in sintered magnets. *J. Magn. Magn. Mater.*, 72:247, 1988. (Cited on page 102.)

[142] O. Fruchart, J.-P. Nozières, W. Wernsdorfer, D. Givord, F. Rousseaux, and D. Decanini. Enhanced coercivity in submicrometer-sized ultrathin epitaxial dots with in-plane magnetization. *Phys. Rev. Lett.*, 82:1305, 1999. (Cited on page 104.)

[143] J. Vogel, J. Moritz, and O. Fruchart. Nucleation of magnetisation reversal, from nanoparticles to bulk materials. *Comptes Rendus Physique*, 7:977, 2006. (Cited on page 104.)

Declaration

I herewith declare that I have produced this paper without the prohibited assistance of third parties and without making use of aids other than those specified; notions taken over directly or indirectly from other sources have been identified as such. This paper has not previously been presented in identical or similar form to any other German or foreign examination board.

The thesis was produced at the Laboratory for Spintronics and Devices Technology (SPINTEC) and Leibniz Institute for Solid State and Materials Research (IFW) as a co-tutelle thesis between the ComUE UGA and TU Dresden, under the scientific supervision of Olivier Fruchart and Bernd Büchner, and co-supervision of Romain Giraud.

Date, signature